THERMAL QCD SPECTRUM AND POTENTIAL: BOTTOMONIUM AT NON-ZERO TEMPERATURE

Prifysgol Abertawe
Swansea University

Thomas E. Spriggs

Submitted to Swansea University in partial fulfilment of the requirements for the Degree of

Doctor of Philosophy

2023

Abstract

The spectrum and potential of bottomonium mesons offer windows into strong force phenomenology. This thesis investigates these two constructs at non-zero temperature to explore thermal modifications of bound states. Lattice simulations are performed on two generations of the FASTSUM ensembles using a non-relativistic effective field theory of quantum chromodynamics, NRQCD. These ensembles contain 2+1 flavours of dynamical sea quarks at temperatures spanning the pseudocritical temperature. Maximum likelihood estimation is used to recover the spectrum of two representative bottomonium states, Υ and χ_{b1}, from which the ground state mass and width are determined at non-zero temperature. The central and spin-dependent potentials between the bottom quark and anti-quark are calculated using the approach from the HAL QCD collaboration. The standard implementation is used and then significant improvements are presented that provide a validation of the use of the non-relativistic Schrödinger equation at non-zero temperature.

Declaration

This work has not previously been accepted in substance for any degree and is not being concurrently submitted in candidature for any degree.

Signed: [redacted] (candidate)
Date: 05/12/2023

This thesis is the result of my own investigations, except where otherwise stated. Where correction services have been used, the extent and nature of the correction is clearly marked in a footnote(s). Other sources are acknowledged by footnotes giving explicit references. A bibliography is appended.

Signed: [redacted] (candidate)
Date: 05/12/2023

I hereby give consent for my thesis, if accepted, to be available for photocopying and for inter-library loan, and for the title and summary to be made available to outside organisations.

Signed: [redacted] (candidate)
Date: 05/12/2023

The University's ethical procedures have been followed and, where appropriate, that ethical approval has been granted.

Signed: [redacted] (candidate)
Date: 05/12/2023

Acknowledgements

I thank Prof. Chris Allton and Dr. Tim Burns for their invaluable supervision throughout this thesis, guiding me through more than just the physics. I would also like to thank: close collaborators Prof. Gert Aarts and Prof. Seyong Kim for their academic support as well as for providing me with ample long-haul flights; colleagues Prof. Sinéad Ryan and Prof. Mike Peardon at Trinity College Dublin for providing a stimulating yet enjoyable environment during my stay; Dr Rhian Melita Morris, Roz Toft, and Rosemary Granger for so much more than just administrative support; my former colleagues at Amplyfi for providing a great opportunity to learn and an abundance of coffee; and of course my family, the foundation from which I was able to build.

Author's Contributions

This thesis is based on published and unpublished work. Chapters 4 and 5 were presented in [1, 2] and [3] respectively, and parts of Chapter 6 were presented in [4] but developed further in this work.

The calculation of the correlators in Chapters 4 and 5, and the momentum space point-split correlators in Chapter 6 were performed by Prof. Seyong Kim using ensembles from the FASTSUM collaboration. The determination of the additive renormalisation of non-relativistic quantum chromodynamics in Chapter 4 was also the work of Prof. Seyong Kim.

All other analyses and interpretations in this thesis were performed by the author.

Dedication

To the village that raised this child.

Contents

List of Figures

List of Tables

Chapter 1

Introduction

The development of Quantum Chromodynamics (QCD) by Yang and Mills [5]; Gell-Mann [6]; Ne'eman [7]; Han and Nambu [8]; Drell, Levy, and Yan [9]; Gross and Wilczek [10]; Politzer [11]; and others was an outstanding achievement of the mid-to-late twentieth century. Interesting historical accounts are given by [12,13].

The details of QCD pertinent to this thesis are outlined in Chapter 2. They are presented in a way to motivate the need for a better understanding of the thermal modifications of the bottomonium system. The Lagrangian of QCD is stated alongside the definition and transformation properties of the constituent elements. An outline of the current understanding of the QCD phase diagram is given, with attention paid to the role played by chiral symmetry. The focus shifts then to colour confinement and hierarchical suppression: the systematic dissociation of different states at different temperatures that could be used to infer the conditions in the quark-gluon plasma. Quarkonia, mesons formed of a heavy quark and antiquark, are noted as excellent probes of this plasma and some important properties of bottomonium are elucidated.

The focus of Chapter 3 is lattice QCD, a non-perturbative framework for calculating hadronic observables in the strongly coupled regime of QCD. Monte Carlo integration and importance sampling are introduced as means to efficiently compute observables and the static quark potential is presented as a representative lattice observable. A prescription is given for altering the temperature of lattice simulations before an effective field theory known as non-relativistic quantum chromodynamics is outlined to make the calculations of heavy quarks more feasible.

The author's contributions begin in Chapter 4 with spectral reconstruction, the task of recovering meson spectra from Euclidean correlation functions measured on the lattice. The inherent difficulties are identified and an overview of the methods proposed for solving these is presented. Ansatze for spectral functions are developed along with their corresponding correlation functions. Maximum likelihood estimation is used to fit these ansatze to the lattice data and the ground state mass and width are extracted at various temperatures spanning the pseudocritical temperature. Careful checks are made to reduce, and extrapolate away, the systematic dependencies of these measurements.

Chapter 5 applies a method from the HAL QCD collaboration for calculating the interquark potential of bottomonium. The implementation follows the currently established approach and constitutes the first report of the bottomonium central potential at non-zero temperature using the HAL QCD method with NRQCD quarks. The lattice calculation of the point-split correlation function, the starting point of the HAL QCD method, is defined only along the axes of the lattice to reduce the computational costs of the calculation.

Finally, Chapter 6 builds upon Chapter 5 by examining each step of the HAL QCD method in further detail. This begins with an alternative calculation of the point-split correlation function that significantly reduces the computational costs; the calculation is then computed for all possible lattice sites. The specific forms of the finite difference derivatives are examined, lattice discretisation errors caused by a finite lattice spacing are quantified, and the importance of the quark mass input into the calculation is highlighted. After which, an alternative form of the HAL QCD method is developed with two improvements: firstly it allows the validity of the HAL QCD approach to be examined, pertinent for the extension of the method to non-zero temperature, and secondly it provides a self-consistent determination of the quark mass, which otherwise requires external input. In closing, the central and spin-dependent potentials are presented at a range of temperatures, with the former being fit to the Cornell potential and the low energy constants are presented as a function of temperature.

Chapter 2

QCD

2.1 QCD Lagrangian

The theory of QCD prescribes that colour, a novel fundamental charge at QCD's inception, is a degree of freedom of quarks and gluons. On top of this, quarks also carry degrees of freedom under the electromagnetic and weak nuclear forces. In combination, quarks and gluons form colour-neutral states, *hadrons*, comprised of two or three quarks: *mesons* and *baryons* respectively. Through e^+e^- collisions and pion decays it was found that there are three colours of quark [14], yet unlike these being three independent electromagnetism-like charges, they were intimately connected through gauge transformations, what we now know to be elements of $SU(3)$.

QCD is a Yang-Mills theory with an $SU(3)$ gauge group and six flavours of quark: up (u), down (d), strange (s), charm (c), bottom (b), and top (t) [15]. The QCD Lagrangian density is

$$\mathcal{L}_{QCD} = \bar{q}_f^j \left(i(\gamma^\mu \mathcal{D}_\mu)^{jk} - m_f \delta^{jk} \right) q_f^k - \frac{1}{4} G^a_{\mu\nu} G_a^{\mu\nu}, \tag{2.1}$$

for three colours $j, k = 1, 2, 3$; eight indices of Gell-Mann matrices $a = 1, 2, ...8$; Lorentz indices $\mu, \nu = 0, 1, 2, 3$; with flavour indexed f; and quark mass, m_f. Many of these indices will be dropped in subsequent formulae to simplify notation, we are also implicitly using the summation convention. γ_μ are the Dirac matrices that connect the spinor and vector representations of the Lorentz group. The quark (anti-quark) fields $q(x)$ ($\bar{q}(x)$), defined at point x in spacetime, transform under the fundamental representation of the gauge group, meaning

$$q(x) \to q'(x) = \Omega(x) q(x) \quad ; \quad \bar{q}(x) \to \bar{q}'(x) = \bar{q}(x) \Omega(x)^\dagger \tag{2.2}$$

where Ω is an element of $SU(3)$. The gauge fields, A^a_μ, transform under the adjoint representation of $SU(3)$ and appear in the Lagrangian through the covariant derivative,

$$\mathcal{D}_\mu = \partial_\mu - ig \frac{\lambda_a}{2} A^a_\mu. \tag{2.3}$$

The transformation properties of q_i and $\mathcal{D}_\mu q_i$ are the same by design. The coupling constant, g, is analogous with the electric charge in Quantum Electrodynamics (QED) and measures the strength of quark-gluon interactions. The matrices, λ_a, are the Gell-Mann matrices which are in turn the generators of the group $SU(3)$; their Lie algebra reads

$$[\lambda_a, \lambda_b] = 2if_{abc}\lambda_c. \tag{2.4}$$

f_{abc} is the real, totally antisymmetric structure constant. Finally, for the terms in the Lagrangian, the gluon field strength tensor is given by

$$G^a_{\mu\nu} = \partial_\mu A^a_\nu - \partial_\nu A^a_\mu + g f^{abc} A^b_\mu A^c_\nu. \tag{2.5}$$

Whilst this Lagrangian is reminiscent of QED, the non-Abelian nature of $SU(3)$ (compared to the Abelian group $U(1)$ for QED) adds significant complexity. The final term in equation (2.5), which is not present in QED, leads to interaction terms that are cubic or quartic in the gluon fields. These higher-order terms are self-interactions of the gauge fields and give rise to the confining nature of QCD [10, 14].

The coupling in QCD is not fixed and instead runs with energy scale as captured in the renormalisation group equations [10, 11]. The way the coupling (which we will rewrite as $\alpha_s = g^2/(4\pi)$ to make contact with α from QED) runs with energy scale, μ, is given by the β-function which reads

$$\mu^2 \frac{\partial \alpha_s}{\partial \mu^2} = \beta(\alpha_s) = -\frac{\beta_0}{2\pi}\alpha_s^2 + \mathcal{O}(\alpha_s^4), \tag{2.6}$$

with $\beta_0 = 11 - \frac{2}{3}N_f$, for N_f flavours of quark [16]. The key feature for non-Abelian gauge theories, notably for us QCD, is that the sign of the β-function is negative and thus the theory is asymptotically-free. This has interesting implications for the study of QCD as one can formally define two regimes: perturbative and non-perturbative. At low energies the coupling is large and any perturbative expansion breaks down, this prohibits the study of low-energy states, such as hadrons, with perturbative techniques. Chapter 3 introduces one method for probing the non-perturbative regime of QCD, lattice QCD.

2.2 Phase diagram of QCD

Having access to the Lagrangian of QCD is currently not enough to describe the whole landscape of the strong force and its interactions. It is interesting to study the dynamics of QCD with varying temperature, T, and (baryon) chemical potential, μ_B, for various reasons. One such reason is the expectation of a QCD

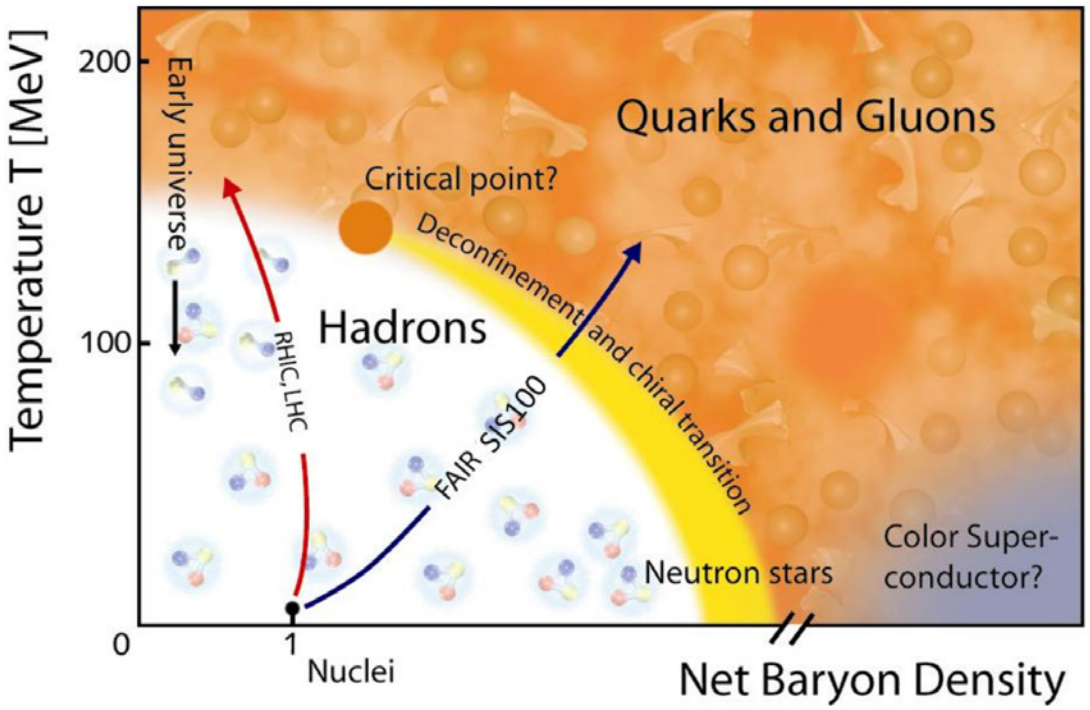

Figure 2.1: One proposal of the phase diagram of QCD from [24]. Net baryon density and baryon chemical potential are used interchangeably. Two existing collider experiments, the Relativistic Heavy Ion Collider (RHIC) at Brookhaven National Laboratory and the Large Hadron Collider (LHC) at CERN probe the region indicated by the red line. A new collider, Facility for Antiproton and Ion Research (FAIR), is planned to probe physics along the navy line.

phase transition playing a significant role in early Universe dynamics [17–20], for example, the nature of the QCD phase transition can affect the abundances of light elements. The dynamics of QCD are both explored using, and required to understand, heavy ion collisions at colliders like the Relativistic Heavy Ion Collider (RHIC) at Brookhaven National Laboratory and the Large Hadron Collider (LHC) at CERN [21,22]. This offers insight into the axis of increased temperature and nominal μ_B.

The mapping out of the various regions of the phase diagram is an active area of research. The currently supported features are: an area of colour confinement at small T and μ_B, quark-gluon plasma (QGP) formation at large T and moderate μ_B where colour confinement no longer occurs, and a possible lens into neutron star phenomenology at large μ_B [23]. These are summarised in Figure 2.1.

Although Figure 2.1 is only a representative figure, and there is much debate about the details, a feature that is common to many depictions of the phase dia-

gram is the chiral transition. It is also significant that chiral symmetry restoration is expected to occur in the neighbourhood of the deconfining transition. For this reason, we will explore some of the details of chiral symmetry here.

The Lagrangian introduced in Section 2.1 couples left and right handed fermions only through the mass term [25]; the left (right) handed fields are defined as $q^{L,R} = \frac{1\mp\gamma_5}{2}q$, where $\gamma_5 = i\gamma_0\gamma_1\gamma_2\gamma_3$[1]. Therefore, for the case of massless light quarks (u, d, s) there exists a chiral symmetry such that the Lagrangian is invariant under the individual (or combined) applications of

$$\begin{pmatrix} u^L \\ d^L \\ s^L \end{pmatrix} \rightarrow U_L \begin{pmatrix} u^L \\ d^L \\ s^L \end{pmatrix} \quad ; \quad \begin{pmatrix} u^R \\ d^R \\ s^R \end{pmatrix} \rightarrow U_R \begin{pmatrix} u^R \\ d^R \\ s^R \end{pmatrix}. \tag{2.7}$$

$U_{L,R} \in SU(3)_{L,R}$ (*i.e.* an element of $SU(3)$ that only acts on the left (right) handed quarks) and thus the chiral symmetry group is $SU(3)_L \times SU(3)_R$. The QCD vacuum is not invariant under these chiral transformations, even for massless quarks: the interactions between quarks and gluons give the quarks an effective mass which breaks chiral symmetry. Therefore, this symmetry is spontaneously broken. Quarks in Nature are not massless, and so the symmetry is explicitly broken, too. Nevertheless, at high enough energies we can consider chiral symmetry breaking as a perturbation of the true Lagrangian for the light quarks. However, the effect is too large for heavy quarks (c, b, t) for this to be a valid perturbation theory [26]. This is why the effective number of flavours in the chiral group is 3, rather than 6.

Despite the explicit breaking of this symmetry, the order parameter, the chiral condensate, can still be used as a remnant order parameter to define a pseudo-critical temperature of the spontaneous symmetry breaking for lattice QCD simulations [27]. This is how $T_{\rm pc}$ is established in the lattice configurations presented in Section 3.6. The chiral condensate is defined as

$$\langle \bar{q}q \rangle = \frac{T}{V}\frac{\partial \ln Z}{\partial m_q}, \tag{2.8}$$

and the accompanying chiral susceptibility is

$$\chi_{\bar{q}q} = \frac{T}{V}\frac{\partial^2 \ln Z}{\partial m_q^2}. \tag{2.9}$$

T denotes the temperature, V the spatial volume, m_q the quark mass, and Z the partition function.

For the remainder of this work, we will consider $\mu_B = 0$ and explore the dependence on temperature.

[1] By convention the Dirac indices will run from $0-3$ in Minkowski spacetime but they will change to $1-4$ for the Euclidean spacetime of the lattice.

2.3 Quarkonium

Quarkonia are mesons comprised of a heavy quark and anti-quark of the same flavour, pertinent for our discussions are charmonia and bottomonia, $c\bar{c}$ and $b\bar{b}$ respectively. They have several interesting properties, notably their large binding energies and small radii: the lightest vector meson in charmonium (bottomonium) is the J/ψ (Υ) with a binding energy of 0.6 GeV (1.1 GeV) and a radius of 0.5fm (0.3fm) [28].

Eichten *et al.* accurately predicted the charmonium spectrum by considering a simple non-relativistic interaction between quarks underpinned by a phenomenologically inspired potential, the Cornell potential [29–31]. This potential interpolates between a repulsive, Coulomb-like, core and a linearly rising, confining, large distance form, given by

$$V_{\text{Cornell}}(r;T) = -\frac{\alpha(T)}{r} + \sigma(T)r + C. \tag{2.10}$$

The parameters α and σ are the coupling and string tension respectively (for convention I will often report $\sqrt{\sigma}$ rather than σ and refer to both as the string tension). $\sqrt{\sigma}$ was found to be 0.445 GeV in [28].

In Chapter 3 I will introduce non-relativistic QCD (NRQCD), a non-relativistic effective field theory to reduce the computational demands of simulating QCD on the lattice. Then, in Chapters 5 and 6, I will first assume, and then test, the picture that quark dynamics can be modelled using a Schrödinger equation with a single potential. Both of these simplifications gain support from the accuracy with which Eichten *et al.* were able to predict charmonium masses using a non-relativistic potential model. I will study bottomonium throughout this thesis, and as the mass scales in bottomonium are larger than charmonium, these simplifications are even more justified.

In their seminal paper, Matsui and Satz offer up the suppression of J/ψ production in nuclear collisions as an "unambiguous signature of quark-gluon plasma formation" [32]. They show how colour screening would prevent the binding of $c\bar{c}$ states as the screening radius becomes shorter than the radius of the bound state. Colour screening is analogous to Debye screening in QED whereby the polarisible medium screens the effect of electrical charge and thus reduces the impact of long-range effects. In QED one replaces the Coulomb potential with a screened form that reads

$$V_{\text{QED}}(r) = \frac{e^2}{r} \to \frac{e^2}{r}\exp(-r/r_D), \tag{2.11}$$

which has only minor modification when the distance, r, is smaller than the Debye radius, r_D, but shows significant dampening of the potential at scales larger than

r_D. In QCD we expect a similar effect, screening of the colour charges and a reduction in the impact of long-range physics. Resultantly, for $r \gg r_D$, quarks in a meson can no longer impact each other and thus a bound state, which is dependent on their interaction, will become unbound or "melt".

A further complexity that opens a window into the QGP is that the minimum Debye radius that allows a bound state to exist is dependent on the temperature through the running coupling of QCD, $\alpha_{\text{eff}}(T)$ [32]. Because different quarkonium states vary in size, colour screening can cause the suppression of different states at distinct temperatures, known as *hierarchical suppression*. Therefore, analysis of charmonium, and bottomonium by extension, would offer a thermometer of sorts. This thesis can be seen as work towards calibrating this thermometer: in Chapter 4 through direct spectral analysis then in Chapters 5 and 6 through thermal modifications to the interquark potential, through which spectra can be recovered.

Chapter 3

Lattice QCD

To understand the hierarchical suppression of quarkonium states we must probe the non-perturbative regime of QCD. At these energy scales, as the name suggests, perturbative methods fail due to the size of the coupling, so the powerful toolkit developed for solving interactions of QED is of limited use. Instead, we use lattice QCD: the only known first-principles method for calculating the non-perturbative physics of QCD.

Lattice QCD is an application of the wider approach of lattice field theory to QCD. Lattice field theories are formulated in a discrete space-time governed by an Euclidean signature. The discretised space-time locations are separated by a lattice spacing, a, which explicitly introduces an ultraviolet (UV) regulator in the form of a momentum cut-off at order $1/a$. The finiteness of the lattice offers regularisation of the infrared (IR) physics and in combination with the UV regulator these lead to a rigorously defined field theory. For much of this chapter I will be following the notation of [16], a resource the reader is pointed to for further details.

I will now introduce only a small selection of the necessary elements of lattice QCD, focusing on those most pertinent to our goal of exploring quarkonium spectra at non-zero temperature: calibrating the thermometer by which we measure the QGP. I will start with the fundamentals of taking a measurement using Monte Carlo methods. Then I will introduce the formalism required to understand the equations of lattice QCD, paired with an example of a specific lattice measurement, the static quark potential. This is followed by a prescription of simulating QCD at non-zero temperature and then present an effective field theory that reduces the computational demands of simulations by narrowing the range of energy scales considered. The chapter concludes with a report of the lattice set-up used for these works aimed at the technical reader.

3.1 Monte Carlo methods

To measure the expectation value of an observable, O, one must evaluate the path integral over all possible configurations of the quark and gluon fields,

$$\langle O \rangle = \frac{1}{Z} \int D[q, \bar{q}, A] e^{-iS_{QCD}[q,\bar{q},A]} O[q, \bar{q}, A]. \tag{3.1}$$

The quark and anti-quark fields are again denoted by q and $\bar{q}$ respectively, the gluon fields are given by A, the measure of integration by $D[q, \bar{q}, A]$, and the partition function, Z, which plays the same role as it does in statistical mechanics. The partition function is the normalisation given by

$$Z = \int D[q, \bar{q}, A] e^{-iS_{QCD}[q,\bar{q},A]}, \tag{3.2}$$

from which one can determine thermodynamic quantities.

When it comes to numerically solving the discretised version of equations (3.1) and (3.2) for QCD one encounters a problem. The integrals quickly grow to an intractable number of dimensions as the size of the lattice increases, as well as when the complexity of the theory increases. We turn, therefore, to methods of approximating equation (3.1), namely Monte Carlo methods of integration.

Consider, for a moment, a pure gauge theory. I will denote the representation of gauge fields on the lattice $U_\mu(n)$, which is related to the continuum gauge fields, $A_\mu(n)$, through

$$U_\mu(n) = e^{iaA_\mu(n)}, \tag{3.3}$$

for finite lattice spacing a, Lorentz index, μ, and lattice site, n. More details of the QCD formalism will be given in Section 3.2. To approximate a measurement using a Monte Carlo sum one calculates

$$\langle O \rangle \approx \frac{1}{N} \sum_{U_\mathcal{N} \in\, p(U_\mathcal{N})} O[U_\mathcal{N}]. \tag{3.4}$$

That is to say one can take the average of N values of the observable, each evaluated on a particular configuration of a gauge field, $U_\mathcal{N}$, provided that a specific distribution of configurations is sampled from, $p(U_\mathcal{N})$. The probability distribution is known but collating an ensemble of fields that are truly a representation of this distribution is challenging, yet mandatory. I will postpone the discussion of measuring an observable on a single field configuration until Section 3.3, I will, however, now briefly explore the way in which we arrive at a representative ensemble of configurations upon which we take each measurement.

The probability distribution over field configurations, $p(U_\mathcal{N})$, is proportional to the Boltzmann weight, $\exp(-S[U_\mathcal{N}])$, for a given action $S[U_\mathcal{N}]$ (the specific

form of the action is the topic of Section 3.2 and not required here). This probability distribution is highly skewed with most configurations contributing little weight and relatively few configurations making up most of the total weight. This means that randomly sampling fields and weighing their contribution with $\exp(-S[U_{\mathcal{N}}])$ would be incredibly inefficient. Instead, we opt for *importance sampling*. To perform importance sampling we adjust field values and use the Metropolis-Hastings algorithm as an accept/reject step to build a *Markov chain* of configurations. This allows us to correctly sample fields with probability $p(U_{\mathcal{N}}) = \exp(-S[U_{\mathcal{N}}])$. Readers wanting a broader review of update algorithms are pointed towards [16, 33]. The notion that we will take forward is the idea that to perform numerical simulations of lattice QCD one computes an ensemble of representative gauge fields and only afterwards uses these for taking measurements.

The addition of fermions into the theory is non-trivial but does not change the picture elucidated above: an ensemble of gauge fields is generated first, upon which a measurement is made afterwards.

The difficulties with fermions are that they obey Fermi statistics and are thus difficult to represent computationally. Grassman numbers are anti-commuting numbers that encode Fermi statistics but their algebra must be handled analytically. We draw a distinction between *sea* and *valence* quarks: defined through the picture of a background of pair-creating and annihilating sea quarks in which the valence quarks propagate, with the valence quarks being those of relevance to hadronic measurements. The distinction is drawn purely for technical reasons and the handling of each is vastly different. The inclusion of valence quarks will be discussed in Section 4.1 when we consider meson correlators. Sea quarks, however, are incorporated during the generation of the gauge fields, the algorithms through which they are included lie outside the scope of this work (see [16, 33]). The takeaway is this: the gauge fields generated are those that are 'aware' of the influence of the sea quarks, and measurements of valence quark behaviour are made upon these gauge fields. Therefore, equation (3.4) is still valid for a theory with fermions.

The gauge fields used throughout this thesis were generated by the FASTSUM collaboration and more details will be provided in Section 3.6.

3.2 Lattice QCD formalism

To arrive at the lattice version of the QCD action we must first introduce the building blocks of the theory: the lattice itself and the matter and gauge fields as well as their transformation properties. We define a lattice, Λ, to be a four-dimensional hypercube with three dimensions of space and one of time governed

by an Euclidean space-time metric,

$$\Lambda = \{n = (n_1, n_2, n_3, n_4) | n_1, n_2, n_3 = 0, 1, ..., N_s - 1; n_4 = 0, 1, ..., N_\tau - 1\}. \quad (3.5)$$

The vectors, n, label space-time locations on the lattice which are each separated by the lattice spacing, a, and therefore any physical distance would be $x = an$.

The fermions in our theory live on lattice sites labelled by n, so the quark and anti-quark fields are defined at

$$q(n), \bar{q}(n). \quad (3.6)$$

These fields carry the same degrees of freedom as the continuum representation of fermions: colour, spinor, and flavour indices. They also transform in the same way as their continuum counterpart; for an element, $\Omega(n)$, of $SU(3)$, they transform as

$$q(n) \to q'(n) = \Omega(n)q(n) \ ; \ \bar{q}(n) \to \bar{q}'(n) = \bar{q}(n)\Omega(n)^\dagger. \quad (3.7)$$

The introduction of the gauge fields confronts one of the fundamental differences between the lattice and continuum: the nature of derivatives. On the lattice, one must take a discretised derivative whereby the value of the field at two different lattice sites is considered. If we observe the transformation property of, for example, a combination of fields separated by the unit distance along the μ axis, namely

$$\bar{q}(n)q(n + \hat{\mu}) \to \bar{q}'(n)q'(n + \hat{\mu}) = \bar{q}(n)\Omega(n)^\dagger\Omega(n + \hat{\mu})q(n + \hat{\mu}), \quad (3.8)$$

then we can see that this term is not gauge invariant. We introduce our gauge fields (also known as *link variables*), $U_\mu(n)$, an oriented element of $SU(3)$ that lives on the links between lattice sites to enforce gauge invariance. These are exactly as defined in equation (3.3). If we insert a link variable into the bilinear

$$\bar{q}(n)U_\mu(n)q(n + \hat{\mu}) \to \bar{q}'(n)U'_\mu(n)q'(n + \hat{\mu}) = \bar{q}(n)\Omega(n)^\dagger U'_\mu(n)\Omega(n + \hat{\mu})q(n + \hat{\mu}), \quad (3.9)$$

then we can make the whole object gauge invariant by proposing that the gauge fields transform as

$$U_\mu(n) \to U'_\mu(n) = \Omega(n)U_\mu(n)\Omega(n + \hat{\mu})^\dagger. \quad (3.10)$$

Notationally, the link variable $U_\mu(n)$ joins the sites n and $n + \hat{\mu}$ oriented from the former to the latter. The hermitian conjugate is defined as

$$U_{-\mu}(n) \equiv U_\mu(n - \hat{\mu})^\dagger. \quad (3.11)$$

We now have enough gauge invariant objects to define the so-called *naive fermion action*,

$$S_F[q,\bar{q},U] = a^4 \sum_{n\in\Lambda} \bar{q}(n) \left(\sum_{\mu=1}^{4} \gamma_\mu \frac{U_\mu(n)q(n+\hat{\mu}) - U_{-\mu}(n)q(n-\hat{\mu})}{2a} + mq(n) \right). \tag{3.12}$$

This form of the fermion action actually gives rise to many more fermions than were originally intended. To highlight this I will define the responsible term from the action, namely the Dirac operator given by

$$D(n|m)_{\alpha\beta;ab} = \sum_{\mu=1}^{4} (\gamma_\mu)_{\alpha\beta} \frac{U_\mu(n)_{ab}\ \delta_{n+\hat{\mu},m} - U_{-\mu}(n)_{ab}\ \delta_{n-\hat{\mu},m}}{2a} + m\delta_{\alpha\beta}\ \delta_{ab}\ \delta_{n,m}, \tag{3.13}$$

where I have included the colour (a,b) and Dirac (α,β) indices for completeness here, yet they will again be dropped for notational clarity going forward. I will also consider the trivial gauge, meaning $U_\mu(n) = \mathbb{I}$. The Fourier transform of the Dirac operator, for a lattice of volume $|\Lambda|$, defined through

$$\tilde{D}(P|Q) = \frac{1}{|\Lambda|} \sum_{n,m\in\Lambda} e^{-iP\cdot na} D(n|m) e^{iQ\cdot ma}, \tag{3.14}$$

for momenta P and Q, reads

$$\tilde{D}(P|Q) = \frac{1}{|\Lambda|} \sum_{n\in\Lambda} e^{-i(Q-P)\cdot na} \left(\sum_{\mu=1}^{4} \gamma_\mu \frac{e^{iQ_\mu a} - e^{-iQ_\mu a}}{2a} + m\mathbb{I} \right). \tag{3.15}$$

Taking the massless case gives

$$\tilde{D}(P|Q) = \delta(P-Q) \frac{i}{a} \sum_{\mu=1}^{4} \gamma_\mu \sin(P_\mu a). \tag{3.16}$$

A single fermion corresponds to a pole in the propagator, which is the inverse of this Dirac operator, D^{-1}, such a pole is caused when equation (3.16) is zero. The pole at $P = (0,0,0,0)$ corresponds to the fermion that we intended to introduce, however, the lattice momenta are defined to lie in the range $P_\mu \in (-\pi/a, \pi/a]$ and thus we get spurious fermions at 15 different momenta ($P = (\pi/a,0,0,0), (0,\pi/a,0,0)$ *etc.*). These unphysical fermions are called *fermion doublers* and cannot be excluded without using an alternative form of the fermion action.

To counter these unphysical fermion doublers, Wilson proposed an additional term to the Dirac operator that distinguishes the physical fermion from its doublers. The so-called Wilson term is added to give

$$\tilde{D}(P) = \frac{i}{a}\sum_{\mu=1}^{4}\gamma_\mu \sin(P_\mu a) + \mathbb{I}\frac{1}{a}\sum_{\mu=1}^{4}(1-\cos(P_\mu a)). \tag{3.17}$$

This has the effect of attributing a mass proportional to $2/a$ to all of the fermion doublers without changing the physical fermion. In the continuum, these doublers become far heavier than the physical state and thus they decouple from the theory. Using this altered form of the Dirac operator in the fermion action alleviates the problem of fermion doublers.

Despite this alleviation of the fermion doublers, and as was alluded to in Section 3.1, the handling of fermions on the lattice is highly non-trivial. The naive action is seldom used in precision QCD calculations. The high-level details of the action used by the FASTSUM collaboration is mentioned in Section 3.6 however this is aimed at the technical reader and is not a first-principles introduction of the fermion action. We will not provide further details regarding the fermion action in this work.

For the gauge action, we can create the simplest gauge invariant object comprised purely of gauge fields, the trace of the *plaquette*. The plaquette, $U_{\mu\nu}(n)$, defined as

$$\begin{aligned} U_{\mu\nu}(n) &= U_\mu(n)U_\nu(n+\hat{\mu})U_{-\mu}(n+\hat{\mu}+\hat{\nu})U_{-\nu}(n+\hat{\nu}) \\ &= U_\mu(n)U_\nu(n+\hat{\mu})U_\mu(n+\hat{\nu})^\dagger U_\nu(n)^\dagger. \end{aligned} \tag{3.18}$$

The first line depicts how this is a closed 1×1 loop of links yet the second line is used for notational convenience. To make explicit the gauge transformation of this object, consider the transformation property given by equation (3.10): a product of links where each link is connected to the former would transform as a string of these expressions. Importantly, there would be a mass cancellation of $\Omega(m)^\dagger$ and $\Omega(m)$ pairs because the links are connected, all that would remain is an $\Omega(n)$ at the start of the loop and an $\Omega(n')^\dagger$ at the end. This is to say that if even the start and end points are connected, *i.e.* in a closed loop, and we take the trace of this plaquette, then all of the transformation matrices cancel and the object is gauge invariant. A gauge action can be formed by the sum over traced plaquettes counted only along one orientation. The simplest implementation of this sum is

$$S_G[U] = \frac{2}{g^2}\sum_{n\in\Lambda}\sum_{\mu<\nu}\text{Re tr}[\mathbb{I}-U_{\mu\nu}(n)]. \tag{3.19}$$

Therefore, formally, the lattice QCD action is simply

$$S[q,\bar{q},U] = S_F[q,\bar{q},U] + S_G[U]. \tag{3.20}$$

As I hope the wording has been suggesting, these are not unique definitions of the fermion or gauge actions. Each definition used should reproduce the continuum expression when one takes the continuum limit (defined as $a \to 0$), but the size of the discretisation errors present before this limit can vary with specific forms of the action. The exact action used for the FASTSUM configurations is addressed in Section 3.6.

3.3 Static quark potential

Equipped with the formulation of lattice QCD, one measurement that can be made upon these lattice configurations is that of the Wilson loop from which we can extract the potential between two infinitely heavy quarks. We call this potential the *static quark potential* as the infinitely heavy quarks cannot propagate in space and are thus static. We will review the results extracted from the static quark potential in Chapters 5 and 6 where we will also report research into the potential of heavy (but finite mass) quarks.

The Wilson loop is a gauge-invariant trace over a particular closed loop of link variables given by

$$L[U] = \mathrm{Tr}\left[\prod_{n,\mu\in\mathcal{L}} U_\mu(n)\right]. \tag{3.21}$$

The closed loop, $\mathcal{L}$, is constructed of four parts: two so-called *Wilson lines* connecting two spatial points, $\mathbf{m}$ and $\mathbf{n}$, at different points in Euclidean time, 0 and n_τ, given by $S(\mathbf{m},\mathbf{n},0)$ and $S(\mathbf{m},\mathbf{n},n_\tau)$, respectively; and two *temporal transporters* that connect the edges of each Wilson line at the same points in space, given by

$$T(\mathbf{n},n_\tau) = \prod_{j=0}^{n_\tau-1} U_4(\mathbf{n},j) \quad ; \quad T(\mathbf{m},n_\tau) = \prod_{j=0}^{n_\tau-1} U_4(\mathbf{m},j). \tag{3.22}$$

An example of a Wilson loop is shown in Figure 3.1.

As previously mentioned, this is a gauge-invariant quantity. However, choosing a particular gauge makes the following physical interpretations of the Wilson loop easier. A similar, albeit more detailed, heuristic argument can be found in [16] and much more detail is provided in [34]. The chosen gauge is the temporal gauge with the only pertinent detail being that $A_4(n) = 0$. Consequently, the temporal transporters reduce to simply

$$T(\mathbf{n},n_\tau) = T(\mathbf{m},n_\tau) = \mathbb{I}. \tag{3.23}$$

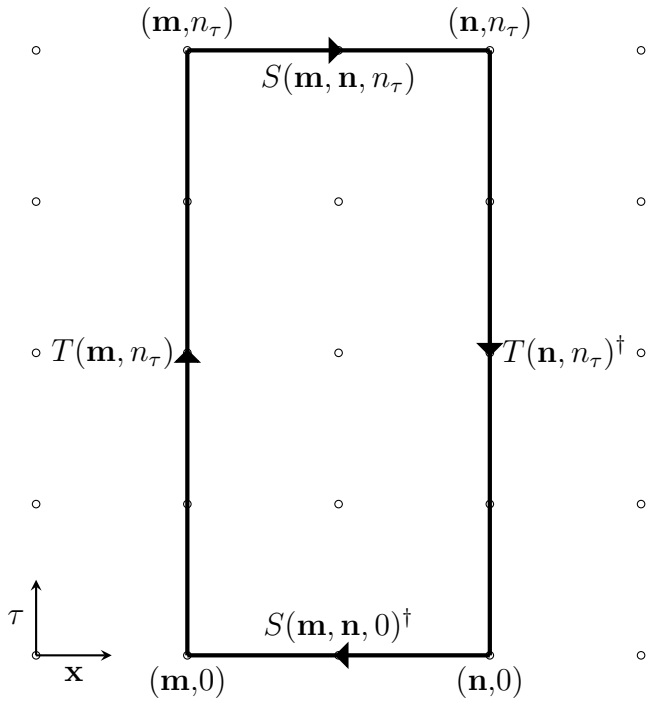

Figure 3.1: An example of a Wilson loop. The arrows depict the directed path, $\mathcal{L}$, that is defined in equation (3.21).

With the temporal transporters trivialised, the Wilson loop is reduced to the two-point correlator of the Wilson lines

$$L[U] = \mathrm{Tr}\left[S(\mathbf{m}, \mathbf{n}, n_\tau)S(\mathbf{m}, \mathbf{n}, 0)^\dagger\right]. \tag{3.24}$$

The Hermitian conjugate of the second Wilson line is a result of orientation around the loop. I will postpone the details of large time limits of the expectation value of two point correlators until Section 4.3.1 but simply state here that, at late times, the expectation value of the Wilson loop behaves as

$$\langle L\rangle = \sum_k \langle 0|\widehat{S}(\mathbf{m}, \mathbf{n})|k\rangle\langle k|\widehat{S}(\mathbf{m}, \mathbf{n})^\dagger|0\rangle e^{-ian_\tau E_k}. \tag{3.25}$$

$\widehat{S}$ is the operator form of the functional S, a is the lattice spacing, and k indexes the ground and excited states, each with energy E_k. All that remains is to make contact with which system these energy levels refer to.

The hopping expansion is a series expansion of the quark propagator in terms of the quark mass, valid in the limit of heavy quark mass. Whilst the details are not covered here (the interested reader can consult [16, 34]) we will take the

result that, in the limit of infinite quark mass, the quark propagator can be approximated by the shortest path of link variables connecting two points: this is exactly the Wilson line. Therefore, the physical system whose states are labelled k in equation (3.25) is that of two infinitely heavy quarks. This means that the energy of this ground state, E_1, is the free energy between two bound quarks of infinite mass: the static quark potential, V.

Calculating the expectation value in equation (3.25) at various quark separations ($r = |\mathbf{m} - \mathbf{n}|$) gives

$$\langle L(r) \rangle = e^{-n_t a V(r)} \left(1 + \mathcal{O}(e^{-n_t a \Delta E})\right), \tag{3.26}$$

where ΔE is the difference between the ground and the first excited state of the quark-antiquark pair. This means that in the large-n_t limit, one can extract the static quark potential with only a minor correction due to excited states.

We will return to the static quark potential in Chapters 5 and 6 when we introduce the HAL QCD method for calculating the potential between two heavy quarks.

3.4 Non-zero temperature

For a computation of an observable over the entire lattice, the lattice must be finite. The finite spatial extent dictates the resolution of momenta available on the lattice and the temporal extent dictates the temperature. The result evincing the latter statement will just be stated here, but the interested reader is pointed to [16, 33, 35] for more details. By considering a particular form of the partition function on the lattice in terms of the Hamiltonian operator, $\widehat{H}$, and the number of lattice sites in the time dimension, N_τ, as

$$Z = \mathrm{Tr}\left[e^{-aN_\tau \widehat{H}}\right], \tag{3.27}$$

we can draw a parallel with statistical mechanics where the partition function reads

$$Z = \mathrm{Tr}\left[e^{-\beta \widehat{H}}\right]. \tag{3.28}$$

We identify β, equal to $1/(k_B T)$ in that domain (with k_B being the Boltzmann constant), as aN_τ in lattice field theory. Thus, we have the relation

$$aN_\tau = \beta = \frac{1}{k_B T}, \tag{3.29}$$

giving two ways to change the temperature in a lattice simulation: changing the lattice spacing or changing the number of points in the time dimension. The

lattice spacing is intimately related to the running of the gauge coupling and quark mass through the renormalisation group equations, and therefore altering a along a line of constant physics is highly non-trivial. It is for this reason that the approach taken by the FASTSUM collaboration, and thus this work, is to change temperature with a fixed a but varying N_τ, the so-called *fixed scale* approach. This is beneficial as once a single temperature has been tuned to give the desired physical setting, simulating other temperatures just requires changing N_τ. However, the obvious drawback of this is that a naive comparison between different temperatures is between different sized data and thus we must take care to control the data in a way that minimises this systematic difference.

Given equation (3.29) it is clear that any notion of zero temperature in a finite lattice simulation is not strictly accurate, instead one uses zero temperature when referring to a temperature far below the region of any phase transitions. The range of temperatures used for these works are shown in Tables 3.1 and 3.2; two generations of configurations were used, generation-2L (for Chapter 4) and generation-2 (for Chapters 5 and 6). Chronologically, generation-2 preceded generation-2L.

Lattice studies at non-zero temperature can certainly be done on isotropic lattices: where the lattice spacing in the time and space dimensions are equal, $a_s = a_\tau = a$. See, as examples, [36–41]. However, there are benefits to studying anisotropic lattices, where $a_s = \xi a_\tau$ with $\xi \neq 1$. Firstly, and most importantly for these works, it increases the resolution in the time dimension as there are ξ times more data available for analysis without having to change the spatial volume. Secondly, a smaller a_τ reduces the discretisation errors in the quark evolution equation that will be introduced in Section 3.5. The exact value of the anisotropy, ξ, changes between generations-2 and -2L of the FASTSUM configurations (see Tables 3.1 and 3.2) but is approximately 3.5 for both.

3.5 Non-relativistic QCD

Following the argument of Thacker and Lepage [42], we consider the relevant energy scales for bottomonium: the bottom quark mass, m_b, its 3-momentum, $m_b v$, and its kinetic energy, $m_b v^2$. If we take the case where v is small (measured in units of the speed of light), then these scales are greatly separated: one needs a lattice that is large relative to $1/(m_b v^2)$ but a lattice spacing that is small relative to $1/m_b$ to control finite volume and lattice spacing effects respectively. For the bottomonium vector meson Υ, $v \sim 0.1c$ and thus we are certainly in the regime where both scales are hard to achieve simultaneously.

Non-relativistic quantum chromodynamics (NRQCD) is an effective field theory (EFT) that explicitly removes the energy scale of m_q by integrating it out

of the theory. By this, it is meant that we introduce an energy cut-off, Ξ, along with new local interactions into our theory to account for any relativistic physics that occurs at scales beyond our cut-off. It would be our intention to write out the resulting theory to all relevant orders in $1/\Xi$ and observe the effect of sending the cut-off to infinity. However, as stated by Thacker and Lepage, if one requires accuracy of order $(p/\Xi)^n$ then one need only include $\mathcal{O}(1/\Xi^n)$ interactions. Therefore, if we set $\Xi \sim m_q$ (and subsequently $(p/\Xi)^n \sim v^n$) then we can rephrase the new local interactions as a Taylor expansion in the heavy quark velocity of the Lagrangian and any terms that are not accounted for are swept away as corrections at a certain order in the Taylor series. One should note that this series converges quickly for bottomonium with $v \sim 0.1c$.

One further convenience of the theory is introduced by means of a Foldy-Wouthuysen-Tani transformation [43] which decouples the quark and antiquark fields. The immediate effect of this is that the particle and antiparticle number of each field is conserved separately and thus there is no annihilation to gluons or pair production. The former only offers a small contribution to the total decay rate and the latter occurs at energy scales around that of our cut-off; both effects can be reintroduced either as a new Fermi interaction term or as a perturbation to the existing theory [42]. I will return to the other benefit of this decoupling momentarily.

The fermionic part of the NRQCD Lagrangian expansion to $\mathcal{O}(v^4)$ in terms the decoupled quark and anti-quark fields, q and $\bar{q}$ respectively, is given by

$$\begin{aligned}
\mathcal{L} = {} & q^\dagger \left(D_\tau - \frac{\mathbf{D}^2}{2m_b} \right) q + \bar{q}^\dagger \left(D_\tau + \frac{\mathbf{D}^2}{2m_b} \right) \bar{q} \\
& - c_1 \frac{1}{8m_q^3} \left[q^\dagger (\mathbf{D}^2)^2 q - \bar{q}^\dagger (\mathbf{D}^2)^2 \bar{q} \right] \\
& + c_2 \frac{ig}{8m_q^2} \left[q^\dagger (\mathbf{D}\cdot\mathbf{E} - \mathbf{E}\cdot\mathbf{D}) q + \bar{q}^\dagger (\mathbf{D}\cdot\mathbf{E} - \mathbf{E}\cdot\mathbf{D}) \bar{q} \right] \\
& - c_3 \frac{g}{8m_q^2} \left[q^\dagger \boldsymbol{\sigma}\cdot(\mathbf{D}\times\mathbf{E} - \mathbf{E}\times\mathbf{D}) q + \bar{q}^\dagger \boldsymbol{\sigma}\cdot(\mathbf{D}\times\mathbf{E} - \mathbf{E}\times\mathbf{D}) \bar{q} \right] \\
& - c_4 \frac{g}{2m_q} \left[q^\dagger \boldsymbol{\sigma}\cdot\mathbf{B} q - \bar{q}^\dagger \boldsymbol{\sigma}\cdot\mathbf{B} \bar{q} \right] .
\end{aligned} \tag{3.30}$$

The first line contains the zeroth order term and the next-to-leading-order contributions on the following lines [44]. The covariant derivative is $D_\mu = \{\mathbf{D}, D_\tau\}$ in continuum NRQCD, but when discretised for the lattice it becomes the central

derivative, Δ_μ, built from forward and backwards finite differences

$$\begin{aligned}\Delta_\mu^{(+)}q(n) &= U_{n,\mu}q(n+\hat{\mu}) - q(n)\\ \Delta_\mu^{(-)}q(n) &= q(n) - U^\dagger_{n-\hat{\mu},\mu}q(n-\hat{\mu})\\ \Delta_\mu q(n) &= \frac{1}{2}\left(\Delta_\mu^{(+)}q(n) + \Delta_\mu^{(-)}q(n)\right).\end{aligned} \tag{3.31}$$

$\mathbf{E}$ and $\mathbf{B}$ are the chromoelectric and chromomagnetic fields respectively and $\boldsymbol{\sigma}$ are the Pauli matrices. The unknown constants c_i, m_q, and g capture the relativistic physics that was integrated out by the cut-off. Each c_i can be computed using perturbation theory if the quark mass is heavy enough: one can compare computations of amplitudes using QCD and NRQCD and adjust the coupling constants until the two agree. At tree-level in perturbation theory $c_i = 1$. Such constants can also be numerically tuned to data (from relativistic QCD simulations) should the perturbative treatment fail.

Another key result is that the decoupling of quark and antiquark fields leads to a significantly simpler propagation of quarks. The propagation is solved as an initial-value problem, given by

$$G(\mathbf{x},\tau+a_\tau) = \left(1-\frac{a_\tau H_0|_{\tau+a_\tau}}{2k}\right)^k U_4^\dagger(\mathbf{x},\tau)\left(1-\frac{a_\tau H_0|_\tau}{2k}\right)^k (1-a_\tau\delta H)G(\mathbf{x},\tau). \tag{3.32}$$

The Lepage parameter, k, is introduced to add stability to the propagation of quarks with high momentum, often $k=1$ is sufficient but we will come back to this in Section 6.1.2 when we consider a case where it must be increased. The initial condition is $G(\mathbf{x},0) = S(\mathbf{x})$, where $S(\mathbf{x})$ is a particular choice of source, this will be explored more in Section 4.2.1. This expression contains the contribution from the leading order kinetic operator,

$$H_0 = -\frac{\Delta^2}{2m_b} \tag{3.33}$$

where $\Delta^{2n} = \sum_{i=1}^3 (\Delta_i^{(+)}\Delta_i^{(-)})^n$, as well as radiative corrections introduced through

$$\begin{aligned}\delta H = &-\frac{(\Delta^2)^2}{8m_b^3} + \frac{ig_0}{8m_q^2}(\boldsymbol{\Delta}^\pm\cdot\mathbf{E} - \mathbf{E}\cdot\boldsymbol{\Delta}^\pm)\\ &-\frac{g_0}{8m_b^2}\boldsymbol{\sigma}\cdot(\boldsymbol{\Delta}^\pm\times\mathbf{E} - \mathbf{E}\times\boldsymbol{\Delta}^\pm) - \frac{g_0}{2m_b}\boldsymbol{\sigma}\cdot\mathbf{B}\\ &+\frac{a_s^2\Delta^4}{24m_b} - \frac{a_\tau(\Delta^2)^2}{16m_b^2}.\end{aligned} \tag{3.34}$$

The final correction of which we will mention is *tadpole improvement* whereby we address corrections of $\mathcal{O}(a_s^2)$ in H_0 and $\mathcal{O}(a_\tau)$ in $G(\mathbf{x},\tau+a_\tau)$ by means of

altering the link variables through

$$U_i(x) \to \frac{U_i(x)}{u_s} \quad U_4 \to \frac{U_4(x)}{u_\tau}. \tag{3.35}$$

Here, $u_{s,\tau}$ are the average space-like (s) and time-like (τ) links, the former is determined from the plaquette expectation value whereas the latter is actually just set to unity for the work of the FASTSUM collaboration [45].

Given that the energy scale m_q has been integrated out of the analysis, the masses that one extracts from NRQCD simulations need to be additively renormalised. One actually calculates the mass splitting between particles and thus one must set the scale using a known particle mass. For these works this is done by comparing a lattice measurement of the ground state mass of the S-wave vector state, Υ, to the physical value given in [46], and more recently [47]. The details of the lattice estimation of this value are explored in Section 4.6.1.

3.6 Configuration parameters

Both generations of the FASTSUM configurations use 2+1 flavours of dynamical sea quarks with stout-linked, clover-improved Wilson fermions and Symanzik-improved gauge fields. Their differences are presented in Tables 3.1 and 3.2 for generation-2 and generation-2L respectively; L is for light as that generation contains lighter sea quarks. More details of the set-up are elucidated in [27]. The tuning of the bare parameters and the lowest temperature configuration from each generation were kindly supplied by the Hadron Spectrum Collaboration [48–51].

N_τ	T [MeV]	T/T_{pc}	$N_{\text{configurations}}$
40	141	0.760	500
36	156	0.844	500
32	176	0.950	1000
28	201	1.086	1000
24	235	1.267	1000
20	281	1.520	1000
16	352	1.900	1000

Table 3.1: FASTUM generation-2 configuration parameters. Constant across all are the lattice size, $(24a_s)^3 \times N_\tau a_\tau$, with $a_s = 0.1205(8)$ fm, $a_\tau = 0.03506(23)$ fm, and thus $\xi = 3.444(6)$, pseudocritical temperature, $T_{\text{pc}} \approx 181$ MeV, and a pion mass of $m_\pi = 384(4)$ MeV. More details can be found in [27, 52]

N_τ	T [MeV]	T/T_{pc}
128	47	0.284
64	95	0.569
56	109	0.650
48	127	0.758
40	152	0.910
36	169	1.011
32	190	1.138
28	217	1.300
24	253	1.517
20	304	1.820
16	380	2.275

Table 3.2: FASTUM generation-2L configuration parameters. Constant across all are the lattice size, $(32a_s)^3 \times N_\tau a_\tau$, with $a_s = 0.1121(3)$ fm, $a_\tau = 0.003246(7)$ fm, and thus $\xi = 3.453(6)$, pseudocritical temperature, $T_{\text{pc}} \approx 167$ MeV, a pion mass of $m_\pi = 239(1)$ MeV, and $N_{\text{configurations}} \approx 1,000$. More details can be found in [27, 53].

Chapter 4

Spectral reconstruction

In this chapter, I introduce the problem of spectral reconstruction whereby in-medium properties of mesons are related to the two-point correlation function measured on the lattice. I will highlight how the extraction of these physical properties is hampered by spectral reconstruction being an ill-posed problem and thus the recovered spectra are not unique. Once this is established, I will provide more details of the calculation of the correlation functions and show that we can observe temperature dependence of the correlation functions themselves. Then the rest of the chapter will explore the approach of using maximum likelihood estimation to fit some physics-informed ansatze to the correlation functions in a way that alleviates the ill-posed nature of the reconstruction. This provides estimates of the ground state mass and width of the Υ and χ_{b1} at a range of temperatures.

The analysis of this chapter will be performed on the FASTSUM generation-2L ensembles.

4.1 Spectral reconstruction as an ill-posed inversion

In-medium properties of QCD bound states can be completely described by the spectral function, $\rho_\lambda(\omega, T)$, for a given channel indicated by λ, at an energy ω [54]. We expect the spectral function to change with temperature, T, but in a non-trivial way, a way which will be explored in this work[1]. The spectral function is not an observable that is measured on the lattice, however, it can be extracted from the meson correlator (whose name will be used interchangeably with *correlator* and *correlation function*) through the following integral transform [45]

$$C_\lambda(\tau; T) = \int_0^\infty \frac{d\omega}{2\pi} K(\tau, \omega; T)\rho_\lambda(\omega; T). \tag{4.1}$$

[1]The temperature dependence will often be dropped from the notation as it seldom enters analytic expressions.

The kernel, $K(\tau, \omega; T)$, is set by the theory that is being considered. For NRQCD the kernel is independent of temperature [55] and reads

$$K(\tau, \omega; T) = K(\tau, \omega) = e^{-\omega\tau}. \tag{4.2}$$

The zero momentum meson correlator is defined[2] as

$$C_\lambda(\tau) = \sum_{\mathbf{x}} \langle O_\lambda(\mathbf{x}, \tau) O_\lambda^\dagger(\mathbf{0}, 0) \rangle. \tag{4.3}$$

The operator, O_λ, which is known as a meson interpolator, is given in terms of quark fields, $q(x)$, and anti-quark fields, $\bar{q}(x)$, by the expression

$$O_\lambda(x) = \bar{q}(x) \lambda q(x). \tag{4.4}$$

The symmetry properties of λ define the channel represented by the correlator. For the two states considered in this work, Υ and χ_{b1}, $\lambda = \boldsymbol{\sigma}_j$ and $\lambda = (\boldsymbol{\sigma} \times \boldsymbol{\nabla})_j$ respectively; σ_i are the Pauli matrices (for three spatial dimensions given by $i = 1, 2, 3$), $j = 1, 2, 3$ to account for each of the spin-triplet states, and the covariant derivative operator is given by

$$\nabla_i q(\mathbf{x}, \tau) = \left[U_i(\mathbf{x}, \tau) q(\mathbf{x} + \hat{i}, \tau) - U_i^\dagger(\mathbf{x}, \tau) q(\mathbf{x} - \hat{i}, \tau) \right]. \tag{4.5}$$

Combining equations (4.1) and (4.2) one arrives at the spectral function and correlation function being related via a Laplace transform

$$C_\lambda(\tau, T) = \int_0^\infty \frac{d\omega}{2\pi} e^{-\omega\tau} \rho_\lambda(\omega, T). \tag{4.6}$$

Finding the inverse Laplace transform of a general function is, at best, a non-trivial task [56]. To further restrict the task of recovering $\rho_\lambda(\omega)$ from a given $C_\lambda(\tau)$ there is the fact that the resolution of the latter is entirely limited by computational resources. The correlation function is an observable in a lattice simulation, and with the current resource is sampled $\mathcal{O}(10 - 100)$ times. The resolution that one requires the spectral function to be sampled at in order to resolve narrow peaks is, at least, $\mathcal{O}(1000)$. Furthermore, measurements of $C_\lambda(\tau)$ are subject to error. The combination of these points makes spectral reconstruction an ill-posed problem [57,58]. The implications of this are that a large number of spectral functions could recreate the correlator data measured on the lattice, and thus any reconstructed spectral function is not unique.

[2] A word on notation: in Chapters 5 and 6 we will consider a 'point-split' meson correlator, $C(\mathbf{r}, \tau)$, which I mention here only for completeness. The form presented here will only exist in this chapter.

At this point, we have established the relationship between the correlator that we can measure on the lattice and the spectral function from which we can extract the physical properties of mesons. However, we have just seen that the inversion required to recover the spectrum, equation (4.6), is ill-posed. There are a plethora of approaches to circumvent this problem, from Bayesian methods: maximum entropy methods (MEM) [45,59–72] and the Bayesian reconstruction (BR) method [73, 74]; to the Backus-Gilbert method [75–78]; novel machine learning approaches [79–81]; and methods involving the fitting physics-inspired ansatze to the correlators [82–85]. In this work, we will use maximum likelihood estimation to fit interpretable ansatze to the correlators, and thus we are following the works from the final of the aforementioned methods; this is the first application of maximum likelihood estimation to extract the ground state width of mesons from FASTSUM ensembles. Maximum likelihood estimation allows us to extract the mass and width of bottomonium mesons at a variety of temperatures with a smaller number of free parameters than the number of points in the correlator, which alleviates part of the ill-posed nature. Finite measurement noise on observables cannot be avoided. First, however, I will develop some more of the necessary details for computing equation (4.3).

4.2 Correlation functions

4.2.1 Local and smeared correlation functions

Much of the subtlety of the calculation of the meson correlator is not needed for this work. For more details, the reader is directed to [16, 33]. One such subtlety that I will only briefly expand upon is in the introduction of the quark propagator (also referred to as the inverse Dirac operator), D^{-1}. Equation (4.3) is written here in a formal form, in Chapter 6 I will introduce an alternative form of calculating the meson correlator (albeit one must take $\mathbf{r} = 0$ to match equation (6.4) with this work) that contains D^{-1} and is the form one calculates in practice. This propagator is a very sparse and highly correlated matrix, therefore there is a lot of redundancy in its computation. Encapsulated in this matrix is the quark propagation from all possible 'source' points to all possible 'sink' points. A source (sink) can be considered the origin (end-point) of a quark's propagation, it has spacetime, colour, and Dirac indices. A particular source can be introduced such that we need only calculate a single column of the quark propagator, which is enough for the computation of meson correlators. The simplest source that achieves this is the *point source*, a δ-function in all indices localising the source to a single point in spacetime, colour, and Dirac index.

The meson interpolator was defined in equation (4.4). In theory, any operator

with the correct quantum numbers could act as a valid meson interpolator. In practice, however, the form can be optimised to give a stronger signal in the correlator. This will become more apparent later, in equation (4.13), when we see that the correlator is proportional to the overlap of the operator between the vacuum and state of interest. One way of increasing this overlap is in the choice of source. A source that mimics a realistic spatial wave function improves the overlap of the operator [16, 86]. These are known as *smeared* sources, and the same process applied to the sink gives a smeared sink. For this work, the smeared source/sink was created to have a strong overlap with the ground state in each channel, and thus one would expect fewer excited state contributions from a correlator built of a smeared source and sink. The details of the smearing used can be found in [27, 52, 53].

In this chapter, we will consider the correlator between a point source and point sink (so-called *local correlator*) and the correlator between a smeared source and identically smeared sink (called *smeared correlator*). All analysis will be done on both local and smeared correlators, and, in theory, the ground state parameters should remain the same between the two.

4.2.2 Temperature dependence of correlation functions

The goal of the maximum likelihood fits (which will be introduced in Section 4.3) is to track how the mass and width of bottomonium states change with temperature. We can, however, just at the level of the correlators, show that there are thermal effects in these lattice observables. We cannot attribute these to any physically interpretable changes in the states, but the benefit of observing changes at this level is that there are no modelling assumptions made yet.

Throughout this chapter, I will report results for the vector state, Υ, and the axial-vector state, χ_{b1}, as representative S-wave and P-wave states respectively. These are consistently reported by the FASTSUM collaboration so will lead to better comparison. As well as this, the Υ is much more precisely measured by the PDG of the two S-wave states, and, of the P-wave states, the χ_{b1} has the largest decay fraction into $\gamma\Upsilon(1S)$ which is a clear detection channel [47].

Figure 4.1 shows the local correlators for the representative S- and P-wave states. The statistical errors grow with time and are larger for χ_{b1} than Υ. The same is true for the smeared correlators shown in Figure 4.2. However, with the correlators spanning so many orders of magnitude, and with thermal effects being small, it is hard to notice any changes with temperature in this form.

To amplify any changes we consider the ratio of the of a correlator and the coldest correlator, this is shown in Figures 4.3 and 4.4. This is made easier by the NRQCD framework as there is no temperature dependence in the kernel. Some immediate observations from Figure 4.3 are that the thermal effects are present

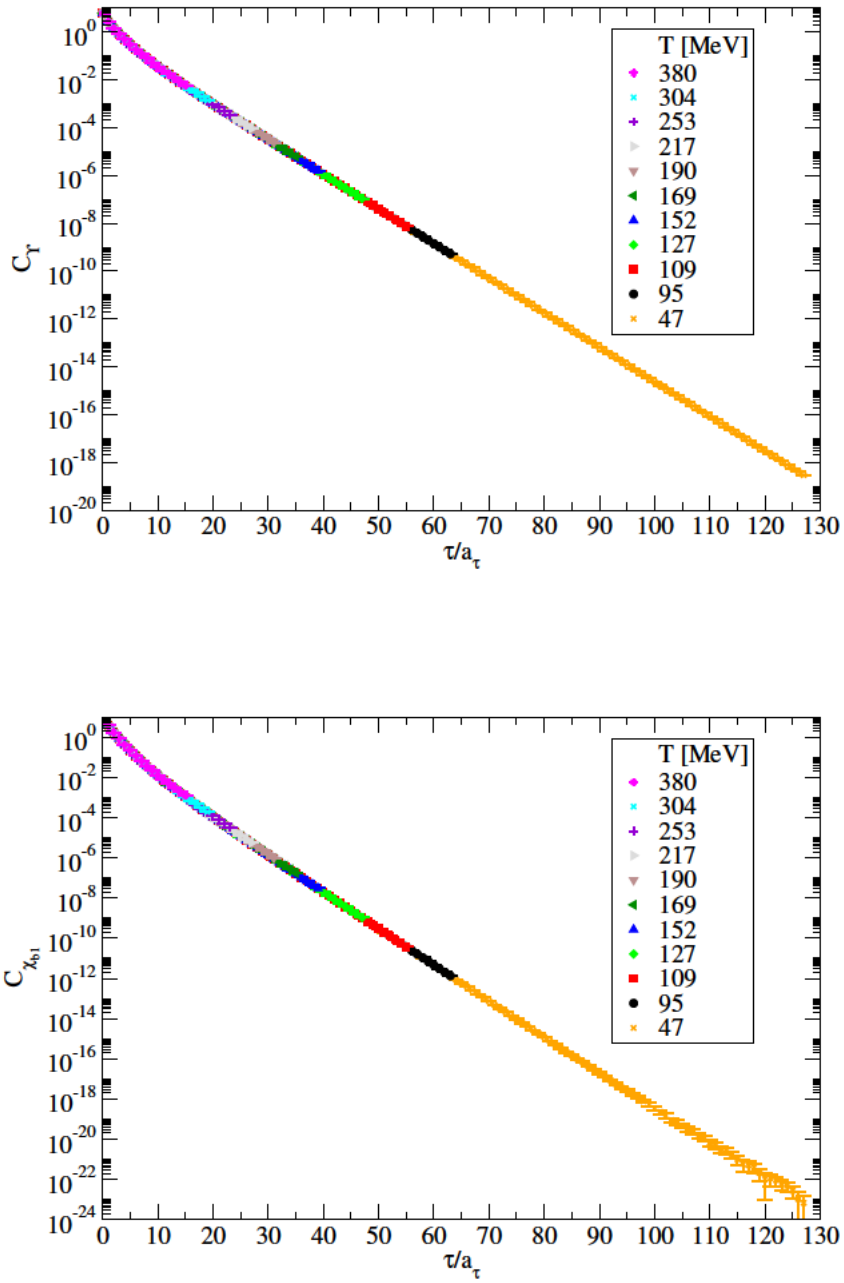

Figure 4.1: *Local* correlators for the S-wave vector state Υ (top) and P-wave axial vector state χ_{b1} (bottom) at a range of temperatures. The errors shown are statistical.

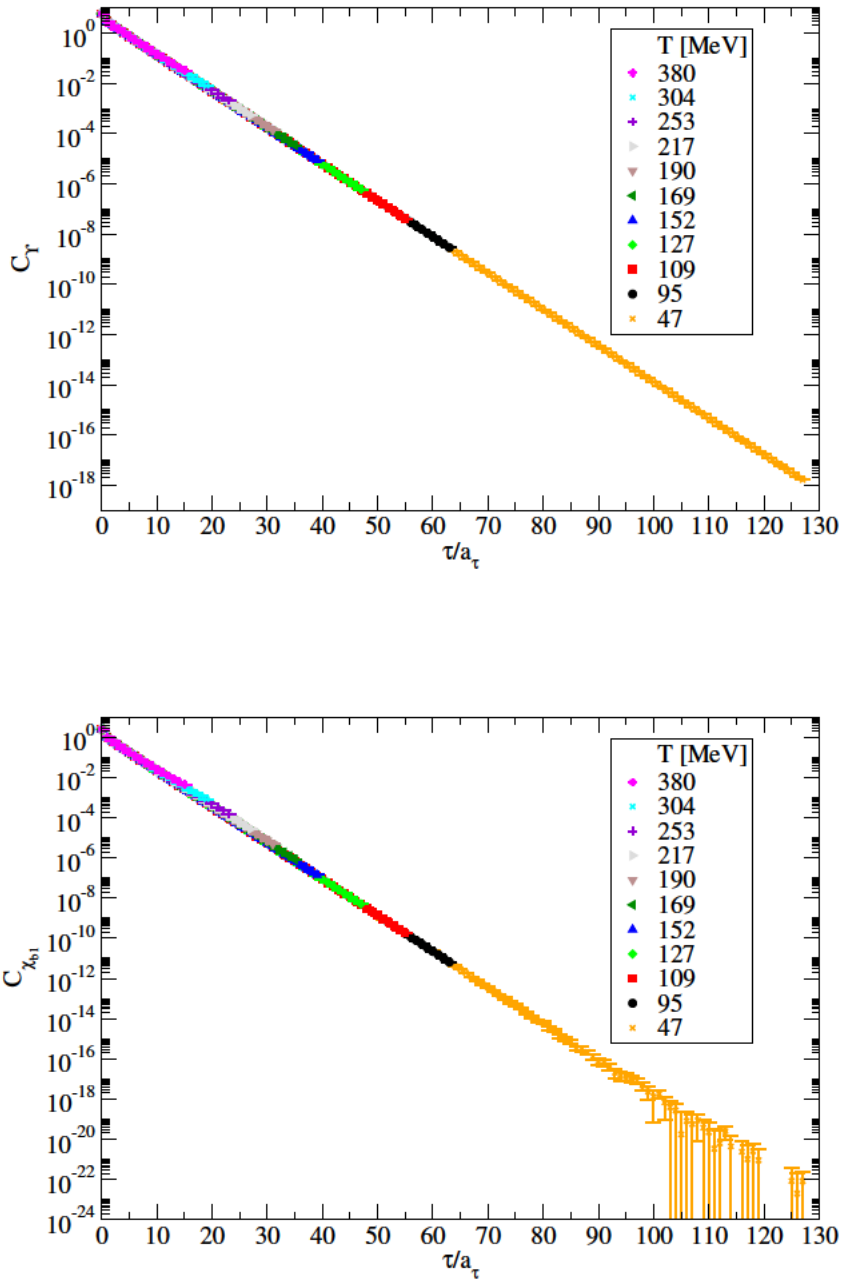

Figure 4.2: *Smeared* correlators for the S-wave vector state Υ (top) and P-wave axial vector state χ_{b1} (bottom) at a range of temperatures. The errors shown are statistical.

in all correlators, yet they are larger for the χ_{b1}, as are the statistical errors. With the exception of the correlators measured on the two coldest lattices, which cannot be resolved within errors, there is a systematic change of the correlators with temperature. Very early times notwithstanding, the correlators are larger for hotter simulations. The same behaviour is evident in the ratio of the smeared correlators to the coldest smeared correlator (see Figure 4.4).

One can also consider the effective mass, defined as

$$M_{\text{eff}}(\tau) = \ln\left(\frac{C(\tau)}{C(\tau+1)}\right), \tag{4.7}$$

to observe thermal effects. The details of the renormalisation of the masses extracted from these NRQCD simulations are postponed until Section 4.6.1, however, the result is that the effective mass, in GeV, is related to the values reported in this section, $M_{\text{eff}}\, a_\tau$, through

$$M_{\text{eff}}[\text{GeV}] = M_{\text{eff}}\, a_\tau \times a_\tau^{-1}[\text{GeV}] + 7.463. \tag{4.8}$$

The value of $a_\tau^{-1}[\text{GeV}]$ for the generation-2L configurations was determined using the mass of the Ω baryon in [51], it was found that $a_\tau^{-1}[\text{GeV}] = 6.079$ GeV.

Figure 4.5 shows the effective mass of the Υ and χ_{b1} states from the local correlators. From this we see that the thermal effects and errors are larger in the χ_{b1} correlator: the thermal effects are best seen by the difference between the data in the range $\tau/a_\tau \sim 10 - 30$. It is important to point out that for $T > 127$ MeV the effective mass does not seem to have reached a plateau, therefore, for these temperatures there is no significant ground state dominance even at late times. However, they do appear to be following the behaviour of the colder lattices: tending towards a plateau within a few per cent of each other.

The effective mass of the smeared correlators tells a different story. For both S- and P-waves, shown in Figure 4.6, the different temperatures do not appear to be converging on the same value. The approximate value of the plateau for the $T = 47$ MeV lattice does not seem to have changed from the case of local correlators, as we would hope. Nevertheless, the behaviour of bending downwards of the hotter lattices was not present in the local correlators. This is indicative of two possible causes: either the smearing used is not appropriate (the smearing function had a poor overlap with the ground state), or the thermal width of the ground state is more pronounced in the smeared data. Fine-tuning the smearing of these correlators lies outside the scope of this work. The latter cause, however, can be explored here. Given that the relation between the spectral function and correlation function is a Laplace transform, one can think of the effect of finite width as follows: as τ increases, the exponential suppression of higher energies increases, this means the dominant contribution to the effective mass comes from

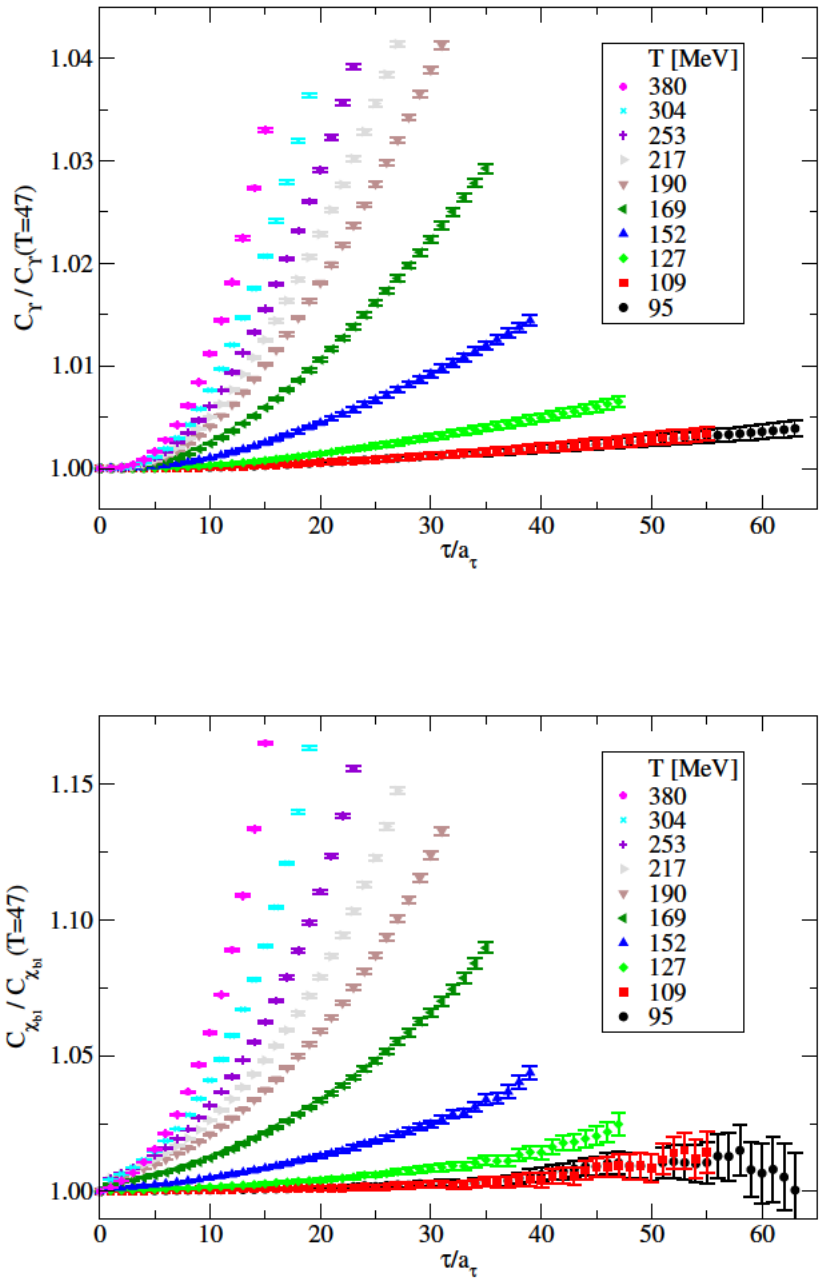

Figure 4.3: Relative *local* correlators for the S-wave vector state Υ (top) and the P-wave axial vector state χ_{b1} (bottom). Each colour is a correlator at a different temperature relative to the coldest temperature available, $T = 47$ MeV. The errors shown are statistical.

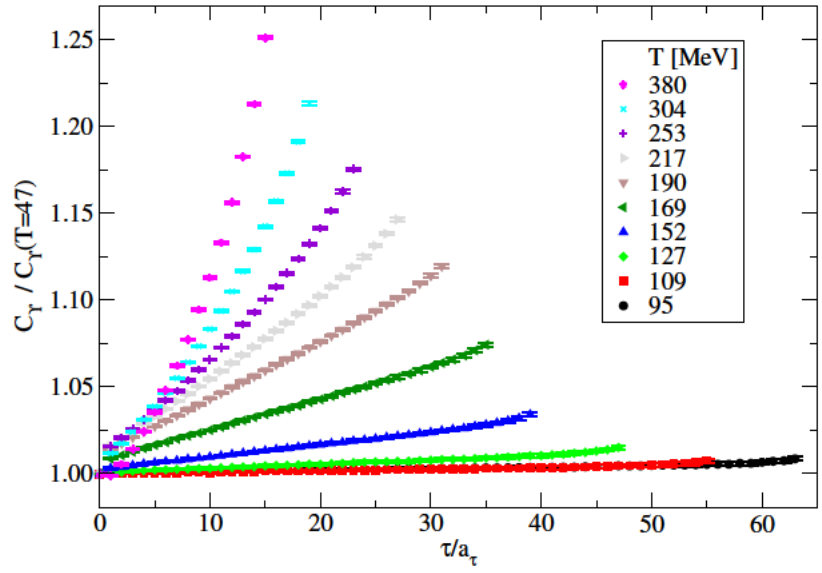

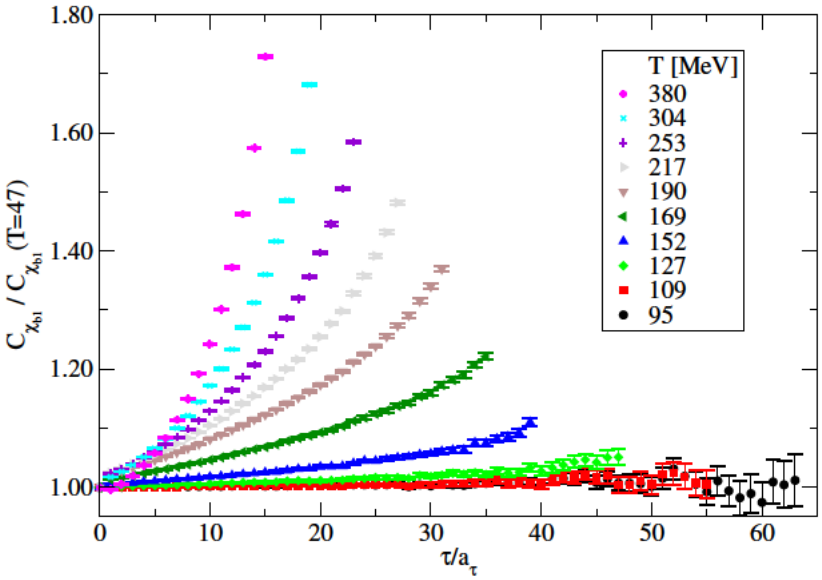

Figure 4.4: As in Figure 4.3 but for smeared correlators.

further and further down the low-energy tail of the broad distribution and thus it appears like a lower and lower energy peak, therefore the effective mass decreases with time. We can't attribute this behaviour directly to ground state parameters, but, providing the smearing is appropriate, it is suggestive that the ground state width increases with temperature in the smeared correlators. This argument is developed in Appendix A where we consider the behaviour of the effective mass for a correlator of a known form.

4.3 Maximum likelihood for spectral reconstruction

The previous section established that there are temperature dependent effects present in the correlation functions. Also, we could see from the effective mass that the mass, and to some extent the width, of the ground state could explain the temperature dependence of the correlators. In this section, we will explore this behaviour in more detail by developing three ansatze in order to use maximum likelihood estimation to extract the ground state mass and width at various temperatures.

4.3.1 Developing the ansatze

A natural starting point is to see what we can glean about the form of the correlator in the special case of zero temperature. We begin by introducing the definition of the Euclidean two-point correlation function [16],

$$\langle O_2(\tau)O_1(0)\rangle = \frac{1}{Z}\mathrm{Tr}\left[e^{-(aN_\tau-\tau)\widehat{H}}\widehat{O}_2 e^{-\tau\widehat{H}}\widehat{O}_1\right]. \tag{4.9}$$

The length of the temporal extent is aN_τ, the Hamiltonian is given by $\widehat{H}$, and the normalisation factor $Z = \mathrm{Tr}\left[e^{-aN_\tau\widehat{H}}\right]$ can be identified with the partition function in statistical mechanics. To be explicit about the trace we introduce a complete set of Fock states, $|n\rangle$, that are eigenstates of the Hamiltonian, leaving

$$\langle O_2(\tau)O_1(0)\rangle = \frac{1}{Z}\sum_n \langle n|e^{-(aN_\tau-\tau)\widehat{H}}\widehat{O}_2 e^{-\tau\widehat{H}}\widehat{O}_1|n\rangle. \tag{4.10}$$

One can introduce a second complete set of states $|m\rangle$ for convenience such that

$$\langle O_2(\tau)O_1(0)\rangle = \frac{1}{Z}\sum_{m,n} \langle n|e^{-(aN_\tau-\tau)\widehat{H}}\widehat{O}_2 e^{-\tau\widehat{H}}|m\rangle\langle m|\widehat{O}_1|n\rangle \tag{4.11}$$

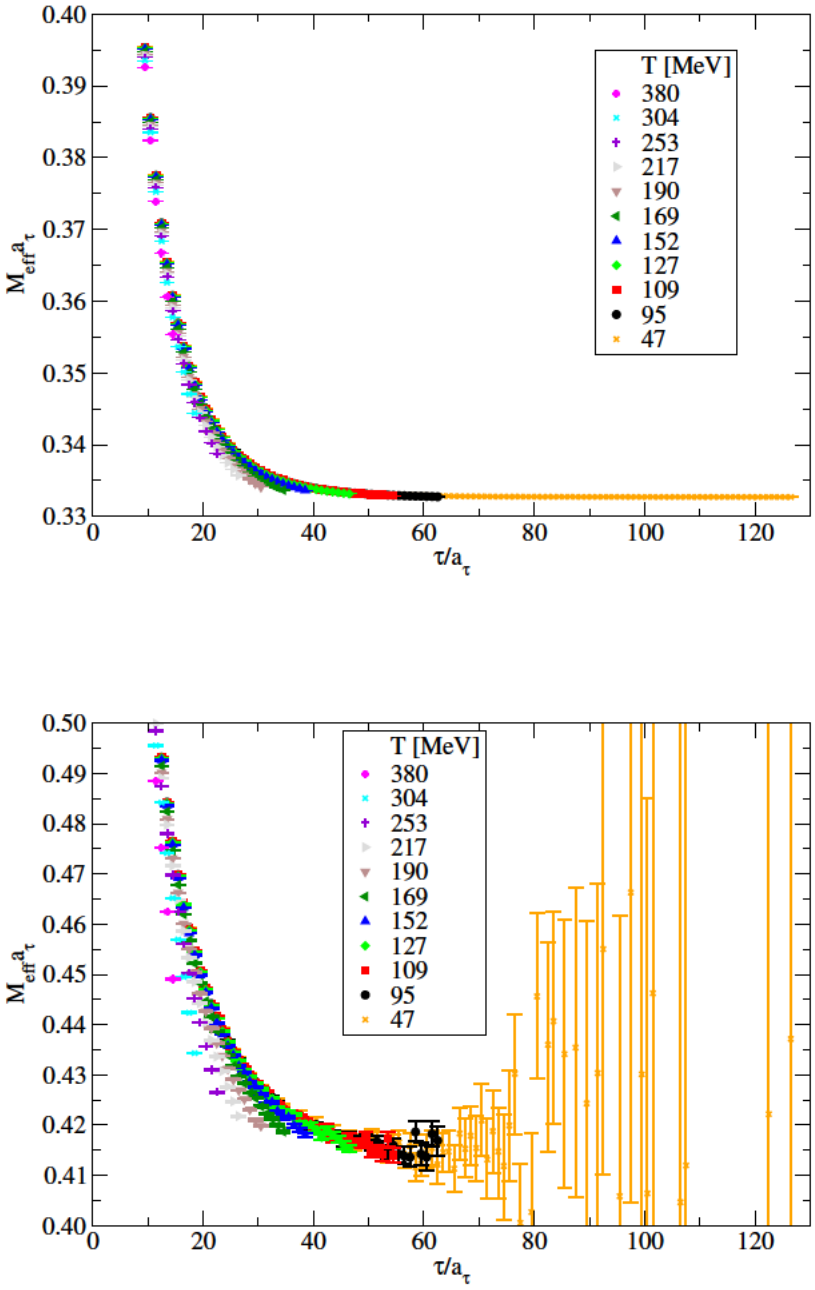

Figure 4.5: The effective mass defined in equation (4.7) for the Υ (top) and χ_{b1} (bottom). Both were generated from local correlators. The statistical errors underestimate the error at large times: the logarithm is not always defined as the correlator can be negative within errors (see Figure 4.2). These undefined values are not incorporated into the error estimate.

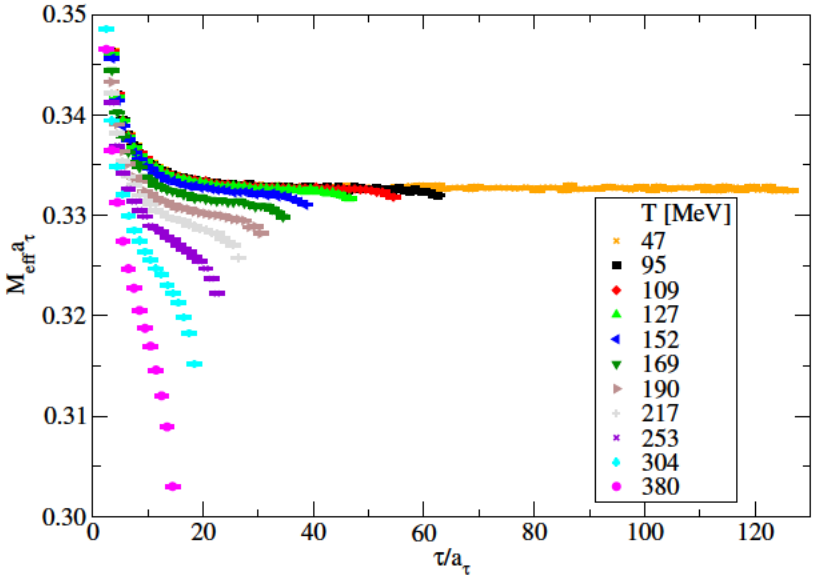

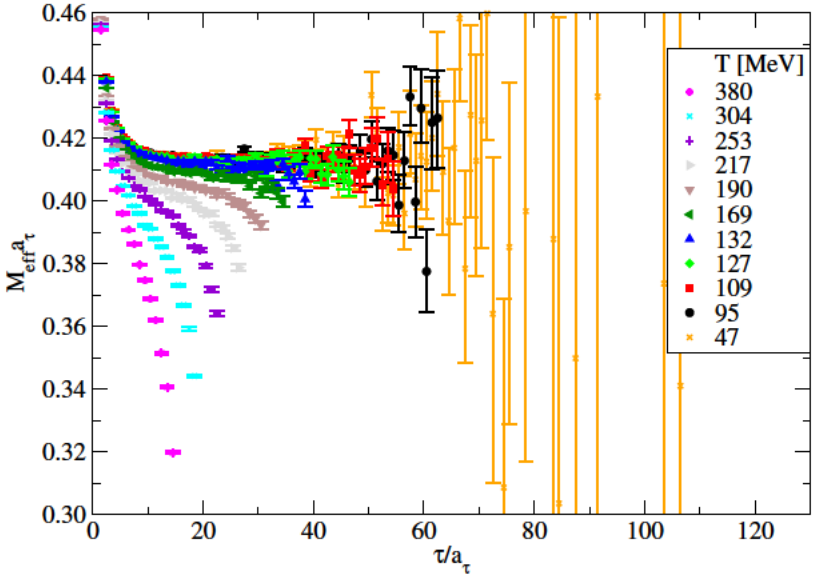

Figure 4.6: As in Figure 4.5 but for smeared correlators.

and then act on these states with the Hamiltonian operator to write this in terms of eigen-energies

$$\langle O_2(\tau)O_1(0)\rangle = \frac{1}{Z}\sum_{m,n} e^{-(aN_\tau-\tau)E_n} e^{-\tau E_m} \langle n|\widehat{O}_2|m\rangle\langle m|\widehat{O}_1|n\rangle. \tag{4.12}$$

In the case where $\widehat{O}_1 = \widehat{O}_2$ (which is the case for the meson correlators explored in this work) and in the limit $aN_\tau \to \infty$ (zero temperature) we arrive at

$$C_\lambda(\tau) = \sum_n |\langle 0|\widehat{O}_\lambda|n\rangle|^2 e^{-E_n\tau}. \tag{4.13}$$

Where $|0\rangle$ represents the vacuum whose energy, E_0, is normalised to 0.

One can see that when the relationship between the correlator and the spectral function is a Laplace transform, then a spectral function that is a sum over δ-functions would recover a correlator in the form of (4.13).

With the previous result in mind, and following a similar process to that laid out in [83], we consider the energy spectrum of an NRQCD meson to consist of a set of δ-functions, *peaks*, with the lowest energy peak corresponding to the ground state and all higher peaks being that of excited states. In the infinite volume limit (*i.e.* the thermodynamic limit) we would expect some of these higher energy peaks to form a continuum, and thus it is reasonable to prescribe the following representation of the spectrum

$$\rho(\omega) = 2\pi \sum_i A_i \delta(\omega - M_i) + \theta(\omega - s_0)\rho_{cont}(\omega), \tag{4.14}$$

where $\theta(\omega - s_0)$ is the Heaviside step function and A_i is related to the overlap between the meson interpolator and the Fock states (see equation (4.13)). This splits the spectrum into two parts: a part that would comprise the continuum in the infinite volume limit, $\rho_{cont}(\omega)$, and then a sum over the remaining states indexed by i. We assume that the continuum behaviour would only contribute above some threshold energy, s_0.

To further simplify this expression we consult the exponential suppression of the high-energy contributions to the spectral function shown in equation (4.2), noting that this suppression means that only a small number of early time lattice points are sensitive to the nature of ρ_{cont}. By not placing much emphasis on these early times we can neglect the continuum contribution and continue to simplify the functional form we expect for the spectrum.

Further pushing the exponential suppression of the higher energies we can consider the spectrum a combination of ground state and excited state contributions, without really speculating about this excited state behaviour but simply

postulating that the spectrum will look like

$$\rho(\omega) = 2\pi A\delta(\omega - M) + \rho_{excited}(\omega), \tag{4.15}$$

where all the behaviour that is not captured by the ground state peak is amalgamated into a single spectral function $\rho_{excited}(\omega)$. The excited state behaviour is inherently a higher energy feature and thus suffers from more suppression. This is the final form of how we expect the spectrum to look at finite volume and strictly zero temperature.

To adjust our above reasoning to the non-zero temperature spectrum, we simply ask how the increase in temperature would affect equation (4.15). The non-zero temperature spectrum takes the general form

$$\rho(\omega) = \rho_{ground}(\omega) + \rho_{excited}(\omega), \tag{4.16}$$

with each term on the right-hand side to be parametrised by an ansatz.

The simplest ansatz that one could suggest given equations (4.15) and (4.16) is

$$\rho(\omega) = 2\pi A\delta(\omega - M). \tag{4.17}$$

This would allow us to fit the ground state mass, M, and the overlap prefactor A.

The next order of complexity could be either to: include thermal broadening of the ground state, or to include excited states. The latter will be postponed for the moment. To arrive at the next most natural ansatz, the δ-function is generalised to include a width,

$$\rho(\omega) = \frac{\sqrt{2\pi}}{\Gamma} A e^{-\left(\frac{\omega - M}{\sqrt{2}\Gamma}\right)^2}. \tag{4.18}$$

The third parameter, Γ, is the width of the state. A changing width could be caused by thermal effects or a finite lifetime of the state. Whilst [83] parameterise the broadening with a Lorentzian, significantly distinguishing the two at the level of numerical errors present in our lattice simulations is unclear. As will be shown in equation (4.21) the Gaussian has a closed form inverse Laplace transform and thus gives a simple ansatz.

Finally, for this analysis, we add the simplest extra term to represent the excited states and arrive at the most complex ansatz considered,

$$\rho(\omega) = \frac{\sqrt{2\pi}}{\Gamma} A_1 e^{-\left(\frac{\omega - M_1}{\sqrt{2}\Gamma}\right)^2} + 2\pi A_2\delta(\omega - M_2), \tag{4.19}$$

where it is understood that $M_2 > M_1$.

We can formulate the correlation functions that would correspond to the spectral functions given in equations (4.17), (4.18), and (4.19) using the Laplace transform given in equation (4.6). These lead to three distinct ansatze, or models, to compare to the correlator data:

$$C(\tau; A, M) = Ae^{-M\tau} \tag{4.20}$$

$$C(\tau; A, M, \Gamma) = Ae^{-\tau\left(M - \frac{\Gamma^2\tau}{2}\right)} \tag{4.21}$$

$$C(\tau; A_1, M_1, \Gamma, A_2, M_2) = A_1 e^{-\tau\left(M_1 - \frac{\Gamma^2\tau}{2}\right)} + A_2 e^{-M_2\tau}. \tag{4.22}$$

I will refer to the ansatze in equations (4.20), (4.21), and (4.22) as the two-, three-, and five-parameter ansatze respectively.

The Laplace transform in equation (4.6) is over half of the real line ($\omega \in [0, \infty]$), however, this leads to a more complex ansatz when it comes to the Gaussian terms. In Section 4.3.3 we will explore how each of the parameters in these correlator ansatze can be seeded from intuitive arguments, however, this is much more difficult if we perform the integral over only half the real line due to the increased complexity of the ansatz. We instead opt to extend the range of integration to all real $\omega \in [-\infty, \infty]$ and arrive at the ansatze shown in equations (4.21) and (4.22). This simplification is discussed in Appendix A where it is shown that the simpler forms of the ansatze do not differ from the true forms by more than a few percent.

Now that we have established some ansatze that we would like to fit to our correlators, I will cover some of the statistics underpinning maximum likelihood estimation such that we can determine the values of the physical parameters.

4.3.2 Maximum likelihood statistics

The likelihood that a given model, $y(x; \theta)$, with a number of tunable parameters, θ, 'fits' data, $\mathcal{D} = \{x_i, y_i\}$, is denoted $L(y(\theta)|\mathcal{D})$. It describes the probability density that the model, with specific parameters, would take the values of the data. One approach to finding the best model to represent data is to maximise this likelihood function.

To illustrate the way in which we find the parameters that maximise the likelihood we consider the following example: each datum, y_i, is independent and has measurement error, σ_i, drawn from a Gaussian. We consider the likelihood in this case, i.e. the probability that each datum being drawn from an independent Gaussian centred at the model's predicted value, $y(x_i; \theta)$, gives the measured value, y_i, plus or minus some small, constant interval dy. This is

$$L(y(\theta)|\mathcal{D}) = \prod_i \left[e^{-\frac{1}{2}\left(\frac{y_i - y(x_i;\theta)}{\sigma_i}\right)^2} dy \right]. \tag{4.23}$$

Then, if we define the least squares error as,

$$\text{Least squares error} = \sum_i \left(y_i - y(x_i;\theta)\right)^2, \tag{4.24}$$

it becomes clear that one can maximise the likelihood by minimising the least squares error: the maximum of the likelihood function is when the exponent is minimised, and this exponent is minimised when $\sum_i \left(y_i - y(x_i;\theta)\right)^2$ is minimised (for a fixed σ_i). Finally, to conclude I will define the χ^2 statistic as

$$\chi^2 = \sum_i \left(\frac{y_i - y(x_i;\theta)}{\sigma_i}\right)^2. \tag{4.25}$$

Minimising this quantity gives the same best-fit parameters as maximising the likelihood. The χ^2 per degree of freedom, which will be denoted χ^2_ν, is often reported as a means to compare between models of differing complexity.

Measurements on the lattice are not independent, there are spatial and temporal correlations in the gauge fields as well as correlations between configurations within the ensemble. These all propagate into the correlator. The spacetime correlations come from both the physical correlation of the system and from only applying local updates to gauge fields during a single step of the accept/reject algorithm. The correlations between configurations come from the autocorrelations in the Markov chain itself. Nevertheless, in a more general sense than what was laid out above, χ^2 minimisation leads to the same estimating equations as maximum likelihood estimation [87] and thus the correlations do not undermine our approach of χ^2 minimisation. So, despite not applying directly here, equations like (4.23) contextualise how the parameters fit by χ^2 minimisation correspond to the most likely model to fit the data.

The fits in this chapter do not account for correlations between the data at different times, and are called *uncorrelated* fits; the cause of these correlations is that at all times the correlation function is generated from the same gauge field. Dealing with such correlations in lattice calculations is difficult (see, for example, the discussions in [88]). To ignore correlations is also known as the diagonal approximation, as one assumes that the covariance matrix, defined as

$$S_{ij} = \frac{1}{N-1}\sum_{n=1}^{N}(y_i(n) - \bar{y}_i)(y_j(n) - \bar{y}_j), \tag{4.26}$$

is non-zero only along the diagonal. Here we have defined the samples of set i to be $y_i(n)$, of which there are N, and their mean is $\bar{y}_i$; the same is true for the index j. Another common method for tackling the problems with correlated fits is to perform singular value decomposition (SVD) cuts; by this it is meant

that one removes the contribution to the covariance matrix that corresponds to the smallest eigenvalue, as this eigenmode will dominate the calculation of the correlated χ^2. Using either the diagonal approximation or SVD cuts changes the physical meaning of χ^2, and the impact on this work is that our uncorrelated χ^2 will be underestimated. As a final comment, one expects that the χ^2_ν from a full, correlated, fit should lie around 1 if the fit is valid [89]; thus in the uncorrelated fits of this work we would expect slightly below 1.

The ansatze in equations (4.20), (4.21), and (4.22) take the form of the model in equation (4.23) and the normalisation, mass, and width in these ansatze are the parameters to be fit by this maximum likelihood minimisation.

4.3.3 Fitting algorithm

The χ^2 landscape, i.e. χ^2 as a function of all fit parameters, θ, is highly multimodal, and the gradient of this landscape spans many orders of magnitude. These factors make for a hard time minimising $\chi^2(\theta)$.

Given that the gradient is so varied we opted for the *Nelder-Mede* algorithm (often called the *simplex* algorithm) as it only involves evaluations of the function, and no information of the derivative is required [90].

As for the multimodality, this is a more challenging problem to solve, we chose to tackle this in two ways. Firstly, the algorithm for fitting the spectrum contains many physics-informed seeding routines to ensure that we begin the fit closest to where we would expect the global minimum to be. This is a clear bias, albeit an intuitive one. With that being said, we never restrict the fit parameters to lie in specific ranges for the final optimisation, and thus if there were a global minimum elsewhere then the parameters are able to find it, in theory. Secondly, once we have found a minimum, we perturb the best-fit parameters slightly and rerun the minimisation routine. We do not consider the minimum to be global if the same minimum is not found the second time. It should be noted, however, that neither method completely alleviates the problem of a multimodal landscape.

We explore three fitting functions in this work. However, I will only outline the fitting procedure for the five-parameter ansatz (equation (4.22)), as the other ansatze follow the same procedure, only they terminate after seeding fewer parameters. Therefore, I will be seeding the following parameters: A_1, M_1, Γ, A_2, and M_2. The following algorithms will be based on heuristic arguments.

We begin with the intuition that eventually the ground state will dominate the correlator, and we call the times for which this is the case, late times. Therefore, at these late times, a single exponential ansatz for the correlator should be suitable (thus assuming $C(\tau) = A_1 \exp(-M_1\tau)$). With this in mind, we perform linear regression on the logarithm of the correlator at late times, the gradient and y-intercept can be trivially related to A_1 and M_1 through

$$\ln C(\tau) = -M_1\tau + \ln A_1. \tag{4.27}$$

To seed the third parameter, Γ, we begin with A_1 and M_1 fixed to the values they were just seeded to. We then take the Gaussian fit function from (4.21) and fit Γ using a single dimensional golden section search [89]. This one-dimensional fit is simpler than if all three parameters were being varied at once to find their optimal values. However, once Γ has been seeded then we do allow A_1, M_1, and Γ all to vary and optimise these parameters using the simplex algorithm. This is also fit to the correlator at late times to avoid excited state contributions.

Seeding A_2 and M_2 requires more steps. Firstly, we use the seed parameters of A_1, M_1, and Γ and create something approximating a 'ground state correlator' by use of equation (4.21), this is created for all times in the time window. We then remove this from the full correlator, leaving, if the three parameters were perfectly fit, only excited state contributions. Finally, linear regression is performed on the logarithm of this remaining correlator to seed A_2 and M_2, analogous to the seeding of A_1 and M_1.

These seeding steps are vital to fitting the ansatz to data and are essentially required due to the complexity of the problem. However, the heuristics that motivate them are imperfect and this leads to failures for known reasons. Firstly, if the data contains too large a contribution from excited states then the final five-parameter fit often does not converge to a stable minimum. This does not affect the seeding of the first three parameters as they are fit to late times where these excited states are suppressed. However, if the ansatz chosen contains only the three parameters (equation (4.21)) then the final fitting step to the entire time window can also fail to converge due to excited states. This failure often occurs when the time window starts too soon. The second known cause of failure is if the excited state contribution is too small. In this case, when trying to remove the ground state contributions from the total correlator (the penultimate seeding step) there can be negative values in the correlator. These negative values cause the logarithm of the correlator to be undefined at certain points, and thus the linear regression step fails. This kind of failure occurs when the time window starts too late, and was found to be particularly common when fitting to smeared correlators.

4.4 Time window effects

As the method used by the FASTSUM collaboration is to change temperature with a fixed scale approach (meaning that the temperature is changed by changing the number of sites in the time dimension, see Section 3.4), there are inherent

systematic effects when making comparisons across different temperatures. Different temperatures correspond to correlators defined on differing numbers of temporal points. Moreover, even without the systematic effect of the fixed scale approach, the relative contributions of energy levels change with time: estimating the ground state parameters at, for example, $\tau = 15a_\tau$, where there are large excited state contributions, compared to at $\tau = 127a_\tau$, where such contributions are negligible, is unwise. This can easily be seen by how much the effective mass changes with time, like in Figure 4.5.

There are two solutions to reduce these systematic effects: one could attribute a systematic error to each measurement that accounts for varying the time window, or one could also make comparisons only between measurements taken from the same time window. Both have their merits. The former allows the result to be quoted out of the context of the specific time window in which it was measured. The latter allows for better comparisons to be made within the data at the same time window: the data would be left with only statistical errors and thus one can resolve smaller significant differences between results at different temperatures. Both approaches will be used in this work, Section 4.6.2 contains the comparisons between data with the same time window and Section 4.6.3 reports the data after the time windows dependence has been extrapolated out and integrated into a systematic and statistical error.

For both methods, it still makes sense to analyse the data over a time window that reduces the size of the systematic effects. The remainder of this section will be dedicated to finding a time range, comprised of a start and end, τ_1 and τ_2 respectively, that minimises the dependence of the fitted values on the time range.

4.4.1 Start time, τ_1

The smallest temporal extent considered in this work is $N_\tau = 16$. One would assume that as all temperatures contain the range $\tau/a_\tau = [0, 15]$ then there is no reason to exclude any in this data. This is not the case. One such reason is that during our heuristic arguments leading to the ansatze under investigation (Section 4.3.1) we relied on the exponential suppression of high energy features affecting only early times. In other words, we required insensitivity to early time features of the correlator in order to develop our ansatze. Another reason is that in NRQCD the correlator at $\tau = 0$ is simply an initial condition (see Section 3.5) and thus does not contain any relevant physics.

Conversely, if the start time is too late then we do not capture enough excited state contributions in the correlator and the fits fail to converge (as was spoken of in Section 4.3.3). Given then, that the choice of τ_1 is more like a balance of how much excited state contribution to include in the correlator, we can see how

this affects fitted values of the ground state mass over different time ranges for local as well as smeared correlators.

For this analysis, we will be using the ansatz given by equation (4.22). Figure 4.7 shows the ground state mass recovered from fits to the correlators at different values of τ_1 and τ_2. The top panel shows the fitted mass for both local and smeared correlators with differing τ_1 being given by different colours. The bottom panel of this figure shows the same analysis but for only the smeared correlators, zoomed in as they vary on a smaller vertical scale. From Figure 4.7 we can clearly see that for local correlators the choice of τ_1 greatly impacts the fitted value of the ground state mass. This effect is present, however markedly reduced, in the smeared correlator; it is assumed that the effect is mitigated by the smearing suppressing the excited state effects that are causing these systematic changes. To disentangle physics from systematics, these plots consider a single temperature and show how the choice of τ_1 provides robustness against the choice of τ_2. A general trend exists that the larger τ_1, the more stable the fit of the ground state mass is upon changing τ_2. This reaffirms the notion that at later τ_1, the excited state contributions provide less of an impact on the fit. The limit is clear, however. For the local correlator, one cannot fit in the range $(\tau_1, \tau_2) = (10, 15)a_\tau$, likewise for the smeared correlator in the range $(5, 15)a_\tau$. These are both one extreme of the balance that we are trying to draw: the balance between the stability of the fit and enough data to perform the fit. Fortunately, the difference in Figure 4.7 between the second-largest τ_1 and the largest, for local and smeared, is small. So, not much stability is lost by reverting to the τ_1 values that allow for analysis of all time ranges.

Another thing we can probe to assess the optimal time range is the quality of the fits. We will consult the χ^2_ν for a given time range, as well as the ratio of the best fit over the correlators. The former will be the goodness-of-fit parameter that will best define the quality, but the latter gives a more visual representation. For this investigation, we chose a single temperature, $T = 95$ MeV ($N_\tau = 64$), which is the coldest lattice that does not suffer from large errors at large times. Figure 4.8 shows the ratio of the fitted correlator to the actual correlator for both Υ and χ_{b1}, local and smeared, for a range of start times, τ_1. From this figure we can see that the best fits always favour the largest τ_1. This is reaffirmed by Table 4.1 that reports the χ^2_ν for a range of fits. Therefore the time ranges that the χ^2_ν would suggest for both correlators are as late as possible. I also note that the fits to smeared correlators are of much higher quality than to local correlators.

With that being said, one can see from Table 4.1 that although the five-parameter ansatz leads to a better fit than the three-parameter ansatz, the χ^2_ν for the fits to the local correlator are significantly larger than 1. Further compounding this is that the values reported are assuming uncorrelated data, and thus the true χ^2_ν would be larger.

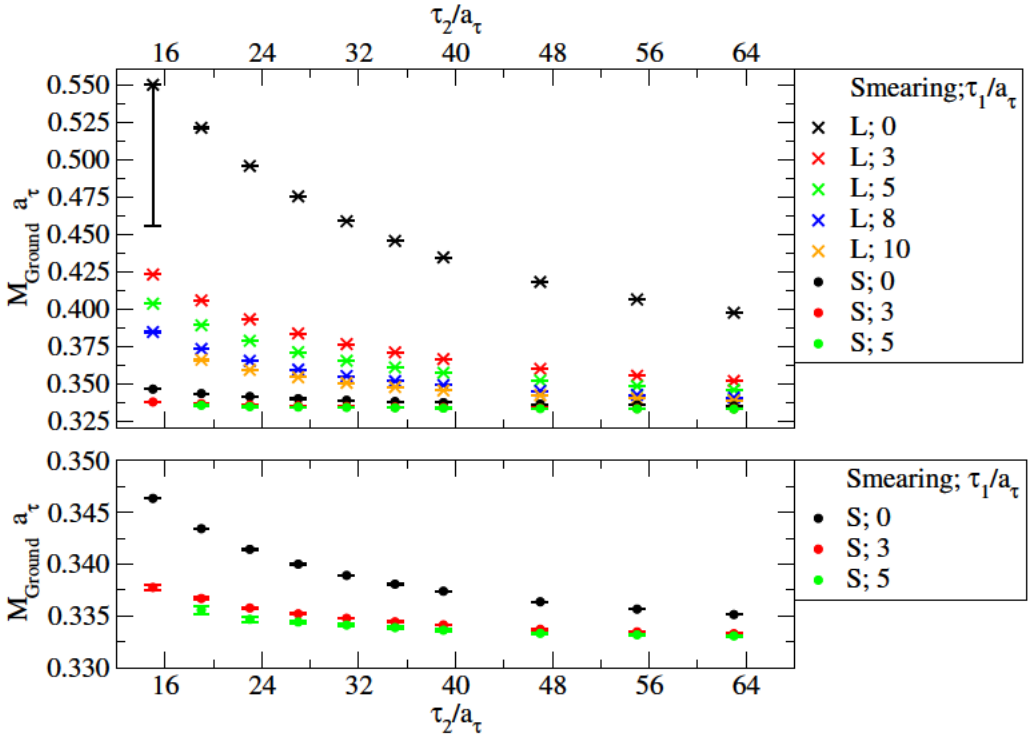

Figure 4.7: The effect that the choice of starting time window time, τ_1, has on the robustness of the fits of the Υ ground state mass (when the ansatz from equation (4.22) used). Fits are performed on the same data, the $T = 47$ MeV ($N_\tau = 128$) correlator, only varying τ_1 (in legend) and τ_2 (along the horizontal axis). Shown both for local (L) and smeared (S) correlators. The full data is presented (top) as well as a zoom into the smeared data (bottom). Clearly, the value of the mass is dependent on the end of the time window, τ_2, but to a lesser degree for certain τ_1 values. The effect is reduced for smeared correlators. The datum with a large error shows the instability of the algorithm when the time range is too short and the excited state contributions are too large.

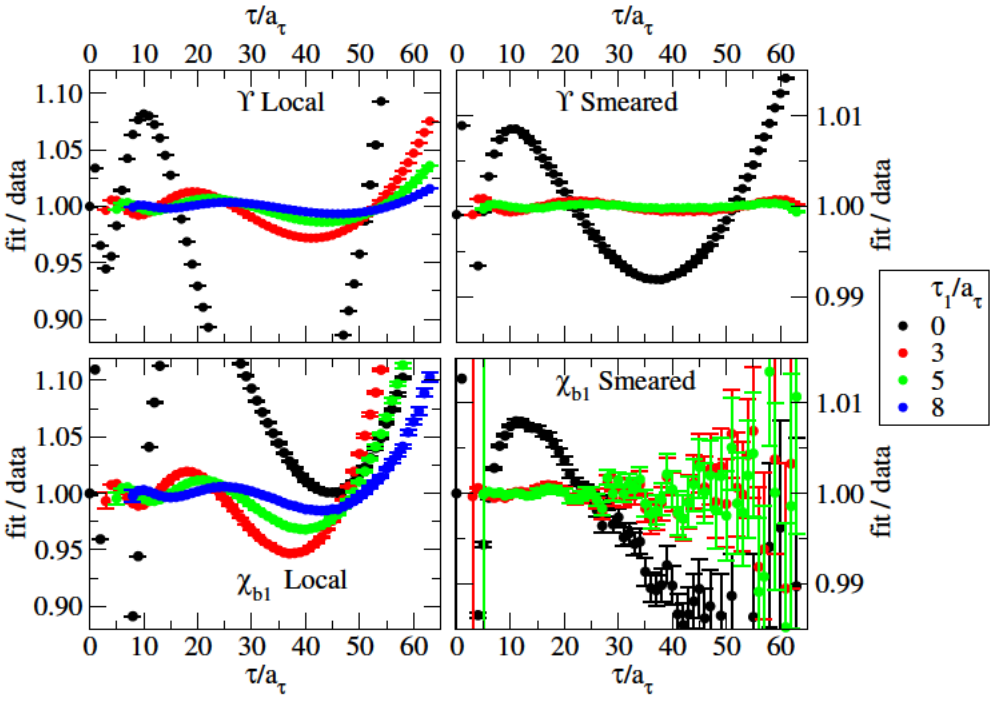

Figure 4.8: The ratio of the best fit correlator ansatz (using equation (4.22)) and the correlator measured on the lattice over the range τ_1 (given by colour and legend) to $\tau_2/a_\tau = 63$. For local (left) and smeared (right) $T = 95$ MeV ($N_\tau = 64$) correlators, and for Υ (top) and χ_{b1} (bottom). In all cases the later τ_1 the better the fit. Smeared also always leads to a better fit, however, the fits from $\tau_1/a_\tau = 8$ were not always possible for smeared correlators.

Type	State	τ_1/a_τ	Three-parameter χ^2_ν	Five-parameter χ^2_ν
Local	Υ	0	N/A	1501758
Local	Υ	3	7607046	10174
Local	Υ	5	2815462	2093
Local	Υ	8	669946	242*
Local	Υ	10	150690	N/A
Local	Υ	12	63862	N/A
Local	χ_{b1}	0	N/A	734105
Local	χ_{b1}	3	630451	1662
Local	χ_{b1}	5	278905	427
Local	χ_{b1}	8	84041	65*
Local	χ_{b1}	10	38822	N/A
Local	χ_{b1}	12	18458	N/A
Smeared	Υ	0	36711	368
Smeared	Υ	3	705	1*
Smeared	Υ	5	276	0.2
Smeared	Υ	8	87	N/A
Smeared	Υ	10	24	N/A
Smeared	Υ	12	14	N/A
Smeared	χ_{b1}	0	N/A	241
Smeared	χ_{b1}	3	119	0.3*
Smeared	χ_{b1}	5	27	0.2
Smeared	χ_{b1}	8	6	N/A
Smeared	χ_{b1}	10	3	N/A
Smeared	χ_{b1}	12	1	N/A

Table 4.1: Quality of fits to the $T = 95$ MeV ($N_\tau = 64$) correlator using both the three- and five-parameter ansatze given by equations (4.21) and (4.22) respectively. All fits use the end time $\tau_2/a_\tau = 63$. The algorithm failed to fit for the combinations labelled N/A and the causes for these are discussed in the body of Section 4.3.3. Note that χ^2_ν is the χ^2 per degree of freedom and that only cells denoted with an asterisk were used in the final analysis.

χ^2_ν is a function of the statistical uncertainties. In calculations of meson correlators, larger errors would prohibit access to excited state contributions; therefore, smaller statistical errors are beneficial. This, however, requires a suitable ansatz to capture these excited states, and, given that it is reasonable to expect that higher excited states could dissociate earlier than lower energy states, the number of excited states may vary across the temperature ranges explored in this work. It is for this reason that we expect even the five-parameter ansatz not to fully represent the spectrum above the ground state. This manifests in high values of χ^2_ν. Evidence that it is, in fact, excited state contributions that are the cause of the high χ^2_ν comes from two sources: firstly, the χ^2_ν for the five-parameter fits to the smeared data, where the excited state contributions are smaller by construction, are around 1, a strong indication that the ansatz captures the ground state behaviour well; and secondly, the larger one chooses the time window to start the better the fit to local correlators, evincing that the size of the excited state contributions are the cause of the high χ^2_ν. As mentioned in Section 4.3.3 this can only be done up to around $\tau = 8a_\tau$ as beyond that there is not enough excited state signal for a stable fit to an ansatz that explicitly contains one excited state.

A more complex ansatz could be proposed to minimise the χ^2_ν, perhaps one with a larger number of excited states, but this would come at a cost of a more difficult optimisation procedure and would be difficult to fit to all temperatures: it can already be seen from Table 4.1 that including just one excited state limited the time windows over which the fits converged.

It is for these reasons that we consider the five-parameter to strike the balance between excited state representation and flexibility, and why we still put weight on the ground state parameters recovered from the fits to local correlators in spite of the χ^2_ν.

To conclude, the local correlators will be analysed from $\tau_1/a_\tau = 8$ onwards, and the smeared correlators from $\tau_2/a_\tau = 3$ onwards.

4.4.2 End time, τ_2

The value of τ_2 is much more dependent on temperature, unsurprising given that the hottest simulation, $N_\tau = 16$, only contains an eighth of the data present in the coldest, $N_\tau = 128$. In Section 4.6.2 I will report the fitted values multiple times for each temperature. The maximum value of τ_2 possible for a given N_τ provides the most data for the fit, however, the colder lattices are also analysed with τ_2 corresponding to a hotter lattice's maximum τ_2 such that they can be compared at the same time window. Thus, there is no general optimal time range for all temperatures and the τ_2 value will be stated alongside the result for that analysis.

4.5 Optimal ansatz

All of the fits from the previous section were for the five-parameter ansatz from equation (4.22). However, our justification for this ansatz allowed for the two other ansatze, equations (4.20) and (4.21), that we named the two- and three-parameter ansatze respectively. In this section, the viability of each ansatz will be assessed to determine which functional form is most appropriate to extract fit parameters.

In Section 4.2.2 we introduced the effective mass, equation (4.7). It is easy to see that if the correlation function were given by the two-parameter ansatz of equation (4.20) then the effective mass would simply be M for all times. Figures 4.5 and 4.6 show that this is certainly not the case, for the local or smeared correlators respectively. The only correlator and time range that this ansatz would be appropriate would be the local Υ correlator at $T = 47$ MeV beyond $\tau \sim 60a_\tau$ because of the plateau of the effective mass; this is an important exception as this is what was used to calibrate the renormalisation of the masses extracted in NRQCD. In general, however, the two-parameter ansatz is not sufficient and we will turn to consider the other ansatze.

As a technical aside, the cause for five-parameter fits not converging at $\tau_1 \geq 10a_\tau$ was related to there not being enough signal from excited states. Given that the three-parameter ansatz does not attempt to fit excited states this is not a concern. Thus, the range of τ_1 that results in a converged fit is larger than it is for the five-parameter ansatz. However, the maximum value of τ_1 is still limited by the total range of the hottest lattice (where $N_\tau = 16$).

Comparing the quality of fits for the three-parameter fit to the quality of the five-parameter fits (Table 4.1) leads to a simple conclusion: the five-parameter fits are more suitable. This table reports the fits of both ansatze to the $T = 95$ MeV lattice with τ_2 fixed to $63a_\tau$, the latest time on this lattice. When there are large excited state contributions, i.e. when τ_1 is small, the three-parameter ansatz is simply not flexible enough to fit these data and thus the fits fail to converge. Even at larger τ_1 there must remain some features that cannot be captured by a single state, perhaps lattice artefacts if not excited states, this is evidenced by the large χ^2_ν for the local correlator fits. Therefore, only the five-parameter ansatz will be used going forward.

4.6 Results

I will perform fits to the local and smeared correlators, where each has its own benefit. The local fits can be performed at all temperatures and allow for the widest perspective to observe thermal modifications. The fitted smeared corre-

lators recreate the data much better than is the case for local fits, evidenced by Table 4.1. This means that there are likely fewer artefacts or features going unrepresented by the five-parameter ansatz when fit to the smeared correlators.

As a result of the preceding sections, the analyses will use the five-parameter ansatz given by equation (4.22), and $\tau_1 = 8a_\tau$ ($\tau_1 = 3a_\tau$) for the local (smeared) correlators. Note that this work will only focus on the ground state parameters.

A general statement that can be made when it comes to the results of these fits is that, when given two estimates of the same observable (mass or width), the lower is more likely closer to the true value. As we saw with the effective mass at early times, excited states interfere with the mass by increasing its value the more they are present. A similar effect occurs with the width: the peaks widen to account for the weight added to the high-energy part of the spectrum by excited states.

What will also be noticeable in the figures in this section is that there are temperatures that cannot be fit in a stable manner. This could be evidence of lattice discretisation artefacts, more excited states, or excited states with a finite width (all unaccounted for in this work). I will refrain from making such prescriptions and simply note that fits could not be made to all temperatures.

4.6.1 NRQCD mass renormalisation

The masses that are to be reported in this section were subjected to the conversion from equation (4.8). This contains both: converting from the units a_τ to GeV and adding the renormalisation inherent to NRQCD due to the integrating out of the overall mass scale. The former will simply be stated from [51], yet the latter will be discussed more at length as it relates intimately will the reported values of this section. For this generation of FASTSUM ensembles, there is no published report of the calculation of this additive shift, the analogous calculation for generation-2 was reported in [72]. The way in this the shift is calculated is as follows: the ansatz from equation (4.20) (corresponding to the spectral function being a δ-function) was fit to the local Υ correlator at the coldest temperature, $T = 47$ MeV, to extract an estimate of the 'zero temperature' $\Upsilon(1S)$ mass, $M_{\text{lat}}(\Upsilon)$. This mass is then compared with the experimental value, $M_{\text{expt}}(\Upsilon)$, from the Particle Data Group (PDG) booklet [47], the difference between the two estimations is thus the definition of the additive renormalisation [91],

$$E_0 = M_{\text{expt}}(\Upsilon) - M_{\text{lat}}(\Upsilon) = 7.463 \text{ GeV}. \tag{4.28}$$

This has interesting implications for the results of this work. Firstly, the experimental Υ mass is used as an input to this work, and therefore, if both the single exponential fit that set this scale and the fits from this work were

equivalent, then our estimates of the Υ mass would equal the PDG value by construction. We will see that this is not the case and we will address this in Section 4.7. Secondly, the reported mass of χ_{b1} is now subject to any systematic uncertainties in the determination of the additive shift, correlating the results with those of the Υ.

4.6.2 Fixed time window analysis

All of the figures in this subsection have the same format. Fit parameters are extracted multiple times for the same lattice with the difference being the end of the time window, τ_2. Fits at different temperatures but with the same time window, and thus the same systematic errors, are shown in the same colour with the same symbol: comparisons made between data of the same colour (and symbol) are optimal for discerning temperature dependence. What this does not allow for is a comparison between data from different colours, they will contain systematic differences that are not accounted for. Data at the same temperature but in different time ranges are not independent, so multiple time windows showing a certain behaviour are not separate validations of that behaviour. However, the systematic changes are different across different time ranges, so one would hope that if there is a certain behaviour in one time range then this should be echoed in the others, but this is not guaranteed. Even a cursory look at the figures in this subsection (Figures 4.9, 4.10, 4.11, and 4.12) will show that the systematic effects of the time window are often larger than the changes with temperature. Analysis will focus on two regimes: $T < T_{\text{pc}}$ and $T > T_{\text{pc}}$, where T_{pc} is the pseudo-critical temperature of 167 MeV.

We begin with the temperature dependence of the ground state mass, shown in Figures 4.9 and 4.10 where the top pane of both figures is the Υ and the bottom is for the χ_{b1}. Below T_{pc} there is no statistically significant change in the mass with temperature for Υ or χ_{b1}, local or smeared. This is evidenced by following any set of same-coloured points in Figures 4.9 and 4.10. Above T_{pc} such a sweeping statement cannot be made.

In Figure 4.9 (top) the fits to the local correlator for Υ do show a very small, albeit statistically significant, increase in mass from 235 MeV to 304 MeV when $\tau_2 = 19a_\tau$ and again between 304 MeV and 380 MeV when $\tau_2 = 15a_\tau$. However, given the lack of significant change between 235 MeV to 304 MeV when $\tau_2 = 15a_\tau$, the first of these two increases appears less consequential: it is not a general trend between temperature increases, it only occurs for one of two time windows. This leaves only a single point to suggest temperature dependence of the mass. With that in mind, consider Figure 4.10 (top), the smeared correlator of the same state. Fits could not be performed at the hottest temperatures, therefore no extra data could support the very high-temperature behaviour. No temperature dependence

is present for the data that exist. Therefore, the only evidence for a temperature dependent Υ mass is the hottest datum in Figure 4.9 (top).

The behaviour of the χ_{b1} mass above $T_{\rm pc}$ is very similar. The large increase in the magnitude of statistical errors makes significance harder to achieve, however, there are still two pairs of temperatures where the change in mass is larger than the statistical errors: 235 MeV to 304 MeV when $\tau_2 = 19a_\tau$ and 304 MeV to 380 MeV when $\tau_2 = 15a_\tau$. These are the same points that were significant for Υ. Once again the first temperature change is not present in the other time window, leaving just a single datum to suggest temperature dependence. The smeared correlators failed to lead to a stable fit for the hottest lattices, and for the temperatures that were fit, there is no temperature dependence (Figure 4.10 (bottom)).

I will now consider the fits to the ground state width, shown in Figures 4.11 and 4.12. The width of the Υ from the local correlator (Figure 4.11 (top)) exhibits a systematic increase with temperature beginning around $T_{\rm pc}$. Data from all values of τ_2 that allow for analyses hotter than $T_{\rm pc}$ show systematic and significant increases of width with temperature. There are similarities in the data from smeared correlators: a general trend of increasing width with temperature, shown in Figure 4.11 (top). There are differences in how this manifests: firstly the increase for the larger τ_2s begins immediately and not around $T_{\rm pc}$, there are larger relative fluctuations of the width with temperature, and the relative increase for the hottest lattices is much more pronounced than in the data from local correlators.

The width of χ_{b1} also shows a systematic increase with the temperature beginning around $T_{\rm pc}$ for the local correlator, Figure 4.11 (bottom). This effect is larger, relative to the values of width reported than in fits to Υ local correlators. The fits to smeared data show more structure, Figure 4.12 (bottom). Between 95 and 152 MeV some time windows report a significant dip in width, yet others steadily increase. It is hard to tell the significance of this behaviour when there is such disagreement across time range. However, I must again stress that data in different colours have different systematic effects that are not accounted for when making naive comparisons. All time windows for which there are data above $T_{\rm pc}$ agree that there is a large increase in the width, well beyond the level of statistical errors.

From the analyses in this section, the temperature dependencies most supported by data are: no significant change to the ground state mass of Υ or χ_{b1}, yet a significant increase in the ground state width for both states, starting around $T_{\rm pc}$ and being more significant in the χ_{b1}.

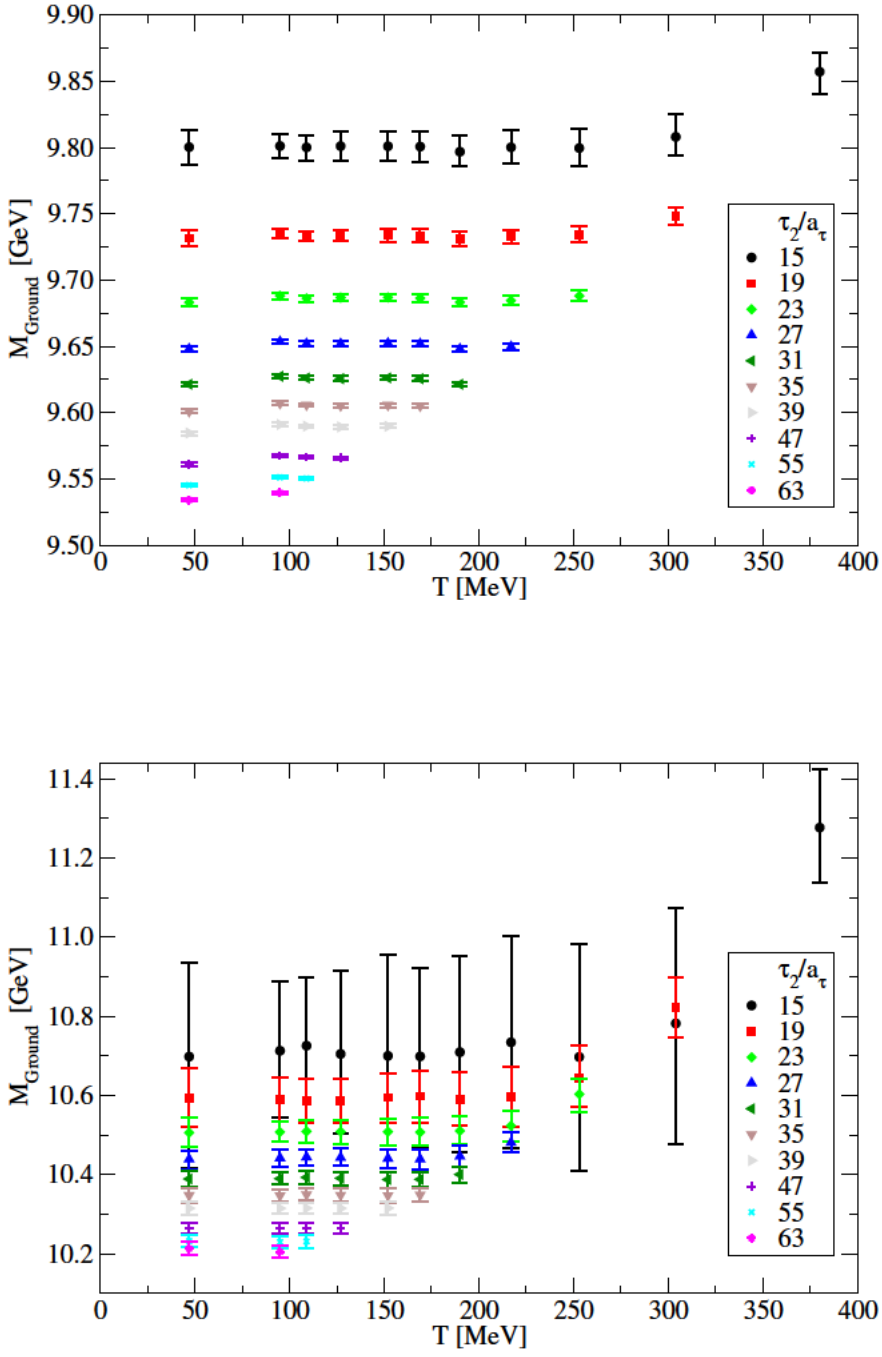

Figure 4.9: Ground state mass fit to Υ (top) and χ_{b1} (bottom). Both use local correlators. Lines of the same colour were fit to the same time window $\tau/a_\tau \in [8, \tau_2]$ and therefore have the same systematic errors. Error bars shown are purely statistical.

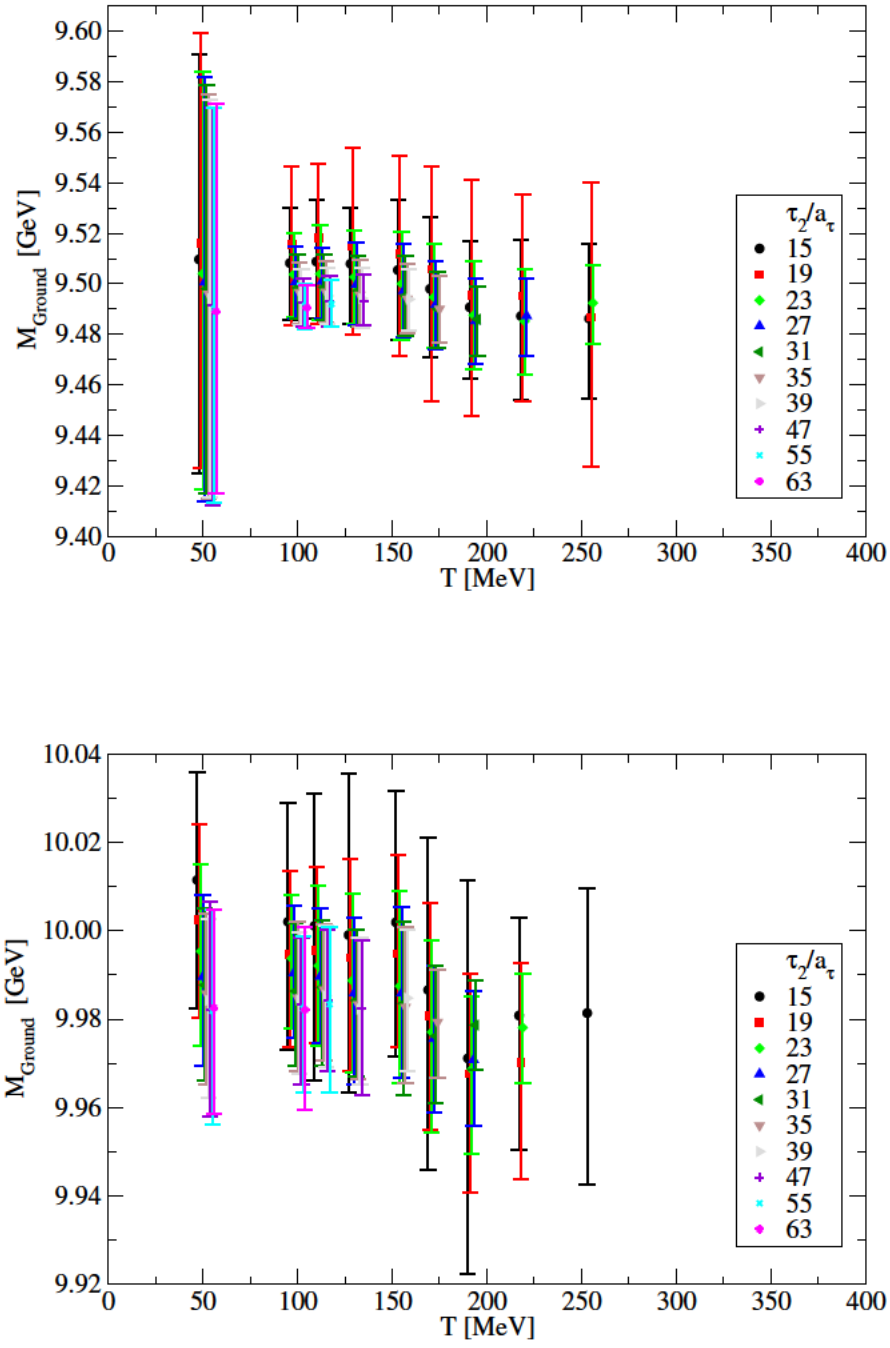

Figure 4.10: Ground state mass fit to Υ (top) and χ_{b1} (bottom). Both use smeared correlators. Lines of the same colour were fit to the same time window $\tau/a_\tau \in [8, \tau_2]$ and therefore have the same systematic errors. Error bars shown are purely statistical and the data have been shifted horizontally for clarity.

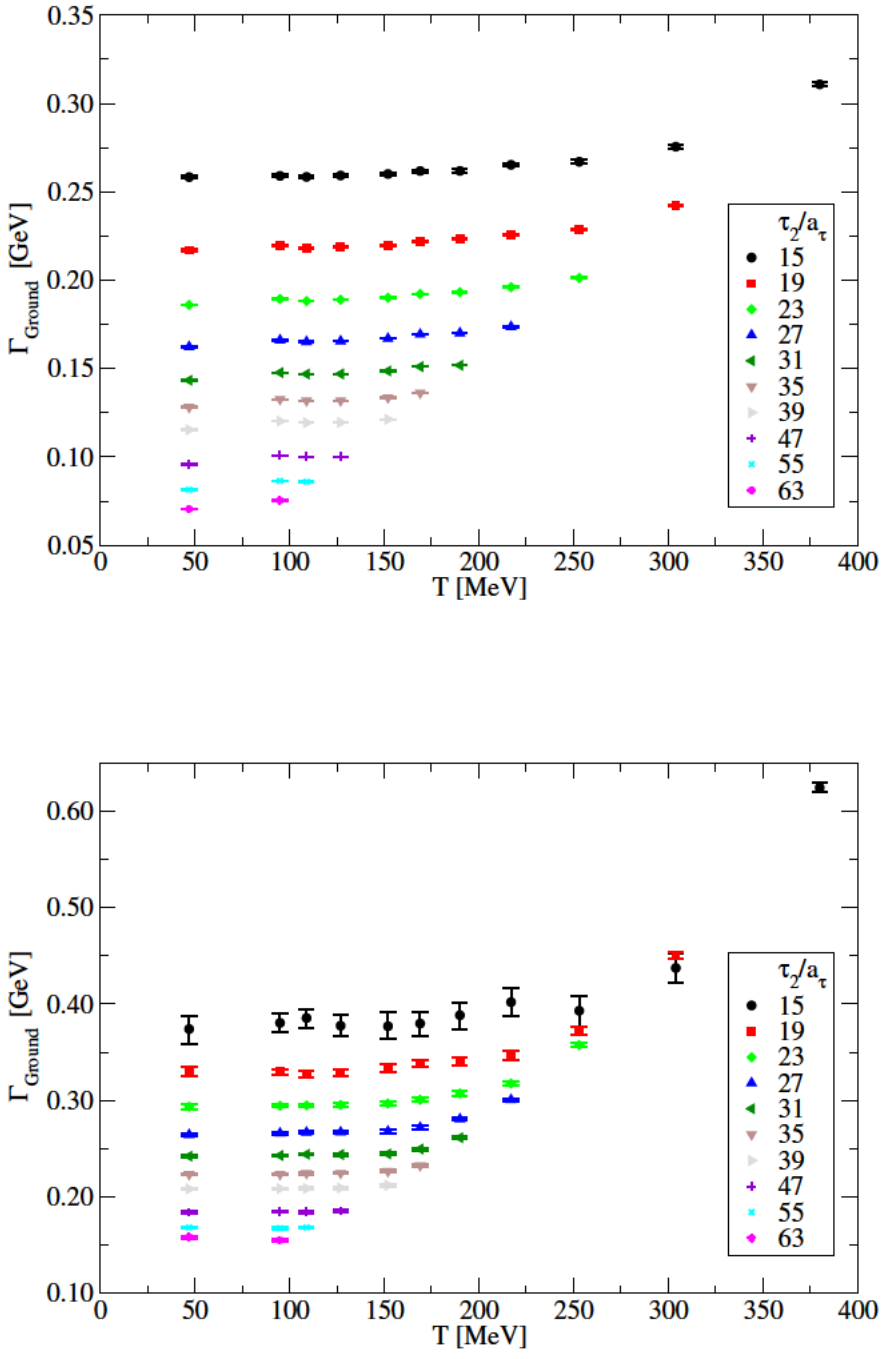

Figure 4.11: Ground state width of the Υ (top) and χ_{b1} (bottom). Both use local correlators. Symbols of the same colour were fit to the same time window $\tau/a_\tau \in [8, \tau_2]$ and therefore have the same systematic errors. Error bars shown are purely statistical.

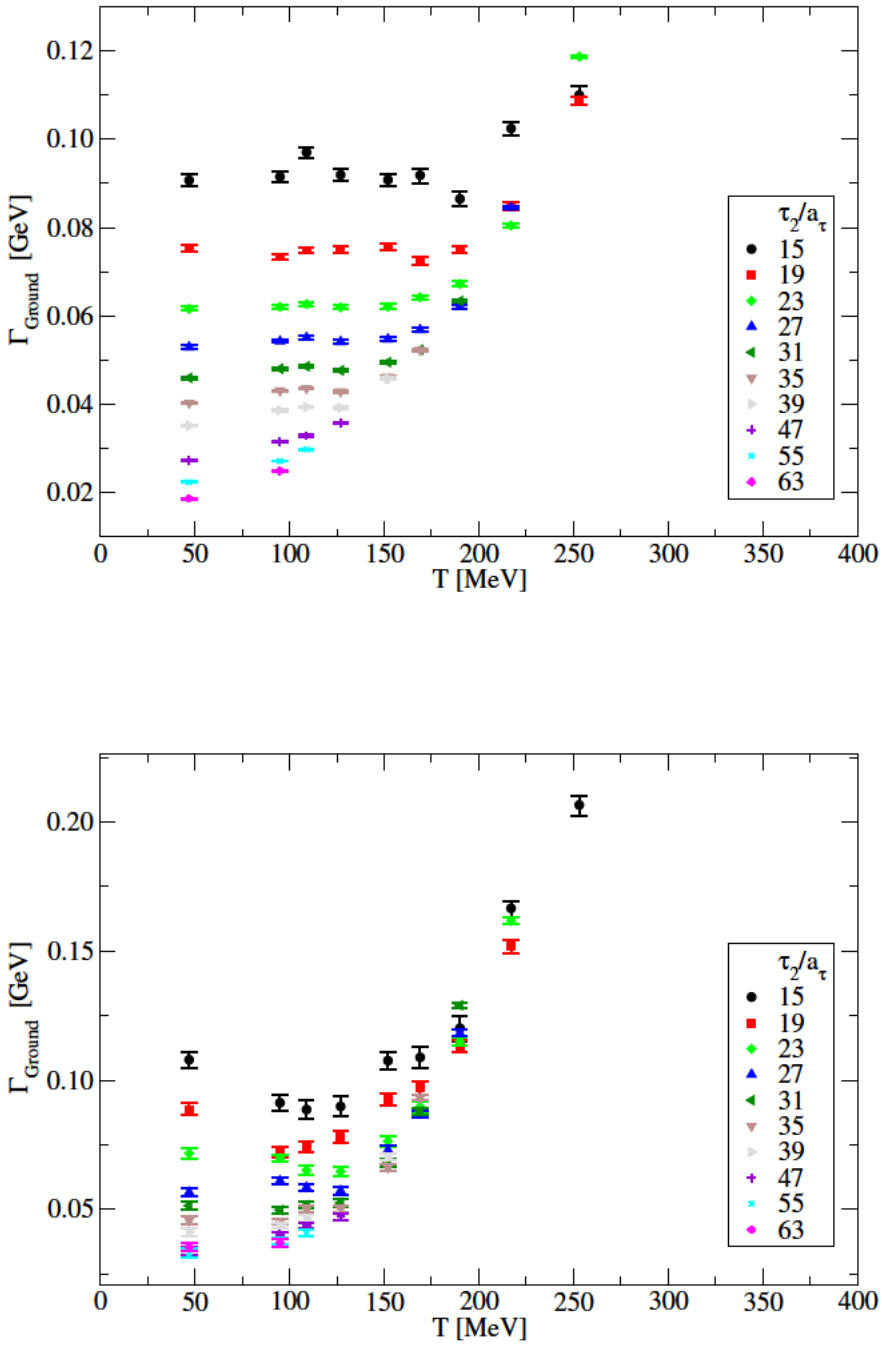

Figure 4.12: As in Figure 4.11 but for smeared correlators.

4.6.3 Time window independent analysis

There are clearly time window effects in values of mass and width reported in the previous subsection. I will now try and give a value of mass and width for each temperature that has the time window effects extrapolated out and integrated into a systematic and statistical error. This will be an extension of the work done in [1, 2].

The ground state parameters would be most easily extracted in the regime where only the ground state contributes to the correlator. This regime is the infinite time limit, $\tau_2 \to \infty$. Therefore, we would like to extrapolate the ground state parameters to the $\tau_2 \to \infty$ limit. Given that we have values of mass and width at different τ_2, we can plot these values against $1/\tau_2$ and, assuming a linear dependence on τ_2, extrapolate the value at $1/\tau_2 = 0$ using linear regression. Two examples of this linear extrapolation are shown in Figures 4.13 and 4.14, one for mass and the other for width. Both of these figures are for the Υ local correlators. The linear relationship between the ground state mass and $1/\tau_2$ is incredibly well respected and the change in the extrapolated value is small across the different extrapolations (when performed over different ranges of data). These offer promising evidence that the extrapolation is valid. A linear relationship between the ground state width and $1/\tau_2$, however, is not very well respected. A more complex relationship than linear could be proposed, *a posteriori*, but as there is no clear justification for any specific relationship, no fine-tuning was performed. Any poor linear fits will supply a larger error which more accurately represents the uncertainty of this extrapolation.

On this note, two sources of error can be estimated from these extrapolations. Firstly, there is a statistical error due to the errors in the estimates of mass or width at each $1/\tau_2$. These can be attributed to the fluctuations within each ensemble of lattice configurations. Secondly, there is a systematic uncertainty due to the choice of data to include in the extrapolations. To quantify this second source of error the extrapolation is done for multiple sets of temperatures: all temperatures, then all but one (ignoring the hottest), all but two (ignoring the two hottest), *etc.* until only two temperatures remain. The value of the error is taken to be half of the spread of the extrapolated value from each set. The two errors, the one inherent to the linear regression, and the one due to the range of temperatures, were added in quadrature to create the overall error estimate. The central values that will be reported use the extrapolation that includes all temperatures. As with the plots in Section 4.6.2, the fitting routine converged for more temperatures when applied to the local correlators than to the smeared, so there will be more data reported for local than smeared.

Figures 4.15 and 4.16 show the temperature dependence of the Υ (top panes) and χ_{b1} (bottom panes) for the local and smeared correlators respectively. There

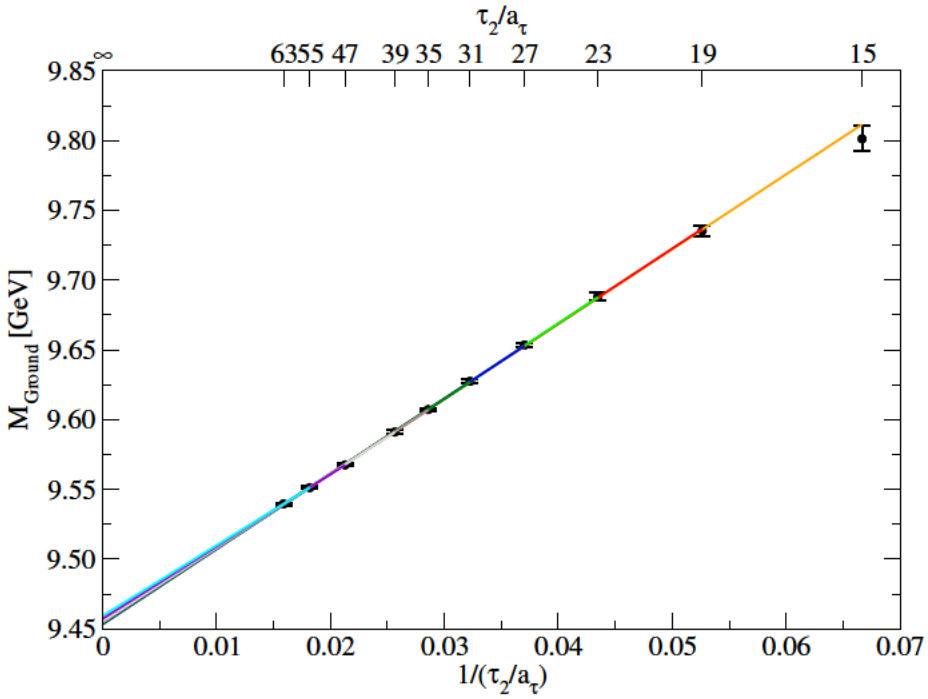

Figure 4.13: Extrapolations of the Υ mass fit to the local correlators at $T = 95$ MeV. Each marker is the fit to the time window $\tau/a_\tau \in [8, \tau_2]$ with statistical errors from fits to a bootstrapped ensemble of correlators. Each line is the extrapolation over a different range of τ_2. The two error contributions extracted from this figure arise from the statistical error in fitting the orange line (spanning the largest range of $1/\tau_2$), and half of the spread of the y-intercepts.

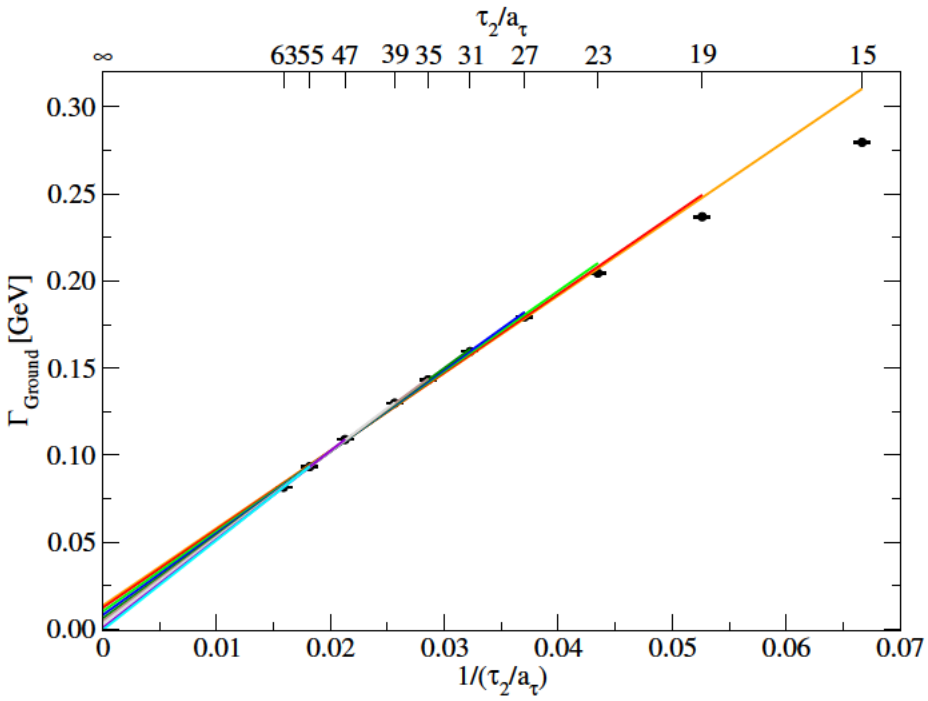

Figure 4.14: As in Figure 4.13 but for the Υ width.

is no significant temperature dependence present in the extrapolated ground state mass for Υ and χ_{b1} fit to the local correlators (Figure 4.15), this is similar to the time window dependent plots, for example, Figure 4.9. This is even more clear for the ground state masses from the smeared correlators, see Figure 4.16. Therefore, in all analyses of the ground state mass, there is no clear evidence of temperature dependence.

The temperature dependence of the width has more structure, this is presented for the local and smeared correlators in Figure 4.17 and 4.18 respectively. The ground state width of the Υ increases monotonically with temperature. For the local correlator, the changes between neighbouring temperatures are immediately significant, shown in Figure 4.17. Likewise, from Figure 4.18 one can see that the same is true for the data from smeared correlators: the increase between neighbouring points is immediately beyond the level of errors. The ground state width of the χ_{b1} also increases with temperature, albeit only above approximately T_{pc}. This change is smooth in the data from local correlators yet looks sharp in the smeared case. With that being said, the magnitude of the increase is much larger than it is for the Υ. These are similar findings to the time window dependent plots of Section 4.6.2 with one exception, the temperature at which the Υ width increases. In this time window independent analysis, the width appears to increase for $T \geq 47$ MeV, yet for local correlator in Section 4.6.2 it was not until $T = 152$ MeV and later still for the smeared correlator.

4.7 Conclusion

Up to this point, there have been two kinds of analysis performed (time window dependent and independent) on two kinds of correlators (local and smeared) for two states (Υ and χ_{b1}) to observe two quantities (mass and width). From these 16 combinations there are two themes that are consistent. For both states, the ground state mass does not appear to change with temperature, yet the ground state width increases with temperature. The temperature at which this width increase begins is unclear for Υ, either as soon as $T \geq 47$ MeV or at $T \sim T_{\mathrm{pc}}$. For the χ_{b1} it is clear that the increase begins around T_{pc} and is larger than it is for the Υ.

The correlators for both S- and P-wave, local and smeared, show thermal modifications from as early as $0.76T_{\mathrm{pc}}$, being most significant above and around T_{pc}. It was shown that these were not caused by temperature variations in the ground state mass, yet the extent to which these modifications can be attributed to an increasing ground state width is unclear: above T_{pc} the ground state width increases for both Υ and χ_{b1}, however from $(0.76-1)T_{\mathrm{pc}}$ the width only increases for Υ, with it appearing fixed for χ_{b1}. Only the ground state parameters were

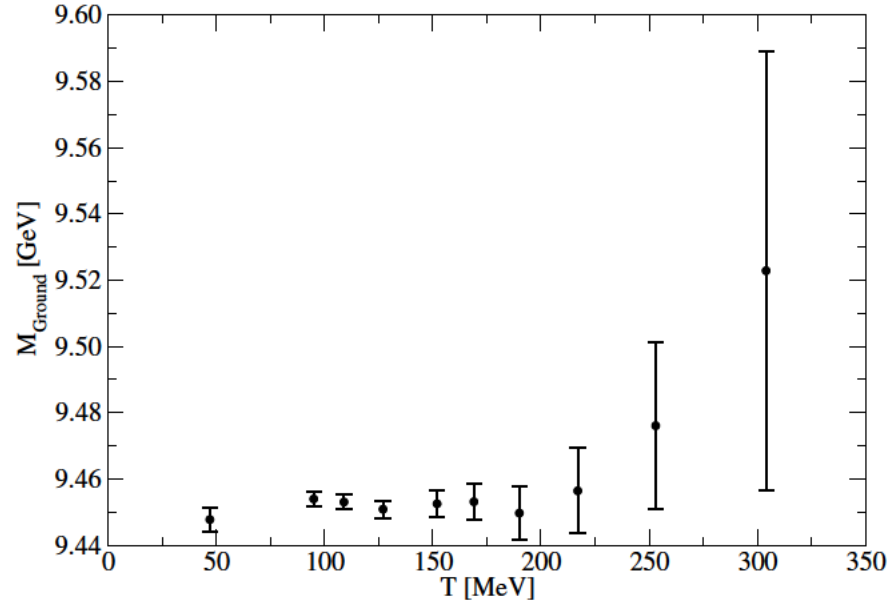

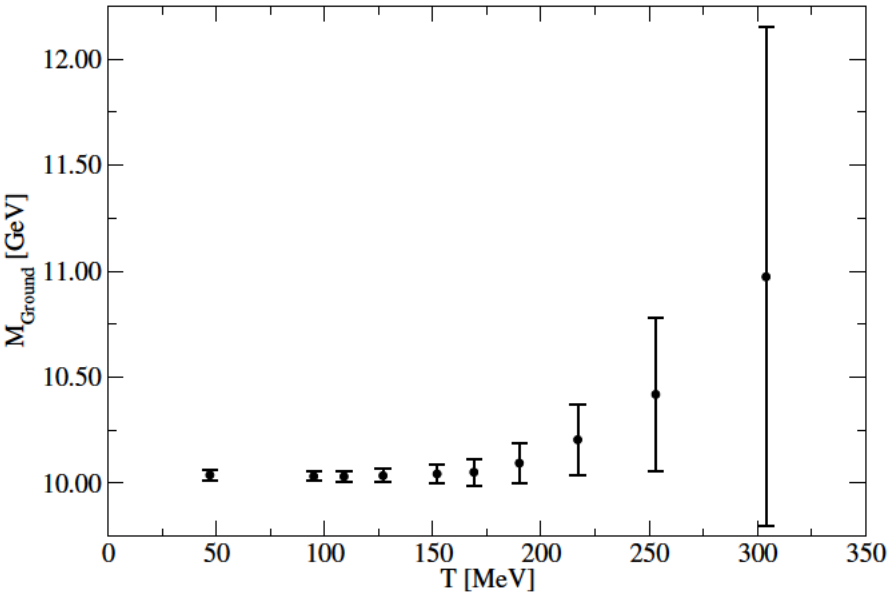

Figure 4.15: Extrapolated mass from local correlators of Υ (top) and χ_{b1} (bottom). The error is a combination of two sources, explained in Section 4.6.3 incorporating uncertainty from statistical and systematic variations.

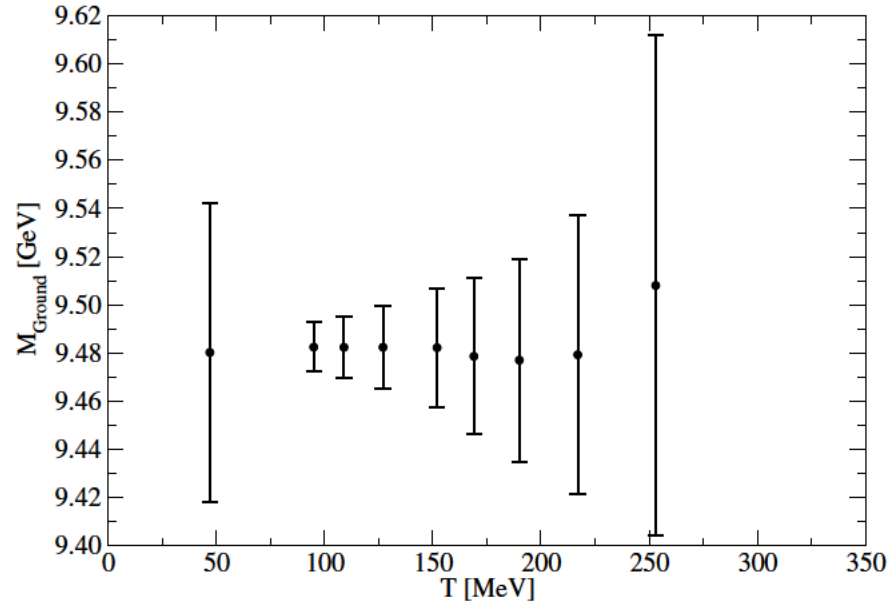

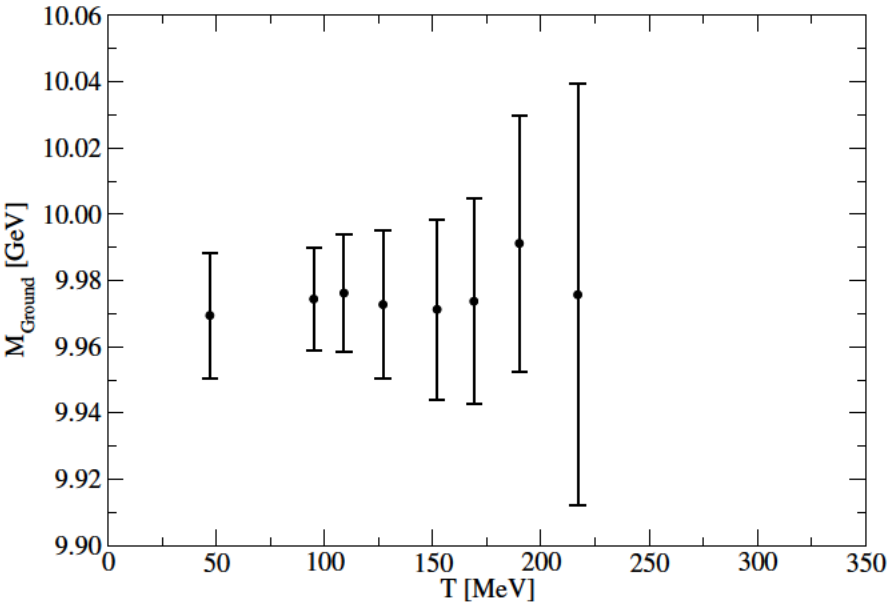

Figure 4.16: As in Figure 4.15 but from smeared correlators.

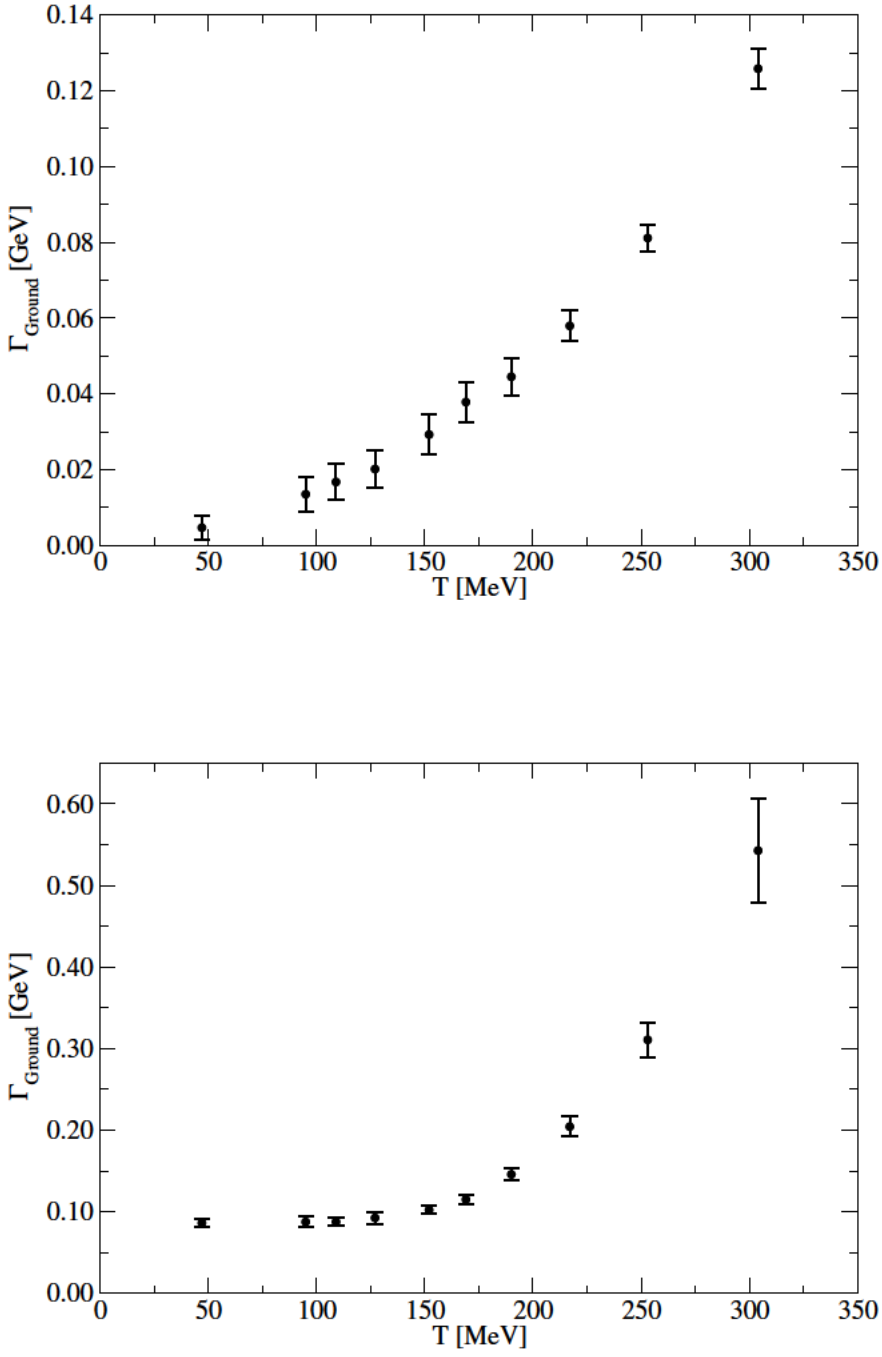

Figure 4.17: Extrapolated width from local correlators of Υ (top) and χ_{b1} (bottom). The error is a combination of two sources, explained in Section 4.6.3 incorporating uncertainty from statistical and systematic variations.

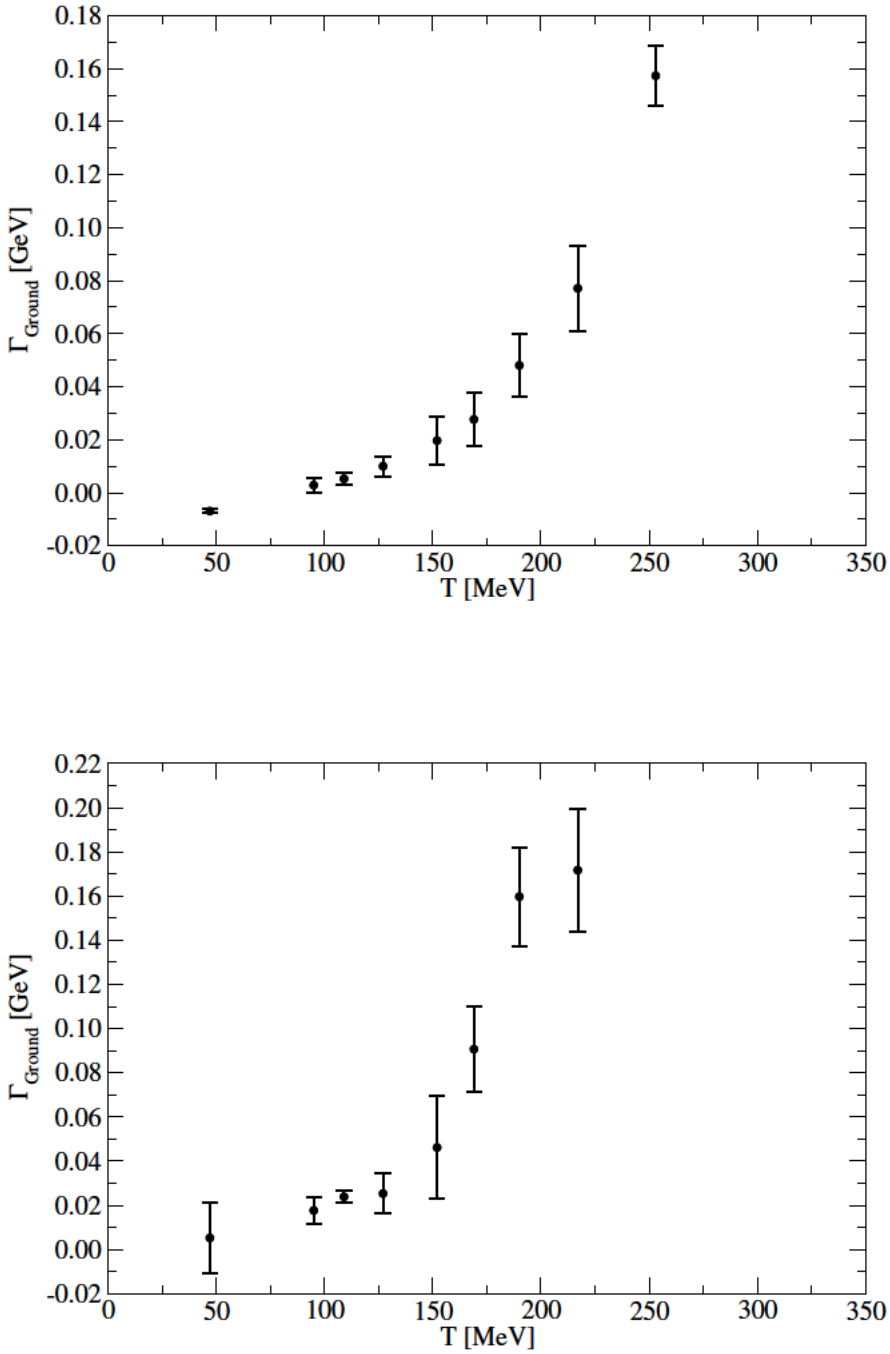

Figure 4.18: As in Figure 4.17 but from smeared correlators.

reliably extracted and thus any further change cannot be confidently attributed to excited states.

These results are in qualitative agreement with a similar analysis of NRQCD bottomonium spectra [83] who find no change in the ground state mass for either the Υ or χ_{b1} but an increase in the width for both. As was the case for the work of this chapter, the increases in width and the statistical errors are larger for the P-wave, and the temperature at which this width significantly increases is unclear. However, a study on the S-wave bottomonium spectrum using NRQCD quarks on the FASTSUM generation-2 ensembles reports that the mass increases with temperature, as well as the width [45]. This was extended to P-wave states using the same configurations in [72], however, only spectra were reported and thus one cannot draw numerical comparisons. As such, it is difficult to assess the significance of the changes in mass with regard to statistical errors. Qualitatively, [72] reports an increase in width with temperature for both states. This chapter is in agreement with both papers from the FASTSUM collaboration when it comes to the increase in the χ_{b1} width being much larger than it is for the Υ, supporting their claims that the Υ would survive at higher temperatures than the χ_{b1}.

The reported masses at the lowest temperature do not agree with the values stated by the PDG; the Υ ground state mass should have done so by construction. This can be attributed to several factors. Firstly, the single exponential fit that was used to determine the NRQCD additive normalisation introduces systematic effects that were not accounted for in that estimation. For example, in Section 4.6.2 we showed how the time window used had a significant effect on the fitted value, an effect that we try to address in Section 4.6.3 by extrapolating out the dependence on the time window. No such treatment was done for the single exponential fits that set the renormalisation and thus there are unaccounted for systematic effects that impact both the S- and P-wave masses. Secondly, these gauge configurations are calculated with a lower-than-physical pion mass, with a non-zero lattice spacing, finite volume, and a plethora of systematic artefacts that cannot be easily ignored. Finally, there are effects from non-QCD sources, such as QED, that can affect hadron masses. All of these factors are kept equal for studies of temperature dependence, but for comparing these results to those from collider experiments, they cannot be ignored.

In closing, then, this work finds no temperature dependence of the $\Upsilon(1S)$ or $\chi_{b1}(1P)$ masses, but clear, monotonic, and significant increases in their width with temperature. The extent to which these states survive in the QGP cannot be established from this work alone, but this does support the claim of the FASTSUM collaboration that the χ_{b1} melts before the Υ.

Chapter 5

On-axis interquark potential

The potential between the quark and antiquark in a meson can offer a rich window into the phenomenology of quark interactions. In Chapter 4 we calculated the spectral function in order to glean some of this information. In this and the following chapter, we will calculate the interquark potential of the bottomonium system that can complement the results from spectral reconstruction.

It has been established that charmonium bound states at zero temperature can be well described using the Schrödinger equation, modelling the interactions between quark and anti-quark with a phenomenological potential [29–31], with the latter work extending this to bottomonium. The HAL QCD method builds upon this by formulating the Schrödinger equation from lattice observables to calculate the potential. The method was developed by the HAL QCD collaboration to calculate the internucleon potential [92–95] but has also been extended to the interquark potential [96–102].

In this chapter, I will use the HAL QCD method to calculate the interquark potential of the bottomonium system and extend the treatment to non-zero temperature. This work builds upon [3], the first presentation of the central potential of bottomonium using NRQCD quarks from the HAL QCD method at non-zero temperature.

This analysis is performed on the FASTSUM generation-2 ensembles.

5.1 Related works

There are many lattice calculations of the static quark potential (introduced in Section 3.3) at a range of temperatures around the critical temperature. The results are consistent with the potential between two heavy quarks being captured by a 'Coulomb + linear' Cornell-like potential. Works from [103–108] report that the string tension (the slope of the linear part of the potential) decreases with increasing temperature: in particular, it is found that the real part of the complex-valued potential shows Debeye (colour) screening above T_{pc}. However, more recently, [109] cast doubt upon the appearance of colour screening, reporting that its existence with temperature is dependent on the method used to extract the static quark potential. Further developments were reported in preliminary

work from [110]. All of these works agree that there is a non-zero imaginary part of the potential that increases with temperature.

This introduces a significant difference between the HAL QCD method and the calculation of the static quark potential: the HAL QCD method only gives access to the real part of the potential. This can be traced back to the calculation of the point-split correlator that will be introduced in Section 5.2.1. This quantity calculated on a single configuration is complex, but the imaginary part averages to zero over the entire ensemble of configurations, giving no access to the imaginary part of the potential.

For this chapter, we will consider the leading order velocity expansion of the interquark potential for S-waves. This expansion expresses the central potential, $V_C(r)$, and spin-dependent potential, $V_S(r)$, in terms of the contributions from the pseudoscalar and vector potentials. Following the notation of Chapter 4 we will denote channels with the subscript λ. Thus, the potential expansion reads [111]

$$V_\lambda(r) = V_C(r) + \mathbf{S}_1 \cdot \mathbf{S}_2 V_S(r). \tag{5.1}$$

$\mathbf{S}_{1,2}$ are the quark spins, with $\mathbf{S}_1 \cdot \mathbf{S}_2 = -3/4, 1/4$ for the pseudoscalar and vector channels respectively.

Using the HAL QCD method, the central and spin-dependent potentials have been calculated at zero [97, 98, 100] and non-zero [101] temperature in the charmonium system. The zero temperature results are consistent with a Cornell form for the central potential and report the spin-dependent potential and having a repulsive core before plateauing to zero beyond the region of $0.2 - 0.5$fm. It should be mentioned, however, that in [98, 100] the spin-dependent potential at large distance is zero by construction. The Cornell form is also exhibited at non-zero temperature, where [101] finds that, with increasing temperature, the central potential exhibits systematic flattening at large distance.

One study on the Nambu-Bethe-Salpete (NBS) wavefunctions[1] (which we will introduce in Section 5.2) of bottomonium using NRQCD quarks presents the central potential at zero temperature but stops short of presenting the non-zero temperature form [102]. The authors claim that care must be taken, particularly to the τ dependence of the NBS wavefunctions, to extend the HAL QCD method to non-zero temperature. The τ dependence will be explored in Section 5.4 and a new method will be introduced in Chapter 6 to explicitly test the validity of the HAL QCD approach at non-zero temperature. There are also works that compute hadronic wavefunctions from lattice QCD data but do not extend their analysis to the interquark potential, see [112] for example.

In its original domain of nuclear physics, the HAL QCD method appears to be at tension with the alternative approach in that setting, the Lüscher method,

[1] Often called Bethe-Salpeter wavefunctions

when it comes to the so-called *two nucleon controversy* [113]. Chiefly, two questions are asked about the HAL QCD method: one pertains to the range of validity of the potential expansion in equation (5.1) and the other to the separation of the excited states above threshold from those below. It certainly remains unclear if the cause of the tension lies solely at the feet of the HAL QCD method, and the HAL QCD collaboration has addressed several of the concerns in [95], but we are more concerned with establishing if these concerns are relevant for the simpler system of NRQCD mesons.

Addressing the order of the potential expansion, insofar as we are assuming that the dominant contributions to the vector and pseudoscalar channels are S-wave states (we will explicitly check for spherical symmetry in Section 6.3 to assess this) then the extra terms included by higher order expansions, the spin-orbit or tensor contributions for example, are zero. Therefore, the current order of the potential expansion is sufficient for this work. As for the contributions from states above threshold, this is much less challenging for heavy quarkonium, especially bottomonium, as, taking the J/ψ states for example, the $1S$, $2S$, and $3S$ states are all below threshold and thus only the highly excited states would be above [47]. Given that these highly excited states ($4S$ and above) decay exponentially quicker than the lower states, only the very early times would ever contain enough contribution from above threshold for this to raise questions. And as we will see in Tables 5.1 and 6.1, the very early times are not included in the analysis. Therefore, the concerns raised against the HAL QCD approach pertaining to the two nucleon controversy are much less, if at all, relevant here.

5.2 The HAL QCD method

The central quantity of this method is the NBS wavefunction and its relation to the point-split meson correlator. There are two ways in which this correlator is introduced into the Schrödinger equation resulting in the time-dependent and time-independent HAL QCD methods. Section 5.2.1 will detail the calculation of the point-split correlator (which is common to both methods) and then Sections 5.2.2 and 5.2.3 outline the time-dependent and time-independent methods respectively.

5.2.1 Point-split correlation function

The point-split correlation function is defined as

$$C_\lambda(\mathbf{r},\tau) = \sum_{\mathbf{x}} \langle O_\lambda(\mathbf{x},\tau;\mathbf{r}) O_\lambda^\dagger(0;\mathbf{0})\rangle, \tag{5.2}$$

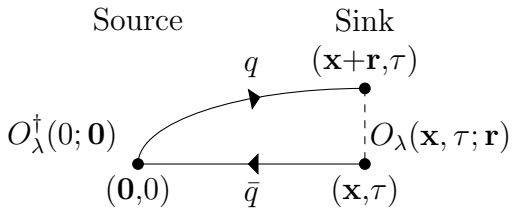

Figure 5.1: A representation of the point-split correlation function, as defined in equation (5.2).

where the non-local meson interpolators are defined by

$$O_\lambda(x;\mathbf{r}) = \bar{q}(x)\lambda U(x, x+\mathbf{r})q(x+\mathbf{r}). \tag{5.3}$$

For the two channels considered in the remaining chapters, the pseudoscalar and vector channels, $\lambda = \mathbb{I}$ and $\lambda = \boldsymbol{\sigma}_j$ respectively. This correlator reduces to equation (4.3) when $\mathbf{r} = 0$. When $\mathbf{r} \neq 0$ however, the interpolating operator at the sink is calculated on two lattice sites. To maintain gauge invariance the link operator, $U(x, x+\mathbf{r})$, is introduced. Going forward we will consider gauge fixed fields, fixed to the Coulomb gauge, and thus the link operator is set to unity. A pictorial representation of the point-split correlator is shown in Figure 5.1.

As equation (5.2) is a generalisation of equation (4.3), the calculation of this correlation function is significantly more computationally expensive: it contains the sum over all lattice sites $\mathbf{x}$ for every separation $\mathbf{r}$. This generation of lattice ensembles, generation-2, contains 24^3 sites per time-slice (see Table 3.1 for further details of the generation-2 ensembles). Therefore, the expectation of the two interpolators must be calculated $N_r \times 24^3 \times N_\tau$ times per configuration to get $C_\lambda(\mathbf{r}, \tau)$ for a single temperature (number of $\mathbf{r}$ values $\times$ number of $\mathbf{x}$ values $\times$ number of τ values respectively). Computational constraints meant that we chose to calculate only on-axis separated sinks, and thus $N_r = (3 \times 23) + 1$ (three axes each of length 24 but sharing the same $\mathbf{r} = \mathbf{0}$ point). Therefore, the whole calculation requires roughly a factor of 200 fewer expectation calculations than if we had chosen every possible $\mathbf{r}$ value. We will see in Section 6.1.1 that a momentum space representation exposes redundancies in the calculation which reduces the size of the computation, but for the remainder of this chapter we will work with the on-axis data calculated using equation (5.2). Figure 5.2 shows the dependence of these correlators on r and τ for each of the temperatures available. Due to the large range over which these correlators span, the data are plotted on a logarithmic scale but these correlators are not positive definite and thus there are some data that do not have a defined logarithm; non-positive data will still be used for further analysis, however.

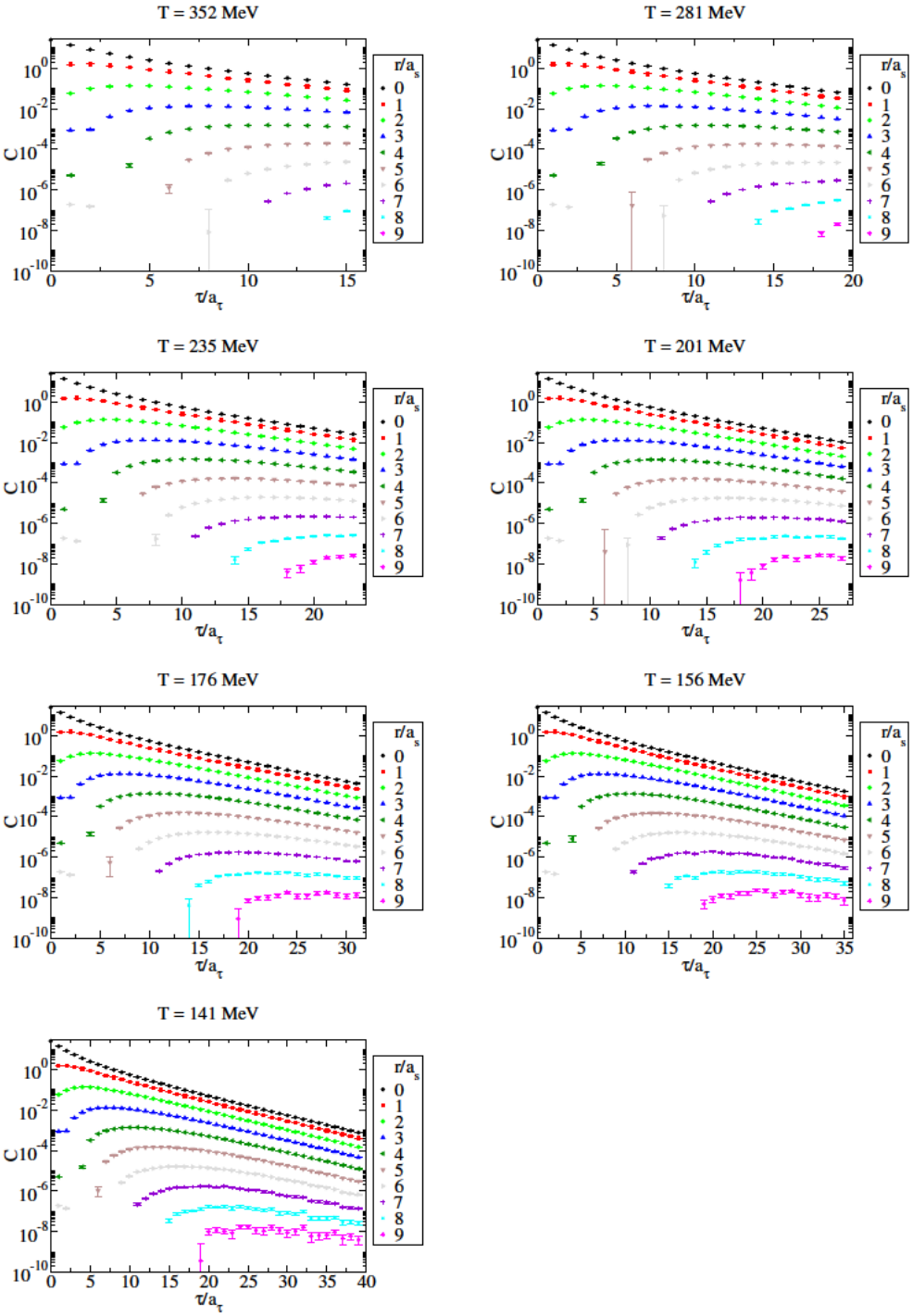

Figure 5.2: The point-split correlator defined in equation (5.2) for the vector channel. Each pane is a different temperature and within each pane, the different sink separations, denoted r/a_s, are given by a different colour. The data are best shown on a logarithmic scale, however, this correlator is not positive definite and thus there are negative entries that are not defined on this logarithmic scale, hence the points missing at early times and large r/a_s.

5.2.2 Time-dependent method

This method was first applied to the interquark potential in [100] and will be the method used, and later developed upon, in this thesis.

This point-split correlation function can be expressed in terms of eigenstates of the Hamiltonian,

$$C_\lambda(\mathbf{r},\tau) = \sum_j \Psi_j(\mathbf{r}) e^{-E_j\tau}, \tag{5.4}$$

where the energy of each eigenstate, j, is given by E_j. The indexing j is chosen such that $E_j < E_{j+1}\ \forall j$. The unnormalised wavefunction $\Psi_j(\mathbf{r})$ is related to the NBS wavefunction, $\psi_j(\mathbf{r})$, by

$$\Psi_j(\mathbf{r}) = \frac{\psi_j^*(\mathbf{0})\psi_j(\mathbf{r})}{2E_j}, \tag{5.5}$$

and is written in this form for convenience. Once this equivalence between our lattice observable (the point-split correlator) and the NBS wavefunction has been established, we can introduce the Schrödinger equation. We use the time-independent form with a reduced quark mass, μ,

$$\left(-\frac{\nabla^2}{2\mu} + V_\lambda(\mathbf{r})\right)\Psi_j(\mathbf{r}) = E_j\Psi_j(\mathbf{r}). \tag{5.6}$$

The value of μ was set to $\frac{1}{4}m_\Upsilon$. For a system of two bottom quarks interacting via a central potential, the reduced mass is half the mass of the bottom quark, and the Υ is comprised of two bottom quarks. Similar reasoning was applied in [96, 101]. Later, in Sections 6.4 and 6.5 we will discuss an improved method of determining μ. Combining this Schrödinger equation with equation (5.4) yields

$$\begin{aligned} -\frac{\partial C_\lambda(\mathbf{r},\tau)}{\partial\tau} = \sum_j E_j\Psi_j(\mathbf{r})e^{-E_j\tau} &= \sum_j \left(-\frac{\nabla^2}{2\mu} + V_\lambda(\mathbf{r})\right)\Psi_j(\mathbf{r})\, e^{-E_j\tau} \\ &= \left(-\frac{\nabla^2}{2\mu} + V_\lambda(\mathbf{r})\right) C_\lambda(\mathbf{r},\tau). \end{aligned} \tag{5.7}$$

From which we can express the interquark potential for a given channel as

$$V_\lambda(\mathbf{r}) = \frac{1}{C_\lambda(\mathbf{r},\tau)}\left(\frac{\nabla^2}{2\mu} - \frac{\partial}{\partial\tau}\right) C_\lambda(\mathbf{r},\tau). \tag{5.8}$$

It is convenient to define the central potential, V_C, which is built to not have any spin-dependent contributions. This is obtained from equation (5.1) via the spin-average

$$V_\mathrm{C} = \frac{1}{4}V_\mathrm{PS} + \frac{3}{4}V_\mathrm{V}. \tag{5.9}$$

Subscripts V and PS denote the vector and pseudoscalar channels respectively. We assume that the recovered potential is spherically symmetric (true in the continuum for purely S-wave states), and thus $V_{\mathrm{C}}(\mathbf{r}) = V_{\mathrm{C}}(r)$. There are, however, known spherical symmetry breaking effects due to finite lattice spacing and D-wave contributions to the vector channel that are not spherically symmetric. In Chapter 6 we will explicitly test this assumption of spherical symmetry.

5.2.3 Time-independent method

The time-independent method was the precursor to the time-dependent approach. It will not be used in this thesis yet I will mention it briefly as it relates to previous works to obtain the interquark potential using NRQCD quarks [102].

Rather than considering the correlation function as a linear combination of states, constructing a linear combination of Schrödinger equations, and solving for a single potential which governs all states (including radially excited states), the time-independent approach only considers one state at a time. If we consider equation (5.4) at late times, the correlator becomes dominated by the ground state and one can write a single Schrödinger equation. Using the $\Upsilon(1S)$ state for example,

$$\lim_{\tau\to\infty} C_{\Upsilon(1S)}(\mathbf{r},\tau) = \Psi_{\Upsilon(1S)}(\mathbf{r})e^{-E_{\Upsilon(1S)}\tau}. \tag{5.10}$$

Therefore, one can formulate a single Schrödinger equation to extract the potential, $V_{\Upsilon(1S)}(r)$, that governs only the $\Upsilon(1S)$, through

$$\left(-\frac{\nabla^2}{2\mu} + V_{\Upsilon(1S)}(r)\right)\Psi_{\Upsilon(1S)}(\mathbf{r}) = E_{\Upsilon(1S)}\Psi_{\Upsilon(1S)}(\mathbf{r}). \tag{5.11}$$

This method relies on precise determinations of NBS wavefunctions and whilst states above the ground state can be accessed through a generalised eigenvalue problem (GEVP) method, each potential is only defined insofar as the correlator is dominated by the state of interest. For our example of considering the ground state at late times, the potential would only be defined in a time range where the effective mass of the correlator reaches a plateau and thus it is clear that only ground state contributions exist.

This is not the method that will be explored in this work due to these limitations.

5.3 Finite difference derivatives

The derivatives in equation (5.8) are defined in the continuum where the notion of a continuous derivative is valid. On the lattice, we must approximate these

derivatives with finite differences. A much more rigorous investigation into the effect of the particular choice of finite difference derivative will be explored in Section 6.2.

For the work covered in this chapter we only had access to on-axis data, *i.e.* $C(x, 0, 0, \tau)$ (and the y and z axis permutations). With this limitation, we do not have the data to calculate the Cartesian form of the Laplacian. We therefore considered the form in polar coordinates. It was assumed that because we are considering S-wave correlators the data respect rotational symmetry. As a result of this, we can use the polar form of the Lagrangian and ignore any angular dependence, leaving

$$\nabla^2 f(r) = \frac{\partial^2 f(r)}{\partial r^2} + \frac{2}{r}\frac{\partial f(r)}{\partial r}. \tag{5.12}$$

We use the finite difference form of each derivative that considers only the nearest neighbours. The lattice version of the Laplacian used is

$$\nabla^2 f(r) = \left(\frac{f(r+a_s) - 2f(r) + f(r-a_s)}{a_s^2} + \frac{f(r+a_s) - f(r-a_s)}{r a_s}\right), \tag{5.13}$$

valid up to $\mathcal{O}(a_s^2)$ corrections, as well as unquantified rotational symmetry breaking corrections. We will explore the validity of this spherical symmetry in Section 6.3. In [98] it was shown that this polar form of the Laplacian shows fewer lattice discretisation errors at smaller distances than a Cartesian equivalent on the same data.

The time derivative is approximated by

$$\frac{\partial f}{\partial \tau} = \left(\frac{f(\tau + a_\tau) - f(\tau - a_\tau)}{2a_\tau}\right). \tag{5.14}$$

This is valid up to $\mathcal{O}(a_\tau^2)$ corrections.

Not all lattice sites have a neighbour on both sides. For example, in the temporal axis, the $\tau/a_\tau = 0$ site does not have a neighbour earlier in time, likewise, the $\tau/a_\tau = N_\tau - 1$ site does not have a neighbour later in time. The same effect occurs in the spatial dimensions with the $r/a_s = 0$ and $r/a_s = N_s - 1$ points; there are periodic boundary conditions in the spatial axes, and these would alleviate this problem, but these were not exploited in this chapter. As a result of the lattice sites that do not have a neighbour on each side, the derivatives are only defined for $\tau/a_\tau \in [1, N_\tau - 2]$ and $r/a_s \in [1, N_s - 2]$.

Equation (5.8) expresses the potential as a sum of two terms: one related to the spatial derivative, $\nabla^2 C/(2\mu C)$, and the other from the time derivative, $(1/C)\partial C/\partial\tau$. These will be referred to as the *reduced* spatial and temporal derivative terms respectively. Figure 5.3 shows the behaviour of the first of these contributions; plotted is the reduced spatial derivative against τ for a range of r

and at each of the available temperatures. For all temperatures, the $r = 0$ data show a mild increase with time and when the temporal extent is large enough (equivalent to lattices where T <281 MeV) it plateaus to a τ-independent value. For $r \neq 0$ the data decay with time and these, too, would appear to tend towards a plateau, albeit for high temperature or large separation the plateau is less clear. Clearly, however, when this plateau is reached it does so at different values for each r. Figure 5.4 is the analogous plot but for the reduced time derivative, it shows a similar pattern: all data show a decay with time and at late times appear to plateau, although from the $T = 141$ MeV result the data for all separations tend towards the same value.

5.4 Time window choices

The HAL QCD method uses the time-independent Schrödinger equation. In the previous section, we saw that the constituent terms of equation (5.8) showed time-dependence up to a point, however, there were windows in τ and r that showed approximate τ-independence. Figure 5.5 presents the potential calculated in the vector channel, V_{V}, against τ for a few separations and across all temperatures. One can see that in Figure 5.5 the τ-dependence is reduced in $V_{\mathrm{V}}(\tau)$ compared to the individual reduced derivative terms, shown in Figures 5.3 and 5.4, perhaps with the exception of the reduced spatial derivative at $r = 0$. The same is true of $V_{\mathrm{PS}}(\tau)$. For the HAL QCD method to be valid we would only use ranges of $V_\lambda(\tau, r)$ that showed no τ dependence. This is in contrast to the time-independent HAL QCD method where one requires ground state dominance and can only use time ranges where there is a plateau in $\nabla^2 C/(2\mu C)$ [98]. So, by using the time-dependent approach we have extended the range of validity in τ, allowing for more data to be incorporated into observables. We can use Figure 5.5 to prescribe valid ranges of τ and r based on plateaus of τ-independence in $V_\lambda(\tau)$.

Table 5.1 shows the largest range of r and τ where there exists a clear plateau in both $V_{\mathrm{V}}(r, \tau)$ and $V_{\mathrm{PS}}(r, \tau)$ for each temperature. The optimal time range for each lattice will be different: the data with the least τ-dependence resides at late times, and not all lattices extend as far in time. To make a comparison across different temperatures, in a way that minimises systematic errors, the data will be presented in the following way: for each temperature, there is a longest possible time range determined by that temperature's N_τ, all temperatures with N_τ large enough to span this range will be compared with each other using this same time range. This will be done for each of the possible longest time ranges, one per N_τ corresponding to each row in Table 5.1. Resultantly, each temperature can be reported multiple times and thus not all data will be independent; this is the same treatment as in Section 4.6.2.

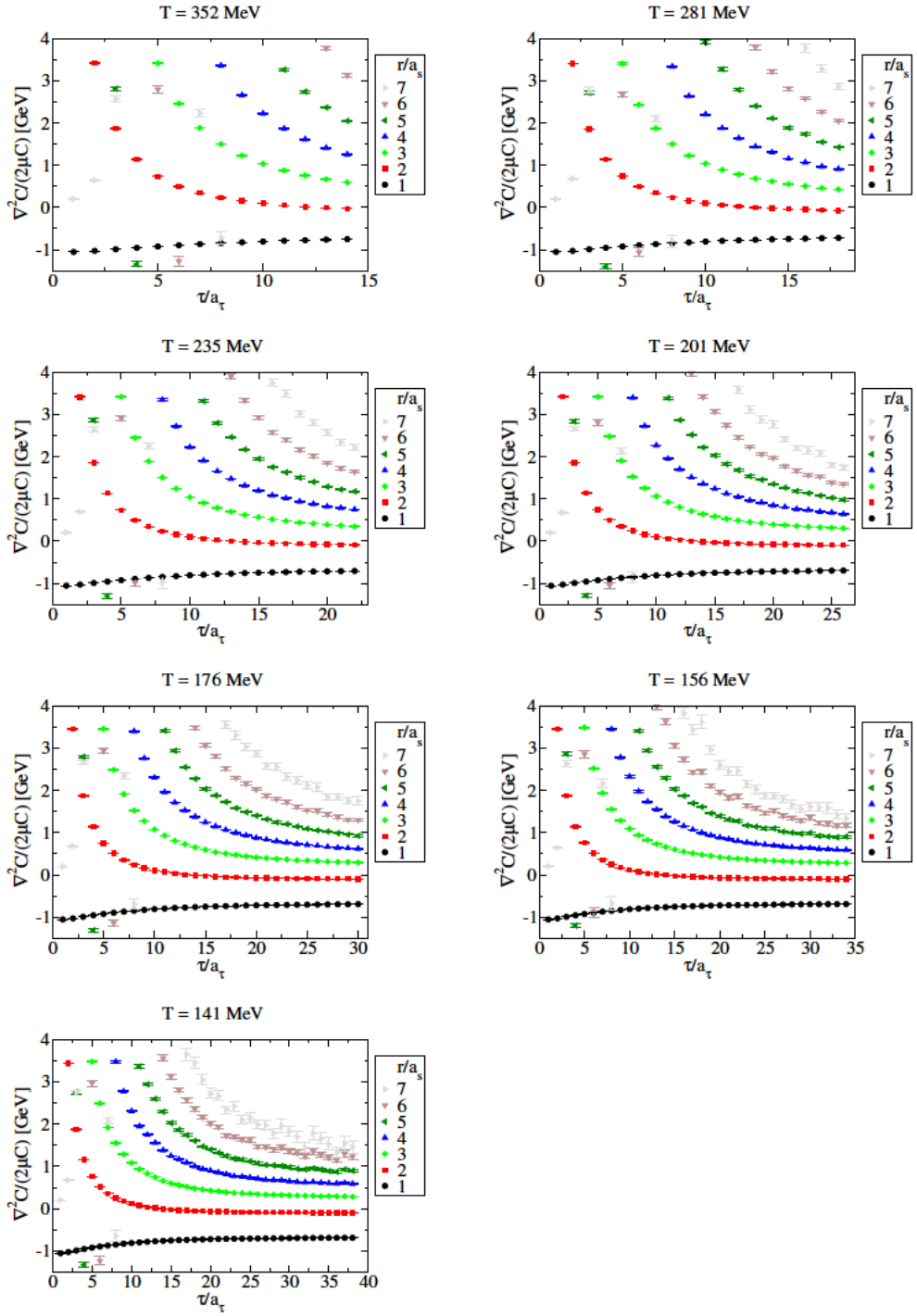

Figure 5.3: The reduced spatial derivative contribution to the vector potential for a range of temperatures. Plotted is the first term in equation 5.8 with τ along the horizontal axis and sink separation, r, labelled by colour. The specific form of the Laplacian is equation (5.13).

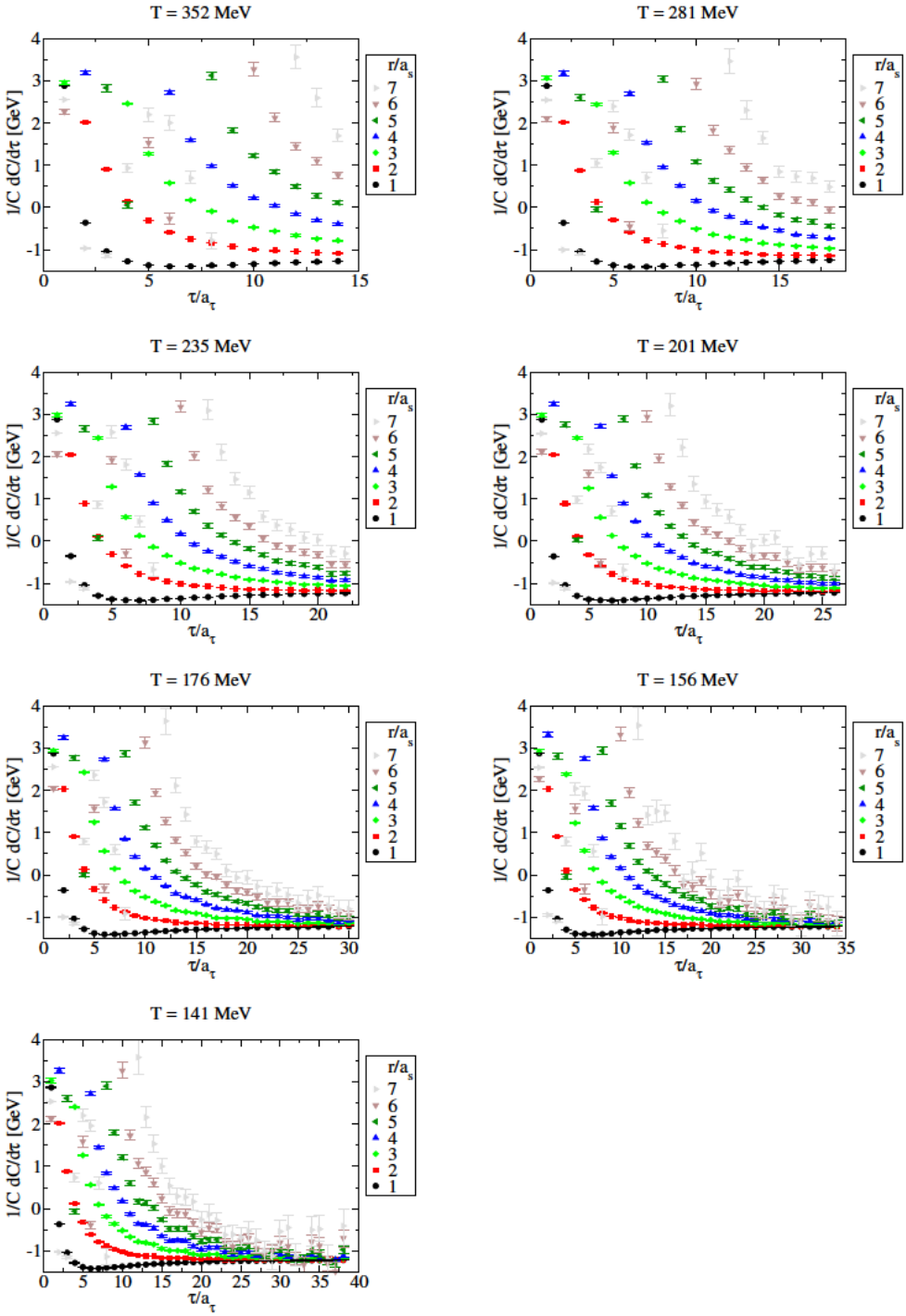

Figure 5.4: The reduced temporal derivative contribution to the vector potential for a range of temperatures. Shown is the second term in equation (5.8), calculated using equation (5.14), with τ along the horizontal axis and sink separation, r, labelled by colour.

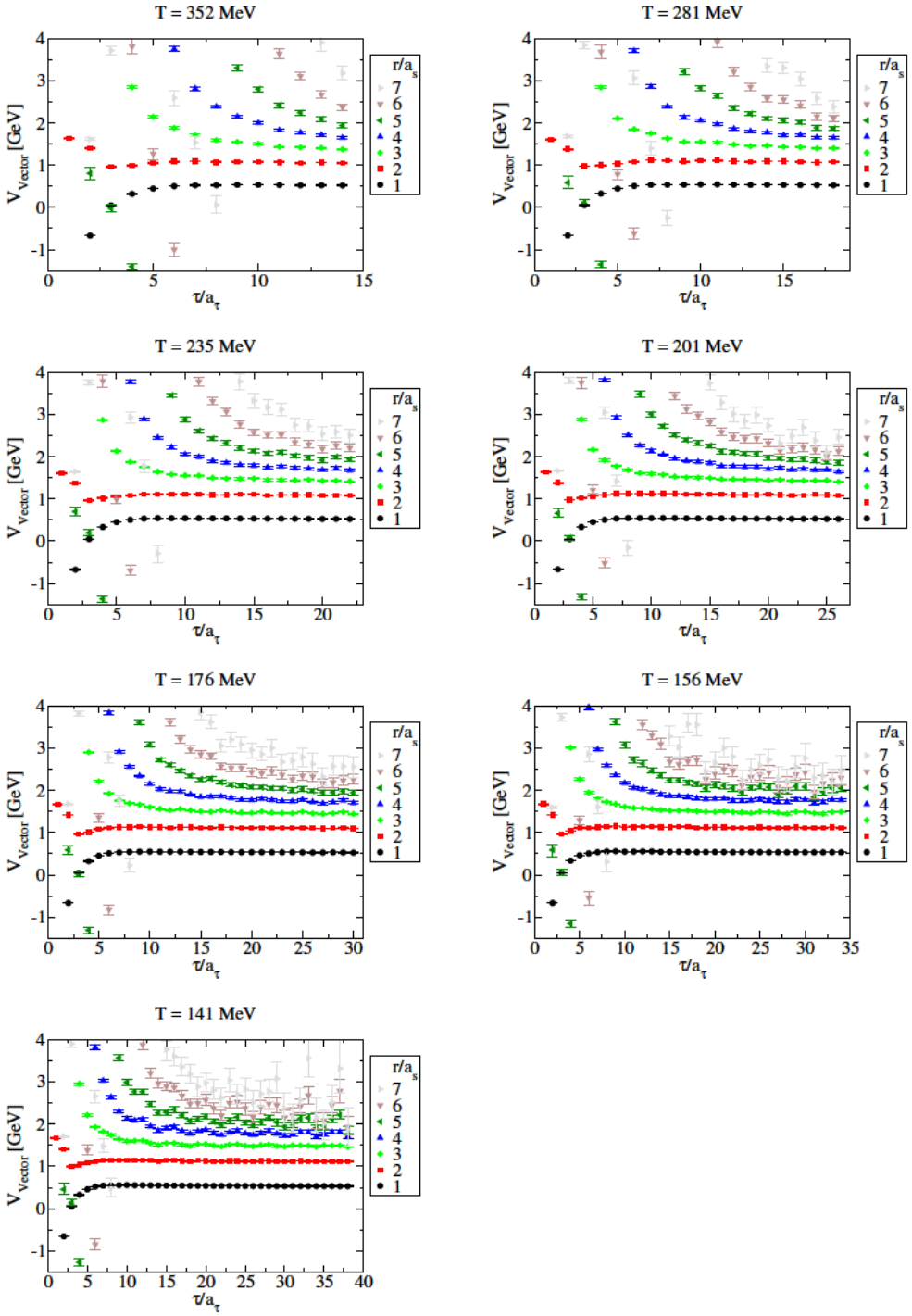

Figure 5.5: The potential calculated using the time-dependent HAL QCD method, equation (5.8), for the vector channel. Note the reduced dependence on τ compared to the constituent terms in equation (5.8) shown in Figures 5.3 and 5.4.

Time window $[a_\tau]$	r range $[a_s]$	r range [fm]	Temperatures [MeV]
$13-14$	$1-3$	$0.12-0.37$	$352-141$
$17-18$	$1-4$	$0.12-0.49$	$281-141$
$19-22$	$1-5$	$0.12-0.61$	$235-141$
$21-26$	$1-5$	$0.12-0.61$	$201-141$
$24-30$	$1-6$	$0.12-0.74$	$176-141$
$24-33$	$1-6$	$0.12-0.74$	$156-141$

Table 5.1: Range of displacements and τ ranges allowed to best approximate time-independence in both $V_{\rm V}(r,\tau)$ and $V_{\rm PS}(r,\tau)$. Note that $T_{\rm pc} = 181$ MeV and thus the time windows below the solid line do not span this pseudocritical temperature.

5.5 Central potential results

Alongside presenting the central potentials calculated from the HAL QCD method, we will also present fits to the Cornell potential from equation (2.10). There are three free parameters in the Cornell potential, we chose to keep the additive constant, C, the same across all of the fits and thus only the coupling, α, and string tension, $\sqrt{\sigma}$, were allowed to vary. The value of C was fit to the coldest data over the longest time range available, $T = 141$ MeV and $\tau \in [24-38]a_\tau$, this resulted in $C = 0.98(1)$ GeV.

Figures 5.6 and 5.7 show the central potential averaged over the time ranges, and plotted over the distances, prescribed in Table 5.1. The first two rows of Table 5.1 correspond to Figure 5.6 and the third and fourth rows to Figure 5.7; the temperature ranges that do not span $T_{\rm pc}$ are not shown. The panels in these figures are presented in this way (with the same time range across the temperatures) to isolate any temperature dependence of the central potential. The symbols show the data calculated from the lattice and the curves are Cornell potentials fit to these data. One can see that there is consistent and significant flattening of the potential with increased temperature above $T_{\rm pc}$ (which, for the generation-2 ensembles, is ~ 181 MeV).

Fits of the Cornell potential were performed on the data shown in Figures 5.6 and 5.7. Figure 5.8 shows the coupling, α, and the string tension, $\sqrt{\sigma}$, that results from these fits against temperature. From Figure 5.8 (bottom) one can see that the string tension decreases fairly consistently with temperature and the decreases are often larger than statistical errors. One would expect this to be how the flattening of the potentials manifests, however the reported values are much larger than was found in [28,98,101,105]. From Figure 5.8 (top), one could argue that α decreases with temperature, however, there are a few anomalous data

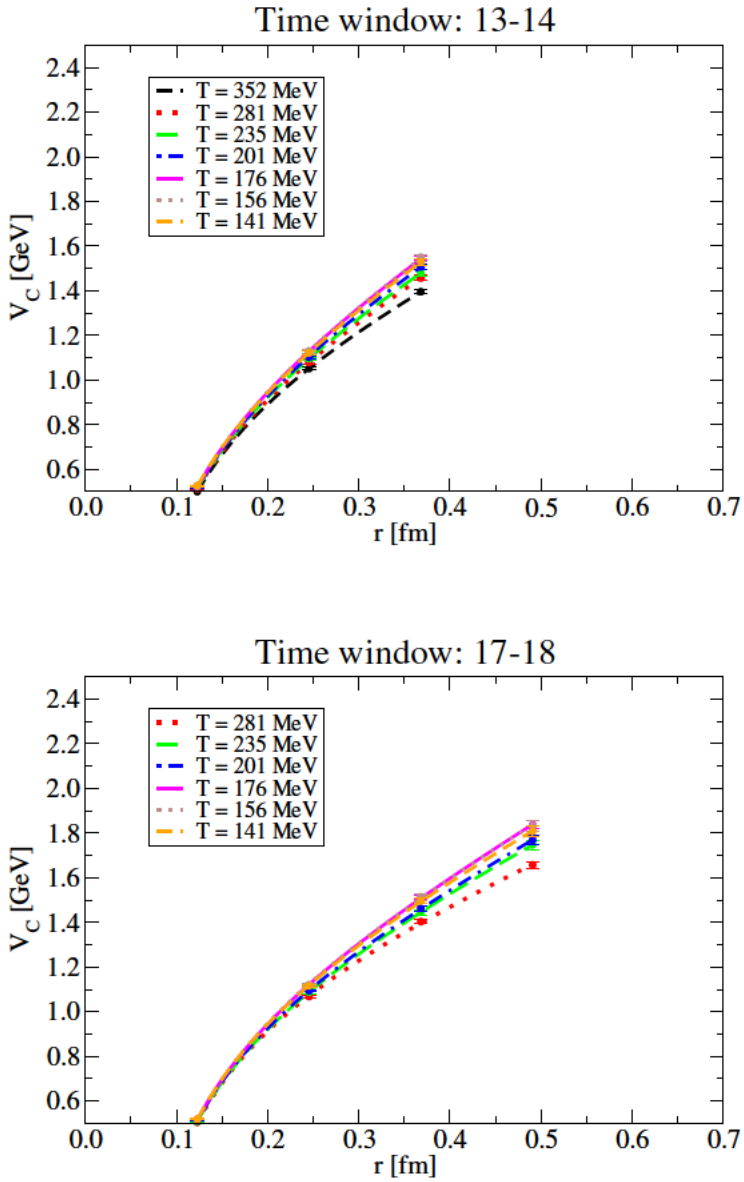

Figure 5.6: The central potential, $V_C(\tau)$, against separation for the time windows from the 1st (top) and 2nd (bottom) rows on Table 5.1. The symbols are the data as calculated on the lattice at integer separations in lattice units (where $a_\tau \sim 0.12$fm). Due to the choice of finite difference derivative, the $r = 0$ point cannot be used. The colour corresponds to different temperatures given in the legend. The lines are the best fit of a Cornell potential, equation (2.10), to each set of points with the same constant shift used for all temperatures and time windows. The same time window is used across all temperatures in the same pane to eliminate this systematic effect and to make comparisons across temperatures easier.

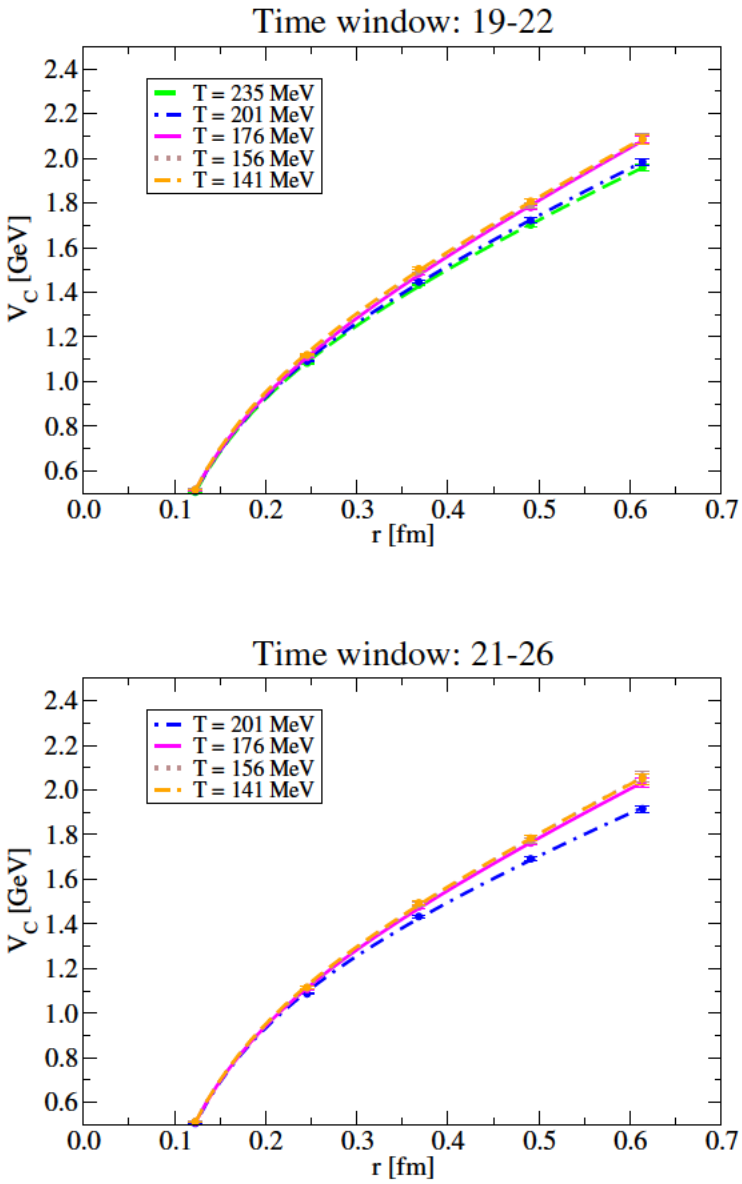

Figure 5.7: As in Figure 5.6 but for the 3rd (top) and 4th (bottom) rows on Table 5.1.

that disagree with this statement. These anomalous data could be an indication that these fits are not suitable, and thus the fit parameters do not carry much weight. Compounding this is the fact that the Cornell potential contains two free parameters (once the shift, C, has been established) and certain time windows only allow for analysis over three distances. Perhaps this leads to the fits fine-tuning to statistical errors which could manifest in fluctuating fit parameters. In Chapter 6 we rectify this with off-axis data increasing spatial resolution and giving more data to fit.

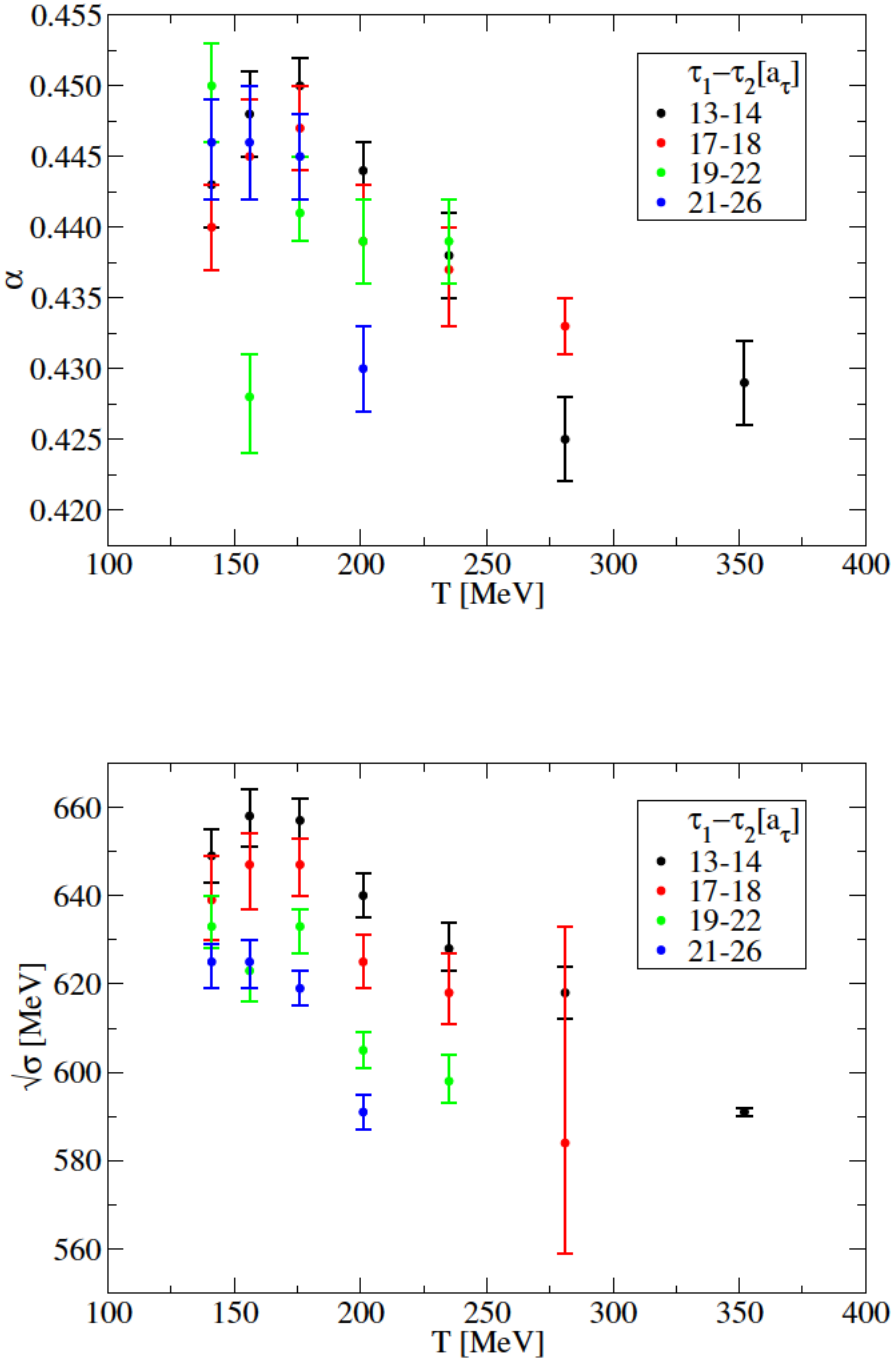

Figure 5.8: The best fit of the coupling, α, (top) and the string tension, $\sqrt{\sigma}$, (bottom) from the Cornell potential in equation (2.10) at each time range (given by the colour) against temperature. The error bars are purely statistical and come from estimates on bootstrapped ensembles.

5.6 Conclusion

In this chapter, I presented our first attempt to calculate the interquark potential for bottomonium using NRQCD quarks. We find evidence for temperature dependence in the form of flattening of the central potential with increased temperature. Fits were performed to the Cornell potential which showed an increase in the string tension with temperature, however, the values of the string tension were much larger than expected. As well as this, the coupling shows non-monotonic variations with temperature. The clearest limitation of this first analysis was the size of the data: there were not enough separations to make robust fits to the Cornell potential. An increase in the resolution of data, by including off-axis separations, along with more rigour across other elements of the method will be developed in the next chapter. As such, further interpretation of the non-zero temperature behaviour of the central potential will be postponed until Section 6.7.

Chapter 6

Improved interquark potential

The previous chapter laid out the initial approach to observe the effect of increasing temperature on the interquark potential. The analysis was limited to only on-axis separations in the sink and it transpired that this coarseness in data affected the analysis: there were not enough data to perform robust fits to phenomenological models and thus we could not reliably extract low energy parameters such as the string tension. The reason for such sparsity of data was the size of the calculation for the point split correlator in equation (5.2). This required a sum over all lattice sites for each separation of the sink, and thus the number of separations was reduced to make this manageable.

In this chapter, we explore a method to drastically reduce the number of computations required to calculate $C_\lambda(\mathbf{r}, \tau)$ for every possible sink separation $\mathbf{r}$. The size of the computation will end up similar to when we calculated only the on-axis separations. Further work will also be shown that explores the effect of different forms of finite derivatives used in calculating the Laplacian, we will explore the lattice discretisation errors present due to the inclusion of off-axis separations, and we will offer an improvement on the HAL QCD method that explicitly tests for time-independence and gives a self-consistent determination of the reduced quark mass μ that differs from that used by the HAL QCD collaboration. Many of these investigations transcend temperature-dependent studies and instead offer a wider review of the HAL QCD methodology and the details of its implementation.

The calculations of this chapter are performed on the FASTSUM generation-2 ensembles.

6.1 Improved point-split correlation function calculation

This section will outline an improvement to the calculation of the point-split correlator that is the basis of the HAL QCD method. Figure 6.1 shows two recipes for calculating this correlator, the method used in Chapter 5 follows the red solid line, and the improved method will follow the blue dashed lines.

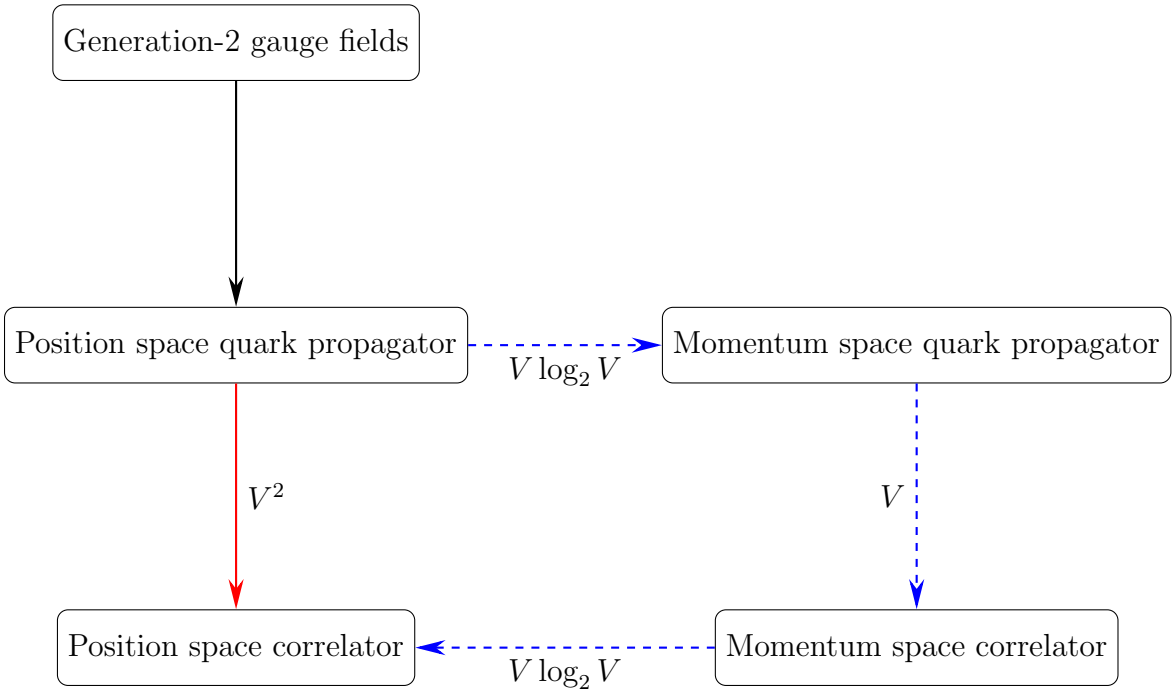

Figure 6.1: The estimated number of terms in the two calculations of the position space point-split correlator if one used every possible quark separation, $\mathbf{r}$. Both methods start from the position space quark propagator and thus the black arrow is common for both. The momentum space representation follows the blue dashed arrows and the terms required for each step are labelled along the arrow; this path corresponds to equations (6.5), (6.8), and (6.7) respectively. The method that did not require a momentum space representation, equation (6.4), is simply the single calculation along the red arrow, this was the approach used in Chapter 5 albeit for fewer separations. $V = 24^3 = 13824$ for this calculation and thus the sum of terms along the blue arrows is significantly fewer than along the red arrow. This is the time-efficient method introduced in this chapter.

6.1.1 Momentum space representation

We begin by combing the two equations pertinent to the calculation of the point-split correlator, equations (5.2) and (5.3). Considering gauge fixed fields, as in Chapter 5, we get

$$C_\lambda(\mathbf{r},\tau) = \sum_{\mathbf{x}} \langle \bar{q}(x)\lambda q(x+\mathbf{r})\bar{q}(0)\lambda^\dagger q(0)\rangle. \tag{6.1}$$

Then we apply Wick's theorem and keep only the terms with non-zero overlap with the vacuum from the connected contribution, meaning we only take the contractions present in

$$C_\lambda(\mathbf{r},\tau) = \sum_{\mathbf{x}} \langle \bar{q}(x)\lambda \overbrace{q(x+\mathbf{r})\bar{q}(0)}\lambda^\dagger q(0)\rangle. \tag{6.2}$$

This gives the correlator in terms of the quark propagator, D^{-1},

$$C_\lambda(\mathbf{r},\tau) = -\sum_{\mathbf{x}} \langle D^{-1}(\mathbf{x}+\mathbf{r},\tau;\mathbf{0},0)\lambda D^{-1}(\mathbf{0},0;\mathbf{x},\tau)\lambda^\dagger\rangle. \tag{6.3}$$

Notationally, $D^{-1}(\mathbf{0},0;\mathbf{x},\tau)$ represents the propagation of a quark from the location $(\mathbf{x},\tau)$ to $(\mathbf{0},0)$. Currently, equation (6.3) requires computing the propagator from all sources to sinks, and then again for propagating from all sinks to all sources. To avoid this, and to leave only the calculation of the propagation from source to sink, we exploit the γ_5-hermiticity of the quark propagator, $D^{-1}(\mathbf{0},0;\mathbf{x},\tau) = \gamma_5 \left(D^{-1}(\mathbf{x},\tau;\mathbf{0},0)\right)^\dagger \gamma_5$, to give the rewritten form of the point-split correlator. I will refer to this as the position space point-split correlator for reasons that will become apparent, it reads

$$C_\lambda(\mathbf{r},\tau) = -\sum_{\mathbf{x}} \langle D^{-1}(\mathbf{x}+\mathbf{r},\tau;\mathbf{0},0)\lambda\gamma_5 \left(D^{-1}(\mathbf{x},\tau;\mathbf{0},0)\right)^\dagger \gamma_5\lambda^\dagger\rangle. \tag{6.4}$$

The rewriting of equation (5.2) into equation (6.4) does not change any details of the calculation, but we will use this newer form to introduce the momentum space representation of the quark propagator. This, in turn, will highlight the time savings that make this calculation feasible for all separations $\mathbf{r}$. To perform the calculation for all possible sink separations requires calculating the expectation value in equation (6.4) $N_s^3 \times N_s^3$ times for each time-slice. I will define $V = N_s^3$ and say this calculation requires $\mathcal{O}(V^2)$ calculations per τ. The direct calculation of equation (6.4) corresponds to the red line in Figure 6.1.

We define the momentum space quark propagator, $\tilde{D}^{-1}(\mathbf{q},\tau)$, as the Fourier transform of the position space quark propagator through

$$D^{-1}(\mathbf{x},\tau;\mathbf{0},0) = \frac{1}{V}\sum_{\mathbf{p}} \tilde{D}^{-1}(\mathbf{p},\tau)e^{i\mathbf{x}\cdot\mathbf{p}}. \tag{6.5}$$

We have introduced a 3-momentum, $\mathbf{p}$, that is conjugate to the separation of the two quarks, it is not, therefore, the overall quark momentum. Inserting this definition into equation (6.4) yields

$$C_\lambda(\mathbf{r},\tau) = \frac{1}{V}\sum_{\mathbf{p}} \langle \tilde{D}^{-1}(\mathbf{p},\tau)\lambda\gamma_5\tilde{D}^{-1}(-\mathbf{p},\tau)\gamma_5\lambda^\dagger\rangle e^{i\mathbf{p}\cdot\mathbf{r}}. \tag{6.6}$$

We can use this form to implicitly define the momentum space quark propagator

$$C_\lambda(\mathbf{r},\tau) = \frac{1}{V}\sum_{\mathbf{p}} \tilde{C}_\lambda(\mathbf{p},\tau) e^{i\mathbf{p}\cdot\mathbf{r}}, \tag{6.7}$$

such that

$$\tilde{C}_\lambda(\mathbf{p},\tau) = \langle \tilde{D}^{-1}(\mathbf{p},\tau)\lambda\gamma_5\tilde{D}^{-1}(-\mathbf{p},\tau)\gamma_5\lambda^\dagger\rangle. \tag{6.8}$$

It would seem there are more steps to calculating equation (6.7) than before, but I will now stress how each is computationally cheaper such that the combination of the extra steps still costs less than the original one-step of equation (6.4). A result used twice here is that a discrete Fourier transform (DFT) contains a lot of redundancy. The fast Fourier transform (FFT) algorithm is an exact algorithm to compute the DFT without any redundancy, it scales, for a system of size V, as $V\log_2(V)$ operations; the naive DFT implementation scales as V^2. With that in mind, the conversion from the position space quark propagator to the momentum space propagator (equation (6.5)) is a Fourier transform and thus, using the FFT algorithm, this requires $V\log_2(V)$ terms. The calculation of the momentum space correlator from the momentum space quark propagator (equation (6.8)) does not depend on the source separation and thus requires only V terms. Finally, the conversion back from momentum space to get the position space quark propagator (equation (6.7)) is also a Fourier transform, so it, too, requires $V\log_2(V)$ terms. Summing up these contributions, one arrives at a rough cost of $2\times V\log_2(V)+V$ terms. For $N_s = 24, V = 13824$ and thus comparing the cost of the two recipes for this specific lattice size, one see that $V^2 >> 2\times V\log_2(V)+V$. Approximately 200,000,000 terms are reduced to around 400,000. These two calculation recipes are shown in Figure 6.1.

For this consideration, we have assumed that the cost of a single term in a sum (for example, the expectation value in equation (6.4) for a single $\mathbf{r}$, $\mathbf{x}$, and τ) is fixed and any variation in its complexity does not contribute as significantly to the total cost as the number of terms that need to be calculated does. However, given the magnitude of the reduction in the number of terms, an extra few basic numerical operations per term would not overcome the computational saving and thus this assumption is not strictly needed.

6.1.2 Validating the correlation function

The discrete Fourier transform as a pairing between samples is exact. One can say that the data $C(\mathbf{r})$ take values in a position space of size N_s^3 with a particular basis of vectors, and $\tilde{C}(\mathbf{p})$ is simply a rewriting of the same information in a momentum space of the same size but with a different set of basis vectors. The problem becomes when one tries and represent an underlying continuous function with a set of discrete samples [114].

In general, one cannot take a function, perform a Fourier transform, perform an operation on this new representation and then expect the inverse Fourier transform of this final product to relate simply with the original function. This is what we did when we rewrote the calculation of the position space correlator in terms of momentum space representations. However, in this case, the convolution property of Fourier transforms allowed for a simple relation between the position and momentum space correlators.

We can check the convergence of a Fourier transform, that is to say how well the momentum space representation captures the information from the position space representation. Here it is helpful to consider a Fourier transform as a Fourier series, and the values of the momentum space representation being the Fourier coefficients of the finite series. For example, rather than considering $\tilde{C}(\mathbf{p}, \tau)$ a set of points sampling an underlying function, one could consider each $\tilde{C}(\mathbf{p}, \tau)$ the Fourier coefficient of the series with momentum $\mathbf{p}$. If the coefficients keep growing with momentum then it could be said that the momentum basis is not large enough to capture all of the information. This is known as the problem of aliasing whereby a discrete Fourier transform is calculated up to an insufficiently large momentum. (Often analogies are drawn to time and frequency domains, I will stick with position and momentum here but the reader should be aware of the dictionary between the two.) In this case, effects caused by one momentum may be attributed to another momentum, and thus the Fourier-transformed samples do not fully represent the original underlying function. Consider two sinusoids sampled at equally spaced positions, x, for an integer, n, and a small number, ϵ: $\cos[\pi(n+\epsilon)x+\phi]$ and $\cos[\pi(n-\epsilon)x-\phi]$. The values of both sinusoids are the same at the sampled points ($x = 1, 2, 3,$ *etc.*), but different elsewhere. Therefore, equipped with only the knowledge of the sampled points one cannot discern between the contributions from either wave and thus effects from different frequencies can be erroneously mixed [115]. The sampling theorem tells us that the solution is to make the sampling frequency larger than twice the maximum frequency of the system (i.e. to make the lattice spacing small enough to capture the highest momentum contributions). This is not possible given the computational demands of a lattice QCD simulation, so we know we are likely not avoiding aliasing completely but we observe the coefficients of the highest

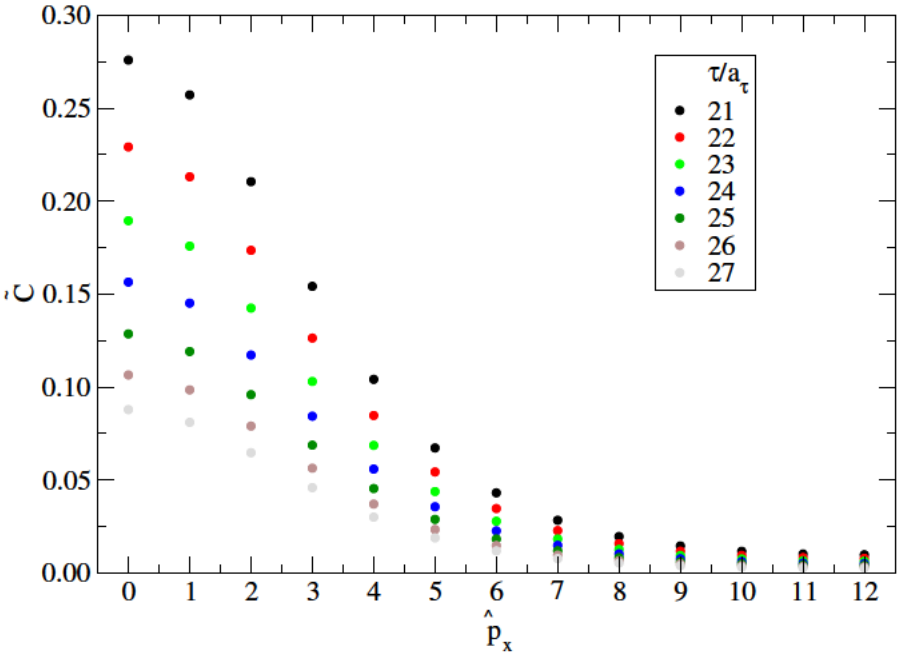

Figure 6.2: The momentum space correlator along the $(\hat{p}_x, 0, 0)$ momentum axis at late times at $T = 201$ MeV ($N_\tau = 28$). This can also be considered as the contribution to the position space correlator from each momentum, where the momentum $p = 2\pi\hat{p}/N_s$. Clearly, the contribution from each momentum decreases as the momentum increases.

momentum contributions to measure the severity.

Figure 6.2 shows the momentum space correlation function against momentum, which, as mentioned above, can be considered the magnitude of the contributions to the Fourier transform (that leads to the position space correlation function) at a given momentum. We can see in Figure 6.2 that the contribution from each momentum decreases at larger momentum. This suggests that we do not have severe aliasing problems and that the Fourier transform that recovered the position space correlator from the momentum space correlator is valid.

The more obvious test of this alternative approach is to compare the resulting correlator to the correlator calculated using the original approach. This is made slightly less trivial by some of the finer details of NRQCD calculations, namely a parameter called the Lepage parameter presented in Section 3.5. This parameter, introduced in [42], is included to add stability to the propagation of quarks

through time. The size of this parameter, which takes integer values of $\mathcal{O}(1)$, was found to take different optimal values for propagating a quark in position space (see Chapter 5) than for propagating in momentum space (this chapter). Despite the momentum space representation only having fewer computational operations if the fast Fourier transform is used, the regular discrete Fourier transform was actually used for this work. This increase in the number of computational operations makes the calculation more susceptible to rounding errors: the Lepage parameter was increased to circumvent this. As a result of different values for the Lepage parameter, a direct comparison between the two results is non-trivial. One should note that both simulations, despite using different Lepage parameters, are physically representative and that the parameter is only to control the order of a Taylor expansion. To allow for an easier comparison, we generated a single correlator from both methods using the same Lepage parameter (the value used in Chapter 5 rather than the rest of this chapter). This comparison of the on-axis correlator from Chapter 5 and the correlator from this chapter with the same Lepage parameter (and all other NRQCD parameters that were always the same) is shown in Figure 6.3. To interpret this figure one must acknowledge the periodic boundaries, meaning that the data at $x = 1$ and $x = 23$ (and all x, $N_s - x$ pairs) would be identical if the symmetries we expect on the lattice (explored in Section 6.3.1) were perfectly upheld. The data, at the late times shown, show remarkable agreement for $x/a_s < 4$ and $x/a_s > 20$, agree within 0.5% up to $x/a_s = 7$ and from $x/a_s = 17$ onwards, and then exhibit worsening agreement towards the centre of the lattice. This is likely due to the presence of rounding errors but it cannot be solely attributed to one computation being superior: neighbouring lattice sites are more correlated as the updates that are made to gauge fields during the MCMC procedure are only local, therefore large separations are less correlated and inherently more noisy. Care must be taken when making statements significantly beyond $7a_s$, but these data still carry some validity.

With the comparison to the old data concluded, we can now exploit the off-axis sink separations to increase the granularity of our data. See Figure 6.4 for the time dependence of the coldest correlator at the first 20 sink separations. For ease of comparison the separations have been converted into polar distance, r, however, as will be explored in Section 6.3.2, this is not always a trivial change of coordinates. The spatial dependence of the correlator is shown in Figure 6.5 for late times.

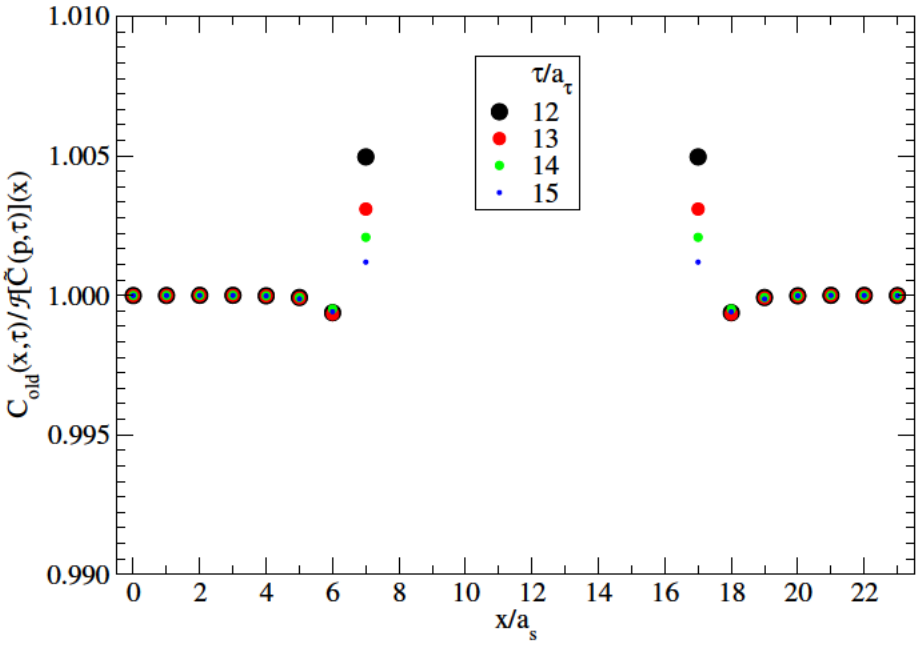

Figure 6.3: The ratio of the on-axis position space correlator from Chapter 5 (suffixed 'old') to the new data that is calculated from the Fourier transform of the momentum space correlator, defined in equation (6.6). See Section 6.1.2 for more details of this comparison. This comparison is made for a single configuration.

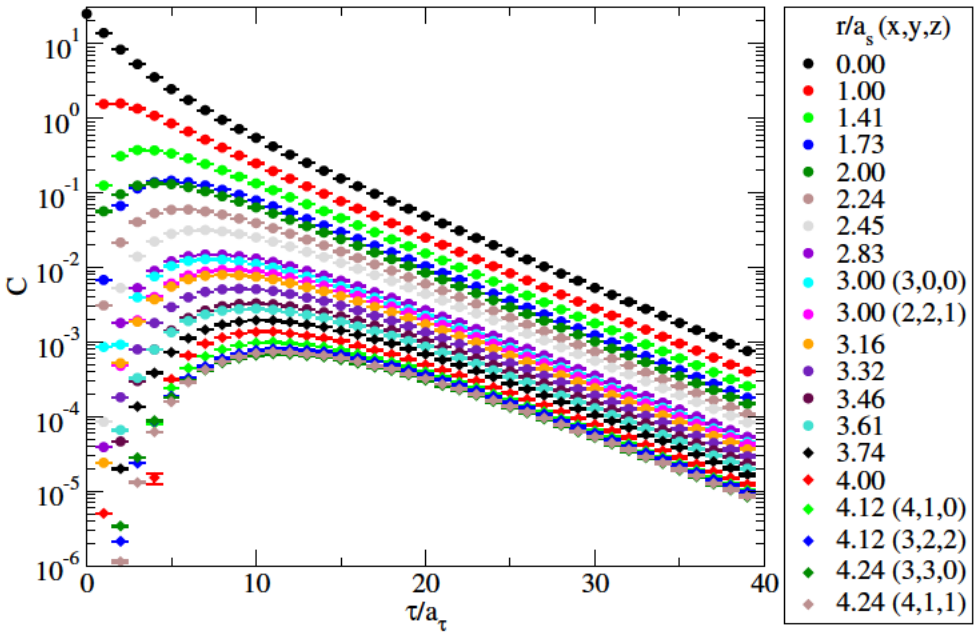

Figure 6.4: The position space correlator against imaginary time for the $T = 141$ MeV ($N_\tau = 40$) correlator, vector channel. The degeneracies in the conversion from Cartesian to polar coordinates are elaborated with the corresponding (x, y, z) Cartesian coordinate where necessary. Errors shown are purely statistical and the cubic group symmetries have been averaged over, see Section 6.3.1 for more details.

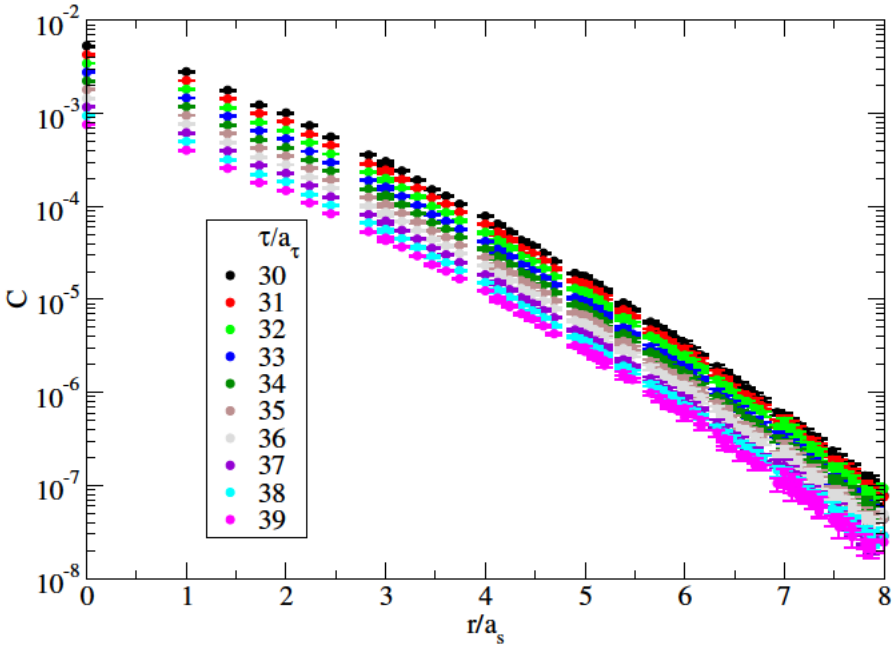

Figure 6.5: The position space correlator against polar distance at late times for the $T = 141$ MeV ($N_\tau = 40$) correlator, vector channel. Errors shown are purely statistical and the cubic group symmetries have been averaged over, see Section 6.3.1 for more details.

6.2 Finite derivatives

In Section 5.3 we used the simplest form of the finite difference derivative to calculate both the Laplacian and time derivative. For both, we used the nearest neighbour finite derivative that did not take into account the periodic boundary conditions (PBC). In this section, I will consider two possible improvements to the Laplacian: increasing the number of neighbours considered in the finite difference derivative (Section 6.2.1), and exploiting the momentum space correlator to perform the derivative (Section 6.2.2). I will then consider improvements to the time derivative (Section 6.2.3) that, as it transpires, do not overcome their shortcomings.

In the previous work, we only had access to on-axis data and thus we could not take nearest neighbours in more than one dimension at a time, this limitation is not present in this chapter. For both new Laplacian methods, the PBC will be used as well as the entire space of on- and off-axis points. Therefore each method will calculate

$$\nabla^2 C(\mathbf{r},\tau) = \frac{d^2}{dx^2}C(\mathbf{r},\tau) + \frac{d^2}{dy^2}C(\mathbf{r},\tau) + \frac{d^2}{dz^2}C(\mathbf{r},\tau). \tag{6.9}$$

6.2.1 Increased accuracy finite difference Laplacian

When approximating a continuous derivative with a finite difference derivative there is a choice of how accurate that approximation is. The more neighbours included in the finite difference the more accurate the approximation. On a finite lattice, there is a natural limit to this as there are only $N_s - 1$ neighbours to each point. However, there is also a trade-off between accuracy and the cost of the calculation, therefore some time will be spent finding this balance.

Using a Taylor series of an arbitrary function, $f(x)$, one can build up more and more accurate finite derivatives and quantify the order of corrections. The

first four lowest order central difference second derivatives are [116]

$$
\begin{aligned}
\frac{d^2}{dx^2}f(x) &= \frac{1}{a^2}\bigg(f(x-a) - 2f(x) + f(x+a)\bigg) + \mathcal{O}(a^2), \\
\frac{d^2}{dx^2}f(x) &= \frac{1}{a^2}\bigg(-\frac{1}{12}f(x-2a) + \frac{4}{3}f(x-a) - \frac{5}{2}f(x) \\
&\qquad + \frac{4}{3}f(x+a) - \frac{1}{12}f(x+2a)\bigg) + \mathcal{O}(a^3), \\
\frac{d^2}{dx^2}f(x) &= \frac{1}{a^2}\bigg(\frac{1}{90}f(x-3a) - \frac{3}{20}f(x-2a) + \frac{3}{2}f(x-a) - \frac{49}{18}f(x) \\
&\qquad + \frac{3}{2}f(x+a) - \frac{3}{20}f(x+2a) + \frac{1}{90}f(x+3a)\bigg) + \mathcal{O}(a^4), \\
\frac{d^2}{dx^2}f(x) &= \frac{1}{a^2}\bigg(-\frac{1}{560}f(x-4a) + \frac{8}{315}f(x-3a) - \frac{1}{5}f(x-2a) \\
&\qquad + \frac{8}{5}f(x-a) - \frac{205}{72}f(x) + \frac{8}{5}f(x+a) - \frac{1}{5}f(x+2a) \\
&\qquad + \frac{8}{315}f(x+3a) - \frac{1}{560}f(x+4a)\bigg) + \mathcal{O}(a^5).
\end{aligned}
\tag{6.10}
$$

Figure 6.6 shows the potential computed using various accuracies of the Laplacian, the four from equation (6.10) and the form used in Chapter 5 (equation (5.13)). Taken for this example is the pseudoscalar potential at $T = 235$ MeV at time $\tau/a_\tau = 22$, however, the effect present is replicated across different temperatures and times. The data are shown along a single axis, labelled x for convenience, as this was all that was available for the analysis in Chapter 5. All data in the figure are from the same correlator that is defined for every separation on the lattice, however treating it in this way, *i.e.* exactly like the data from the previous chapter, allows us to probe those results. The effect of increasing the accuracy of the Laplacian has two features: firstly, the direction of the correction flips with each subsequent increase, and secondly, the magnitude of the correction diminishes with the increased accuracy. The fact the corrections get smaller with each subsequent increase in accuracy is promising, it suggests that the finite derivatives are converging on the true derivative. These diminishing returns led us to stop at the four neighbour finite derivative and use this to calculate the Laplacian in this work. What can also be seen from Figure 6.6 is that the one neighbour d^2/dr^2 Laplacian used in Section 5.3 leads to a potential that grows much quicker than the higher accuracy derivatives. This is likely the explanation for such large string tensions reported in the Cornell potential fits of Section 5.5.

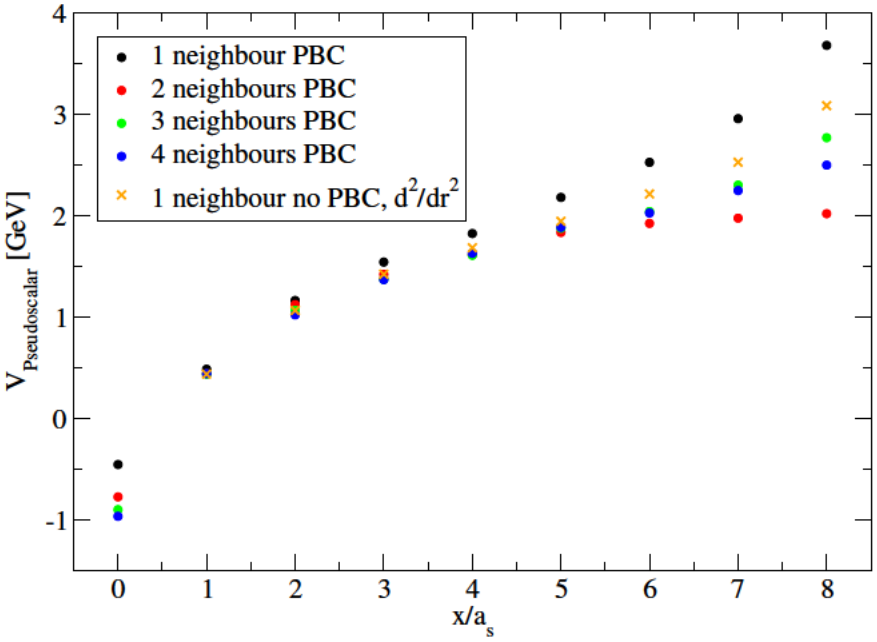

Figure 6.6: The potential from the pseudoscalar channel when the Laplacian is calculated using differing forms. The circle markers are the four forms from equation (6.10) in the order in which they appear. The *N neighbour(s)* refers to the number of neighbours on either side of the central value used for the finite difference derivative. The data marked with crosses are from the form of the Laplacian that was used in Section 5.3: calculating d^2/dr^2 (whereas the circles are $d^2/dx^2+d^2/dy^2+d^2/dz^2$) and not using periodic boundary conditions (PBC): this is why there is no $x = 0$ point. This potential is at $T = 235$ MeV with $\tau/a_\tau = 22$ as an illustrative example.

6.2.2 Momentum space Laplacian

In Section 6.1.1 we introduced the momentum space correlator as a stepping stone that reduced computational costs. However, this representation can be further exploited by noting the following identity for Fourier transforms: let the Fourier transform of $F(p)$ be $f(x)$ (*i.e.* $f(x) = \mathcal{F}[F(p)](x)$), then

$$\frac{d^2}{dx^2} f(x) = \frac{1}{V} \frac{d^2}{dx^2} \sum_p F(p) e^{-ipx} = \frac{1}{V} \sum_p -p^2 F(p) e^{-ipx} = -\mathcal{F}[p^2 F(p)](x). \tag{6.11}$$

Using this identity we can calculate the derivative of the position space correlator from the momentum space correlator without needing nearest neighbour derivatives. Therefore, the form of the Laplacian using this approach is

$$\nabla^2 C(\mathbf{r}, \tau) = -\mathcal{F}[(p_x^2 + p_y^2 + p_z^2) C(\mathbf{p}, \tau)](\mathbf{r}). \tag{6.12}$$

There comes a word of caution when calculating the derivative of functions this way. A Fourier transform of a finite set of data will always capture the information from this set, however, due to the finite sampling it may not always capture the information about the true, underlying, continuous function that gave these sampled data. This can lead to an incorrect calculation of the gradient or Laplacian.

Figure 6.7 shows the reduced spatial derivative term in the potential when calculated using two different forms of the Laplacian, the momentum space representation that has just been introduced and the four-neighbour form from the previous subsection, *i.e.* the final expression of (6.10). By comparing the two resulting reduced spatial derivative terms in this figure one can see "filaments" where the two methods strongly disagree. As this plot contains all x, y, z converted into polar distance r, it contains multiple values for certain r for which there is a degeneracy in the coordinate conversion (I will go into more details of the symmetries and coordinate systems in Section 6.3). From this multivalued nature one can see that although these filaments occur near the on-axis values, it does not occur for all points and is suggestive of a discrepancy between on- and off-axis data: this is an artefact of discretisation errors on the lattice.

Figure 6.8 shows the reduced spatial derivative term from the momentum space Laplacian in the two-dimensional x, y plane at $z = 0$. This figure reaffirms that these filaments are caused by discretisation effects as the data that lie within a small cone centred along each axis contain very different values to the rest of the lattice. Combined, Figures 6.7 and 6.8 show that this method is too prone to discretisation errors to be used.

In an effort to address why the momentum space Laplacian is not appropriate, we consider the convergence of the transform. To test this we consider the size

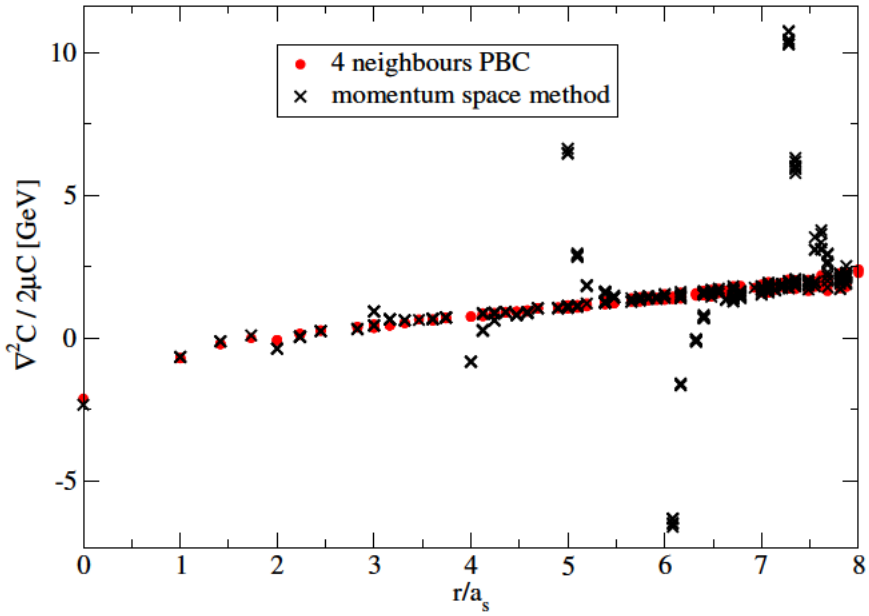

Figure 6.7: The reduced spatial derivative term from equation (5.8) calculated by two different approximations of the Laplacian applied to the $T = 201$ MeV vector channel correlator. The best approximation from Section 6.2.1 (the four-neighbour finite difference) is shown in red, whereas the method that exploits the momentum space representation is in black. The latter method disagrees with the four-neighbour Laplacian around integer values of r/a_s. The full lattice of Cartesian x, y, z are plotted once projected into the polar coordinate r, therefore, due to degeneracies in this coordinate transform, multiple values are reported at certain distances.

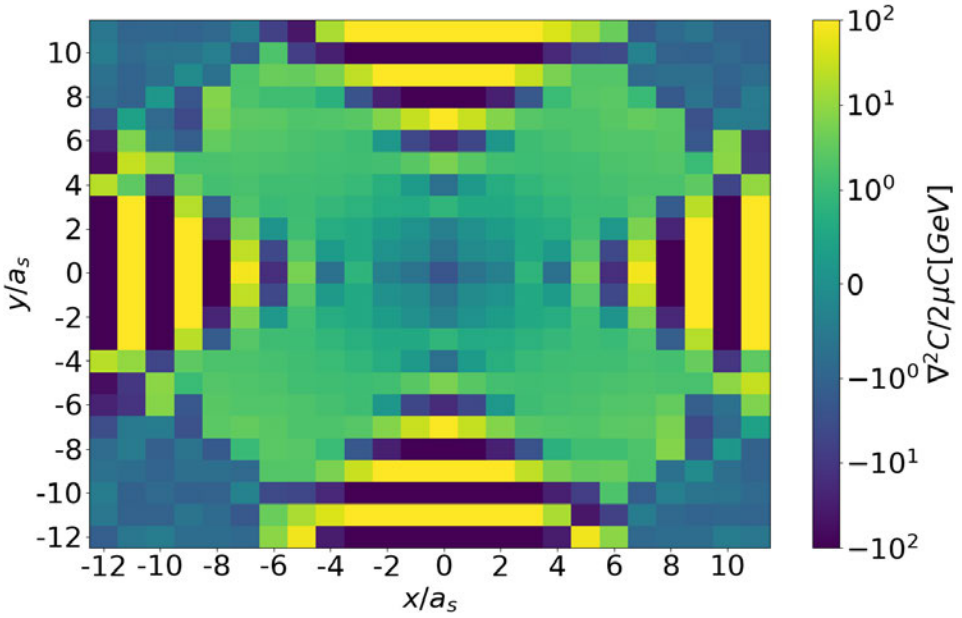

Figure 6.8: The reduced spatial derivative term from the $N_\tau = 28$, $T = 201$ MeV vector channel correlator, viewing a slice of the lattice where $z = 0$. The data are shown in the range [-12,12) rather than [0,24) to highlight the symmetry. The colour scale is designed to show the order of magnitude differences between the very off-axis data and the data that lie near the axis. The highly oscillatory areas are the cause of the filaments in Figure 6.7.

of each term in the Fourier transform as a function of momenta, *i.e.* $(p_x^2 + p_y^2 + p_z^2)C(\mathbf{p}, \tau)$. An increasing contribution from higher momentum terms is suggestive that our momentum range is not large enough to truly represent the data. Figure 6.9 shows the size of each on-axis term that enters into the Fourier transform calculation of the Laplacian, equation (6.12). From this we can see that these terms are still increasing in magnitude at large momentum; this suggests that there are higher momentum contributions that are not being accounted for in our range of allowed momenta (consider how this figure differs from Figure 6.2). This range is fixed by the number of spatial points in our lattice, and for a fixed physical size the only way to increase the range of momenta is to decrease the lattice spacing. Therefore, this is a manifestation of a lattice discretisation effect.

Moving forward, the Laplacian will be calculated using the four-neighbour finite derivative from Section 6.2.1.

6.2.3 Time derivative

The time direction does not have PBC, therefore there will always be points in time that do not have enough neighbours to take the nearest neighbour derivative. Earlier, in Section 5.3, we identified that using a single neighbour for the finite distance in time lost access to the $\tau/a_\tau = 0$ and $\tau/a_\tau = N_\tau - 1$ points. The data at large times are expected to contain the least time-dependence and thus are the most important data for calculating the potential: losing more data at late times would not be ideal. Therefore, we chose against increasing the accuracy of this derivative at the expense of the data at late times. As an alternative to the central finite difference derivative, there is the backwards finite difference derivative which would only prevent access to the derivative at early times. However, this is known to be less accurate for the same number of neighbours considered; even higher order approximations of the backwards derivative contained more noise than the one-neighbour approximation of the central derivative that was used in Chapter 5. For both reasons, it was decided against changing the form of the time derivative and we will continue to use equation (5.14).

6.3 Spatial symmetries

Considering only the spatial dimensions, the action of lattice QCD is invariant under transformations of the cubic group. These transformations are built from any combination of reflections in the plane of either $x = 0$, $y = 0$, or $z = 0$, and/or rotations about the x, y, or z axes by an angle of $\pi/2$. In the continuum, QCD is invariant under these reflections but also rotations of an arbitrary angle,

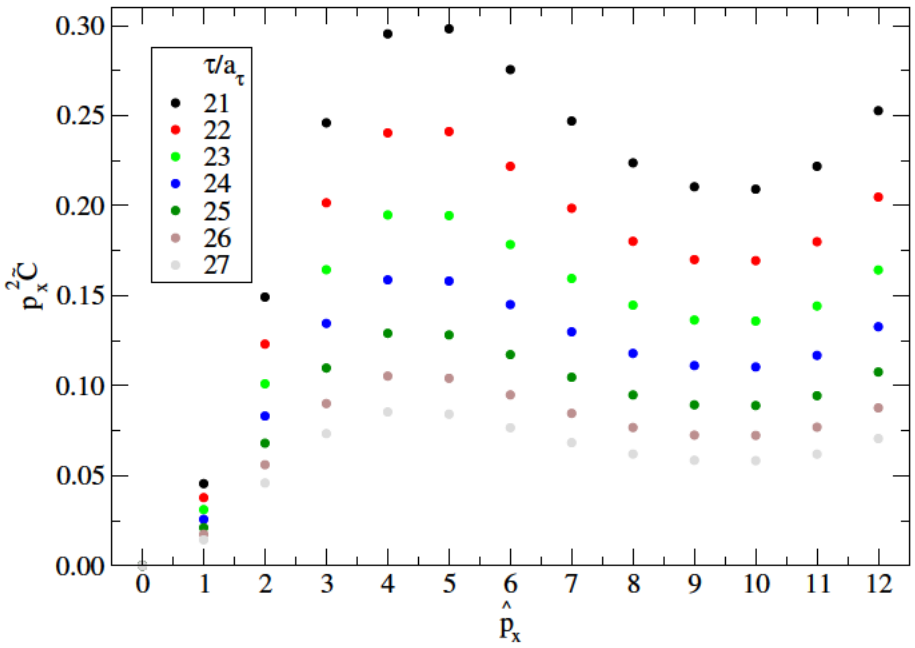

Figure 6.9: The size of each on-axis term that enters the Fourier transform that calculates the Laplacian, equation (6.12). Clearly, the size of the term is not diminishing as the momentum increases, this suggests that the Fourier transform is unable to truly represent the continuous function that $\tilde{C}$ is sampled from. Compare this to Figure 6.2 where the contribution did diminish at high momentum. Here, too, $T = 201$ MeV ($N_\tau = 28$). The physical momentum, p, is related to $\hat{p}$ through $p = 2\pi\hat{p}/N_s$.

it is the finite lattice spacing that breaks the continuous rotational symmetry.

Calculating observables on the lattice requires Monte Carlo integration and thus the symmetries of the cubic group are only exact in the limit of infinite statistics. In this section, we will explore the extent to which these exact symmetries are conserved as well as the size of symmetry breaking effects caused by the non-zero lattice spacing. We will end with an approach to minimise the impact of these symmetry breaking effects.

6.3.1 Exactly conserved symmetries

With finite data, we can explore how well the symmetries are respected and how this changes with the number of data. Figure 6.10 shows the correlator at three different sets of (x, y, z), for each set we plot the value of the correlator at every point that is related to (x, y, z) by a reflection and/or rotations of $\pi/2$, for example $(-z, y, x)$. This is shown for a correlator comprised of 10, 100, and 1,000 configurations and one can see how the spread shrinks with increased statistics. Once the correlator is the mean of 1,000 configurations, the spread of data is between 2 and 4 per cent for the separations shown. The relative spread is larger with increased separation.

For values of x, y, z that are all different there are 48 symmetric partners, therefore, there is a huge statistical benefit to averaging over these points. Since the data have passed this cubic symmetry check, all results shown beyond this and the following subsections will be for data that has been averaged over the symmetries of this group.

Averaging over the cubic symmetries of the correlator commutes with taking the finite difference derivative, therefore, as the space spanned by the set of points after averaging is more complex than the original lattice, the derivative is taken before averaging over symmetries.

6.3.2 Continuous rotation symmetry breaking

A relic of the broken continuous rotational symmetry is that the polar distance, $r = \sqrt{x^2 + y^2 + z^2}$, is not a good measure of distance. Consider two point-split sinks at $(x, y, z) = (2, 2, 1)a_s$ and $(3, 0, 0)a_s$, there are 5 and 3 links separating these sinks from $(0, 0, 0)$ respectively, yet in the continuum they are both a distance of $3a_s$ from the origin. Figure 6.11 presents the difference between points that are related due to the cubic symmetries of the previous subsection and the points that are related by continuous rotational symmetry. The correlator is plotted at a few values of r, where at each r there are two different symbols (but the same colour), points that are the same symbols are related by exact symmetries and points given by different symbols are related only by continuous rotation.

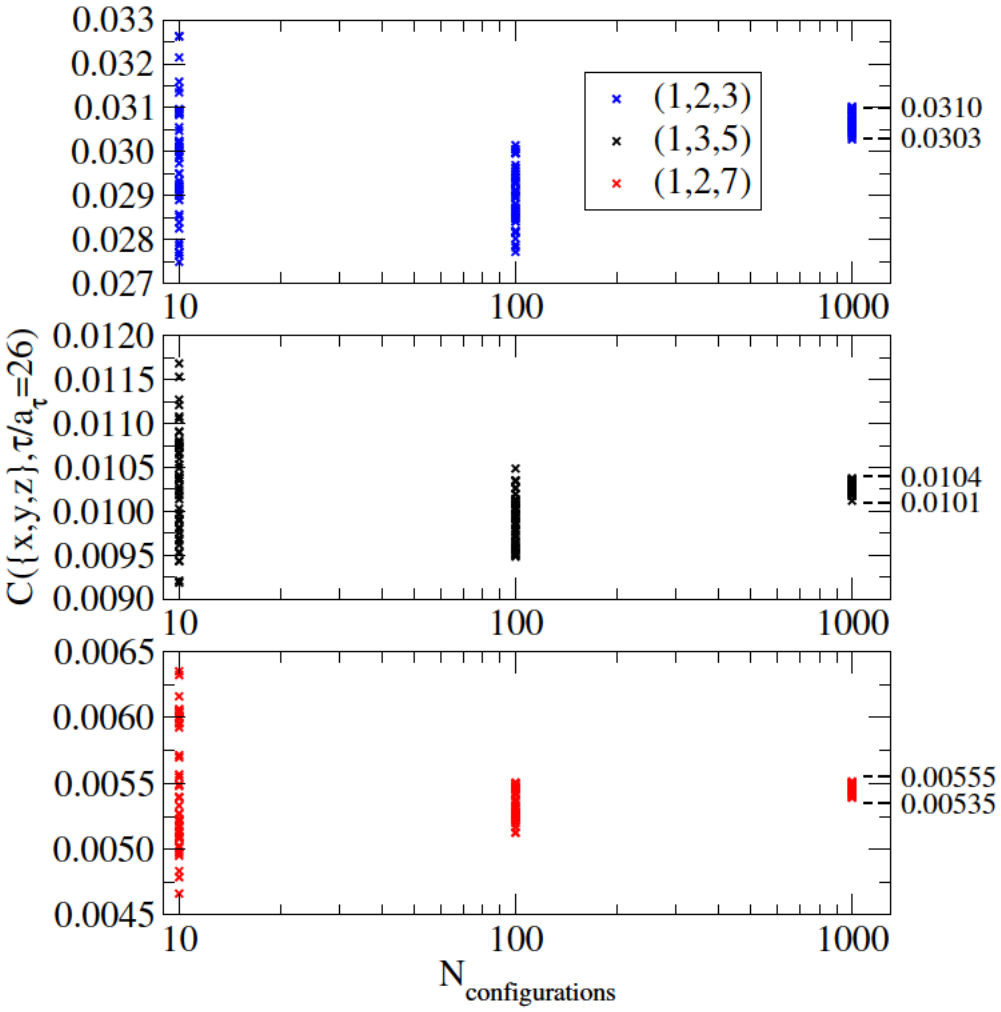

Figure 6.10: The correlator evaluated at three representative distances, depicted by colour, against the number of configurations included in the correlator calculation. Within each spread of points is the correlator evaluated at every point related to the representative point, (x, y, z), by cubic transformations. This tests the quality of this symmetry that should be exact in the limit of infinite statistics.

Any difference between points of different symbols is attributed to the breaking of the continuous rotational symmetry introduced by the finite lattice spacing. Take, for example, the value of the correlator at $(x, y, z) = (3, 0, 0), (0, 3, 0)$, and $(0, 0, 3)$, these are approximately the same as each other, yet very different from $(x, y, z) = (2, 2, 1), (2, 1, 2)$, and $(1, 2, 2)$. These discretisation errors become less apparent at larger distances as the ratio of $(x + y + z)/\sqrt{x^2 + y^2 + z^2}$ (which is the ratio of the distance in discrete space against the polar distance) approaches $\sqrt{3}$, and this is shown clearly in Figure 6.11. Given that we expect this symmetry breaking to be largest when $(x + y + z)/\sqrt{x^2 + y^2 + z^2}$ is furthest from $\sqrt{3}$, we can say that this is mostly a short distance effect.

6.3.3 Tree-level improvement

The short distance discretisation errors shown in the previous subsection are not unique to the calculation of correlators, they are an inherent lattice artefact. We can build upon this by contrasting the perturbative lattice calculation of the static energy with its known continuum counterpart to compute a correction that will also apply to our data [117, 118]. This correction procedure is called tree-level improvement.

In this perturbative expansion, we consider that the leading contribution to the static energy is the one gluon exchange and we do not include a running coupling. The constant coupling will be denoted $\bar{\alpha}_s$. The lattice calculation of the free energy takes the form

$$E^{\text{lat}}_{\text{free}}(r) = \bar{\alpha}_s \frac{4\pi}{a_s} \int_{-\pi}^{\pi} \frac{d^3q}{(2\pi)^3} \frac{e^{i\mathbf{q}\cdot\mathbf{r}}}{4\sum_i (\sin^2(\frac{q_i a_s}{2}) + \frac{1}{3}\sin^4(\frac{q_i a_s}{2}))}, \tag{6.13}$$

where q_i are dimensionless lattice momenta[1]. The continuum counterpart is

$$E^{\text{cont}}_{\text{free}}(r) = \frac{\bar{\alpha}_s}{r}. \tag{6.14}$$

The difference between these two quantities is exploited by [117] as an estimation of the lattice discretisation errors in the potential. Ignoring, for the moment, $\bar{\alpha}_s$, the difference reads

$$\delta G(r) = \frac{4\pi}{a_s} \left(\int_{-\pi}^{\pi} \frac{d^3q}{(2\pi)^3} \frac{e^{i\mathbf{q}\cdot\mathbf{r}}}{4\sum_i (\sin^2(\frac{q_i}{2}) + \frac{1}{3}\sin^4(\frac{q_i}{2}))} \right) - \frac{1}{r}, \tag{6.15}$$

and is included in the Cornell potential via

$$V(r) = -\frac{\alpha}{r} + \sigma r + C + \alpha f \delta G(r). \tag{6.16}$$

[1]This equation is reduced to a discrete Fourier transform when calculated on a finite lattice of size $(a_s L)^3$, thus $q_i = 2\pi n_i/L$ for $n_i = -L/2 + 1, -L/2 + 2, ..., L/2$.

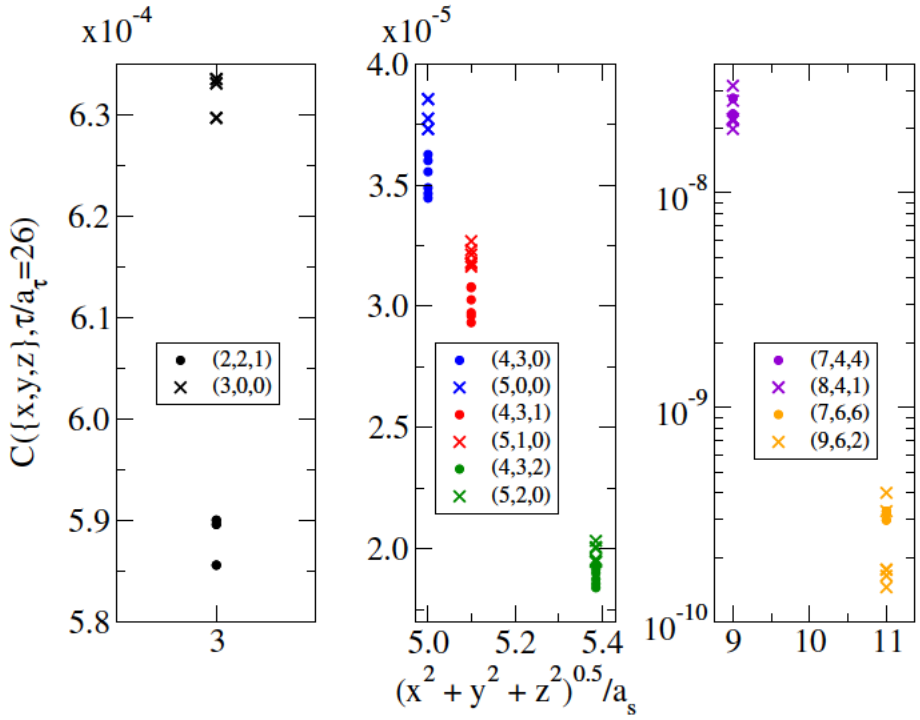

Figure 6.11: The correlator at different radial separations, given by the colour. For each colour there are two sets of points, dots and crosses, that correspond to two sets of x, y, z that are not degenerate under the symmetries of the cubic group but are degenerate under continuous rotations. There are also multiple points for a given colour and symbol, these are the values of the correlator at points that are degenerate under the cubic group and continuous rotations. Therefore, contrasting the difference between points of the same colour and symbol, against those of the same colour but different symbol gives an indication of continuous rotational symmetry breaking relative to the approximately conserved cubic group symmetries.

Here we have turned the strong coupling constant, $\bar{\alpha}_s$, into a free parameter, α, and we have also introduced another free parameter, f, to control the size of the correction contributions. This inclusion of δG into the Cornell ansatz is added to correct, at leading order, for the systematics of finite lattice spacing. This method will be referred to as *improvement scheme* ***I***.

Alternatively, [118] equates the lattice and continuum free energies to define so-called *improved distances*, r_I, through

$$\frac{a_s}{r_I} = \int_{-\pi}^{\pi} \frac{d^3q}{(2\pi)^3} \frac{e^{i\mathbf{q}\cdot\mathbf{r}}}{4\sum_i (\sin^2(\frac{q_i}{2}) + \frac{1}{3}\sin^4(\frac{q_i}{2}))}. \tag{6.17}$$

In this form, r_I/a_s is in lattice units. Equation (6.17) gives a mapping from x, y, z input into the right-hand-side (inside $\mathbf{r}$) to the improved distance r_I on the left. One key difference is that this approach does not require a free parameter to be fit to the data, there is a unique shift from $\mathbf{r} = (x, y, z) \to r_I$. Defining the data at r_I, rather than r, accounts, at leading order, for the errors introduced by the finite lattice spacing. We will refer to this method as *improvement scheme* ***II***.

Both improvement schemes require a calculation of the free energy on the lattice. As we are concerned with ultra-violet (UV) effects (the short distance, finite lattice spacing corrections) we would like to calculate this in the thermodynamic limit ($N_s \to \infty$). Another justification for this limit mimics [119, 120] whereby the lattice calculation only equates to the continuum in the thermodynamic and continuum limits, and therefore in the thermodynamic, but not continuum, limit we would expect only finite lattice spacing effects present. These are the effects we are trying to correct for.

One problem with computing equation (6.13) is the pole at $\mathbf{q} = \mathbf{0}$. For a similar calculation in $SU(2)$ pure gauge theory the author sets the value of the integrand at $\mathbf{q} = \mathbf{0}$ to zero [121]. We can check this prescription by considering that as equation (6.13) is a Fourier transform then the $\mathbf{q} = \mathbf{0}$ term only offers an additive renormalisation. To clarify this, consider that as the continuous integral in equation (6.13) becomes a discrete sum due to discretised momenta, $E^{\text{lat}}_{\text{free}}(r)$ is calculated via a DFT. The zero momentum term in a DFT is multiplied by $e^{\mathbf{0}\cdot\mathbf{r}}$ and thus is a constant over $\mathbf{r}$, impacting the total result only by means of a constant additive shift. All that remains is to establish the value of this additive shift, and as the large r behaviour of each method is known, we can use this to confirm that setting this term to zero gives the appropriate behaviour for the renormalisation.

Infinite volume extrapolations

To extrapolate $\delta G(r)$ and r_I, from equations (6.15) and (6.17) respectively, to the thermodynamic limit they are computed on lattices of differing sizes and then

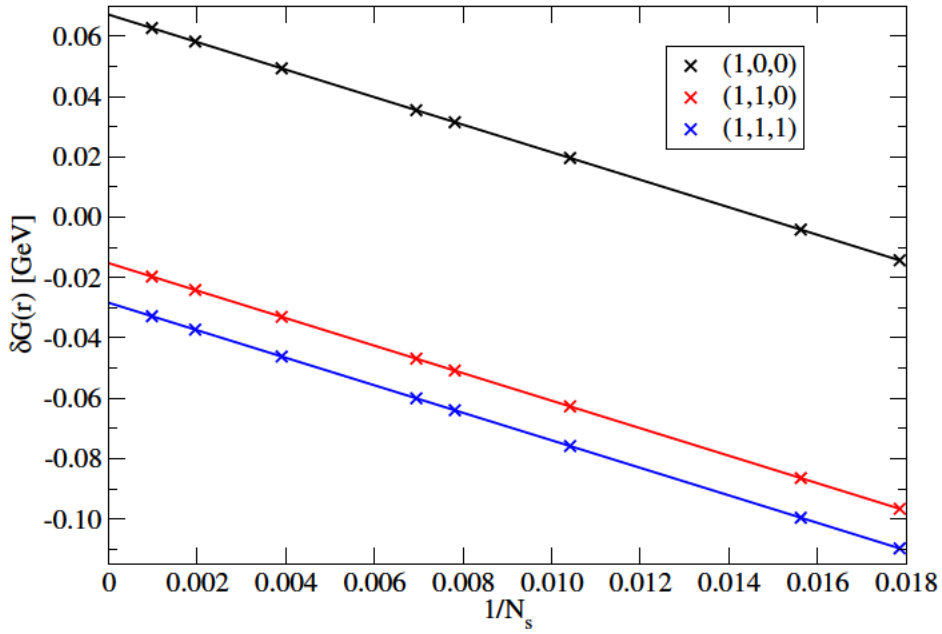

Figure 6.12: The infinite lattice extrapolations of the correction term in the ansatz for improvement scheme **I**, given by equation (6.15). The ansatz is plotted for the shortest three non-zero separations on the lattice.

their values are linearly extrapolated against $1/N_s$, with the thermodynamic limit being $1/N_s \to 0$. The lattice sizes used here are $N_s = 56$, 64, 96, 128, 144, 256, 512, and 1024, with the largest size limited by computational resources.

Considering improvement scheme **I**, the extrapolation of $\delta G(r)$ at the shortest three distances, $\mathbf{r}/a_s = (1,0,0), (1,1,0)$, and $(1,1,1)$, is shown in Figure 6.12. Each datum in this figure is from a single lattice calculation and does not contain error estimates. A linear fit interpolates well between the full range of data with a χ^2_ν, the goodness-of-fit per degree of freedom statistic, of 10^{-7}, this is excellent evidence that the extrapolation carries some significance.

Figure 6.13 depicts the ansatz projected into polar coordinates, this coordinate change is purely for visualisation purposes. It shows significant corrections to small distances and negligible effects beyond $r/a_s = 6$, with the sign of the correction, and the magnitude, changing with distance. Keeping the underlying ansatz in Cartesian coordinates allows for different corrections to pairs at the same polar distance, like $(3,0,0)$ and $(2,2,1)$, evidenced in the multivalued nature at

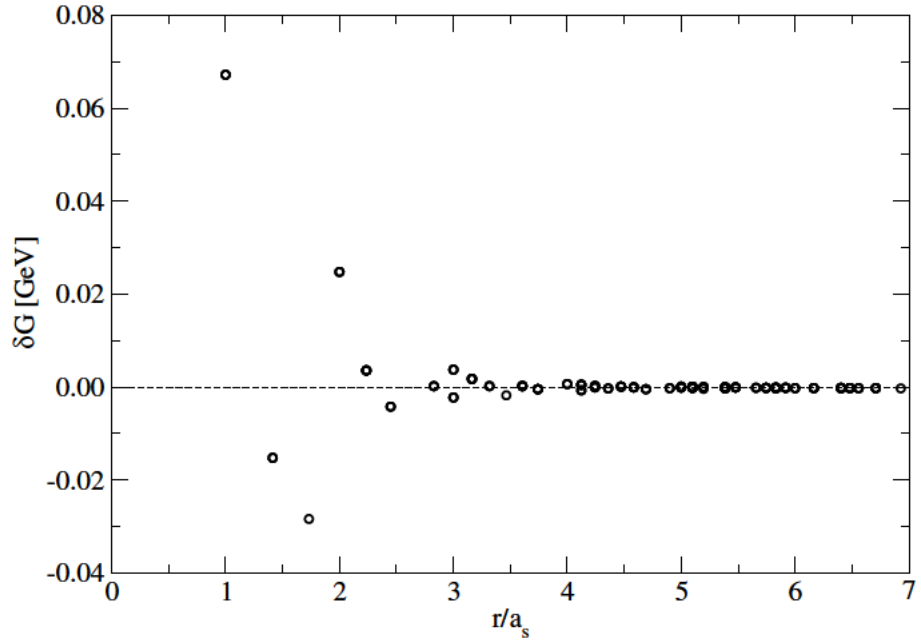

Figure 6.13: The extrapolated values of the tree-level improved correction ansatz from equation (6.15). This quantity is calculated in the full x, y, z Cartesian space and then projected along the polar coordinate, r, hence the multivalued nature at, for example, $r/a_s = 3$. The dashed line at $\delta G = 0$ is the expected large distance behaviour.

$r/a_s = 3$ in this figure.

Turning to the improvement scheme **II**, the expectation for the improved distance calculation is that for large separations r_I should approach r, this is because we expect to only correct for short distance effects. Whilst the linear fit to the improved distances as a function of lattice size from $N_s = 56 - 1024$ yields $\chi^2_\nu = 10^{-4}$, it also gives values of r_I that do not align with r at large r. To remedy this we chose to change the range of data included in the extrapolation; the largest lattices are the most representative of infinite volume and so we only extrapolated over $N_s = 144$, 256, 512, and 1024. Figure 6.14 shows this extrapolation for the improved distances of the first three non-zero distances. This extrapolation over fewer lattice sizes leads to an extrapolated $r_I(r)$ that corrects only at short distances and tends towards $r_I(r) = r$ at around $r/a_s = 4$, this is depicted in Figure 6.15. It too results in a χ^2_ν of 10^{-7}.

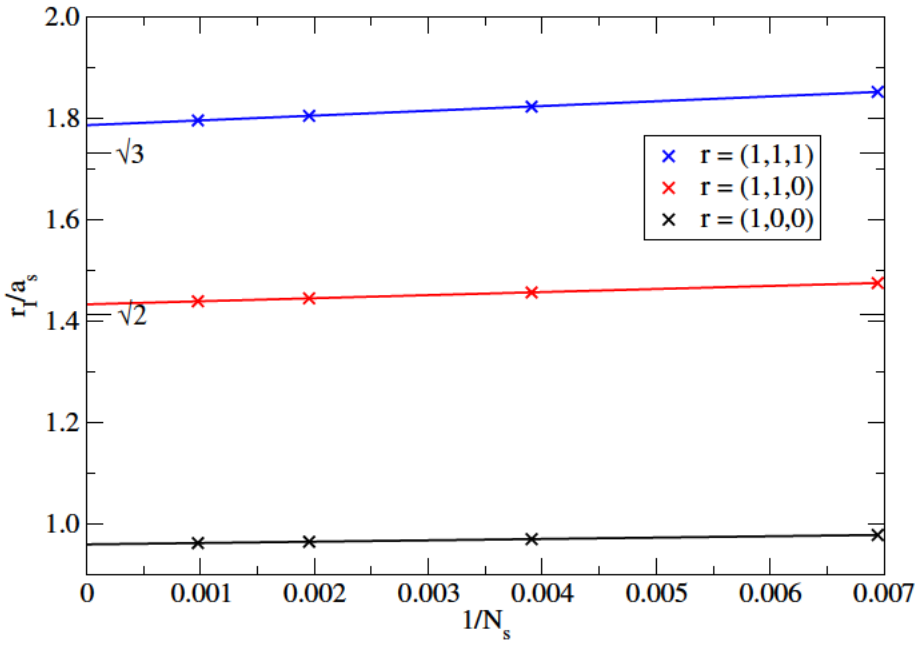

Figure 6.14: The first three non-zero distance extrapolations of the improved distances, r_I, from equation (6.17). This follows improvement scheme **II**. Highlighted are the polar distances for comparison with (1,1,0) and (1,1,1).

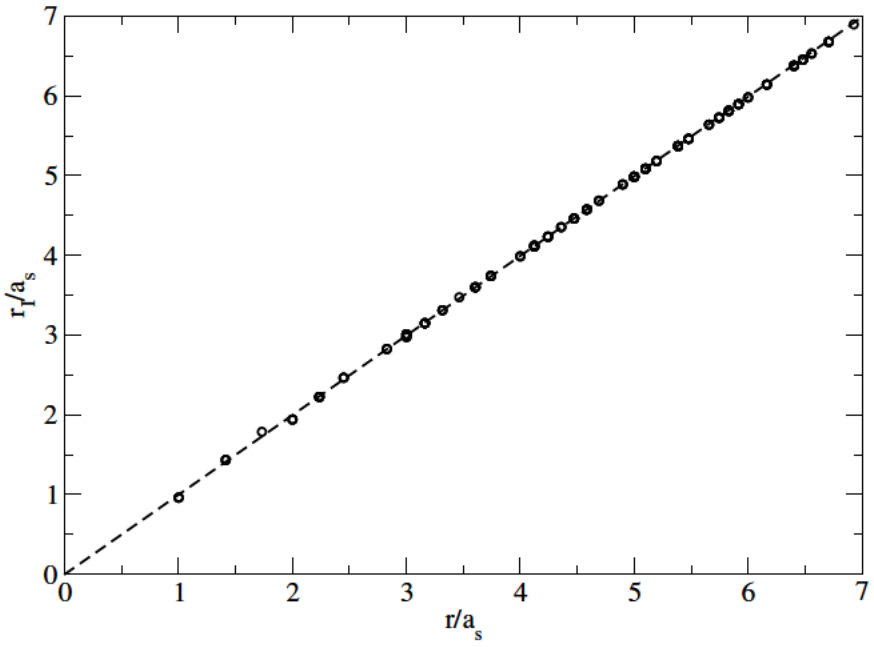

Figure 6.15: The extrapolated values of the tree-level improved distances from equation (6.17). This quantity is calculated in the full x, y, z Cartesian space and then projected along the polar coordinate, r, hence the multivalued nature at, for example, $r/a_s = 3$. The dashed line along $r = r_I$ is the expected large distance behaviour.

We will apply each of these corrections separately in Section 6.6.3 to assess their ability to correct for discretisation errors.

6.4 Importance of μ

The first use of the HAL QCD method was in the domain of nuclear physics [92]. In this setting, the reduced mass, μ, that enters into the Schrödinger equation is that of a baryon and thus precision particle collider measurements can be used as inputs. For the interquark potential of bottomonium, the reduced mass refers to the bottom quark, and colour confinement prohibits a simple attribution of a number to the mass of the bottom quark. Nevertheless, as stated in Section 5.2, we must provide a value as input.

In early work from the HAL QCD collaboration and others, the reduced charm quark mass was set to one quarter of the vector meson mass (J/ψ for their work on charmonium) [96, 101]. Later works argued that the quark mass can be determined by asserting that the spin-dependent potential, defined as

$$V_S(r) = V_{\mathrm{V}}(r) - V_{\mathrm{PS}}(r) \tag{6.18}$$

should vanish at large distance [97–100]. They therefore claim that

$$m_q = \lim_{r\to\infty} \frac{-1}{E_{hyp}} \left(\frac{\nabla^2 C_{\mathrm{V}}(\mathbf{r},\tau)}{C_{\mathrm{V}}(\mathbf{r},\tau)} - \frac{\nabla^2 C_{\mathrm{PS}}(\mathbf{r},\tau)}{C_{\mathrm{PS}}(\mathbf{r},\tau)} \right), \tag{6.19}$$

where, for a system of two equal mass quarks, $m_q = 2\mu$. Here the hyperfine splitting, $E_{hyp} = E_{\mathrm{V}} - E_{\mathrm{PS}}$, can be measured using hadron spectroscopy. This self-determination of the quark mass is proposed alongside, and to be used for, the time-dependent HAL QCD approach, however, the appearance of the energy is very much in the language of the time-independent approach. Taking the formalism of equation (5.8) one would instead get

$$m_q = \lim_{r\to\infty} \frac{1}{\dfrac{\partial C_{\mathrm{V}}(\mathbf{r},\tau)/\partial\tau}{C_{\mathrm{V}}(\mathbf{r},\tau)} - \dfrac{\partial C_{\mathrm{PS}}(\mathbf{r},\tau)/\partial\tau}{C_{\mathrm{PS}}(\mathbf{r},\tau)}} \left(\frac{\nabla^2 C_{\mathrm{V}}(\mathbf{r},\tau)}{C_{\mathrm{V}}(\mathbf{r},\tau)} - \frac{\nabla^2 C_{\mathrm{PS}}(\mathbf{r},\tau)}{C_{\mathrm{PS}}(\mathbf{r},\tau)} \right). \tag{6.20}$$

This is made more clear by considering that, in the presence of only a single state, j, and using the vector channel as an example,

$$\frac{\partial C_{\mathrm{V},j}(\mathbf{r},\tau)/\partial\tau}{C_{\mathrm{V},j}(\mathbf{r},\tau)} = \frac{-E_{\mathrm{V},j}\Psi_{\mathrm{V},j}(r)e^{-E_{\mathrm{V},j}\tau}}{\Psi_{\mathrm{V},j}(r)e^{-E_{\mathrm{V},j}\tau}} = -E_{\mathrm{V},j}, \tag{6.21}$$

but this is certainly not the case in the time-dependent approach where the correlator is considered as a linear combination of states. Figure 6.16 shows

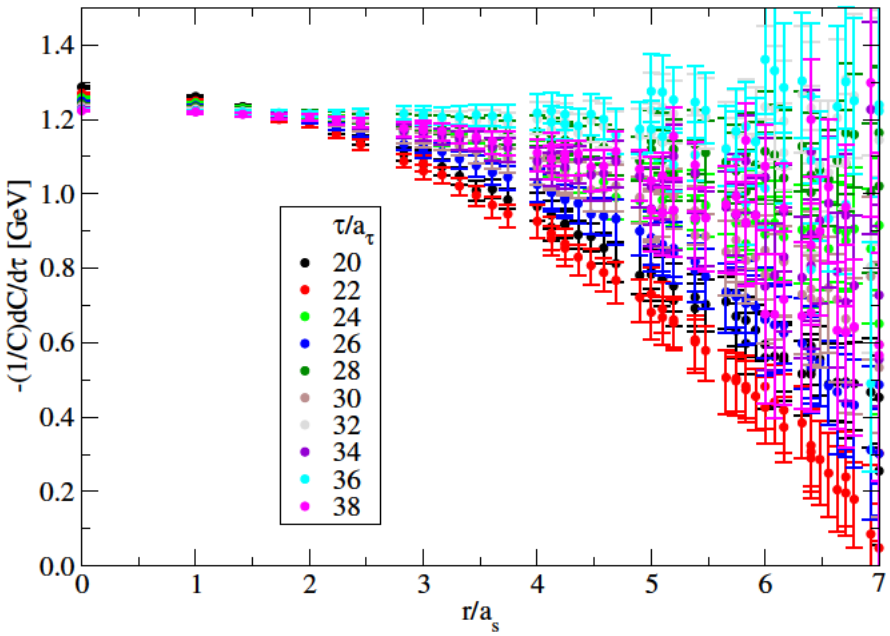

Figure 6.16: The dependence of the reduced temporal derivative term in the potential on distance, r, for the $T = 141$ MeV vector channel correlator.

$-(1/C)dC/d\tau$ against r for a range of τ. There is clear dependence on r and thus replacing this term with E_{hyp} for all r would not capture the true behaviour.

There are also considerations one must take due to the statistical uncertainties in each term in equation (6.20). Studies [97, 98] use quenched simulations and thus have small enough errors for a precise determination of μ this way, the full QCD calculation of [99, 100] also determines μ with this method but only at zero temperature. For the configurations of this study, which span many temperatures, the statistical fluctuations lead to a much larger error estimate and no such precise determination of μ using equation (6.20) can be made.

The role of μ in equation (5.8) is to balance the contributions from the reduced spatial and temporal derivatives terms. Examining them separately shows the importance of a precise determination of μ as it pertains to non-zero temperature studies and confinement signals. Figure 6.17 presents the dependence of the reduced spatial derivative term on τ and r. Comparing Figures 6.16 and 6.17, keeping in mind that the potential is a sum of these two quantities balanced by $1/(2\mu)$, one can see how there is an interplay at large r between the terms decreasing, or increasing slower, and the time: the time derivative term decreases more at early times, the spatial derivative term increases slower at late times. If one wants to ascertain the behaviour of the potential with increasing temperature, paying particular attention to the flattening at large distance, then one must be careful to disentangle physical effects from simply using an incorrect value of μ. Figure 6.18 depicts the effect of varying μ on the potential. At large distance and early times, an increase of μ by 25% causes significant flattening of the potential. There is also a difference at short distance for all times when μ is changed.

With the importance of the reduced quark mass established, and doubt cast upon the prescribed approach for calculating it, the following section will explore an alteration to the HAL QCD method that gives a self-consistent value of μ. This method accounts for the r dependence in the time and spatial derivatives and offers, simultaneously, a calculation of the potential and explicit checks of the validity of the Schrödinger equation formulation at each separation r.

We will come full circle in Section 6.6.2 by showing that this μ is still consistent with $\lim_{r\to\infty} V_{\mathrm{S}}(r) = 0$ and thus satisfies the condition of the HAL QCD approach.

6.5 Linear regression method

In Chapter 5 we implemented the original time-dependent HAL QCD approach, this assessed the validity of the equation for the potential, given in equation (5.8), by requiring that the potential was independent on τ. This method also required an external determination of the reduced quark mass, μ, which we have just raised issues with. In this section, we propose an alternative way to calculate

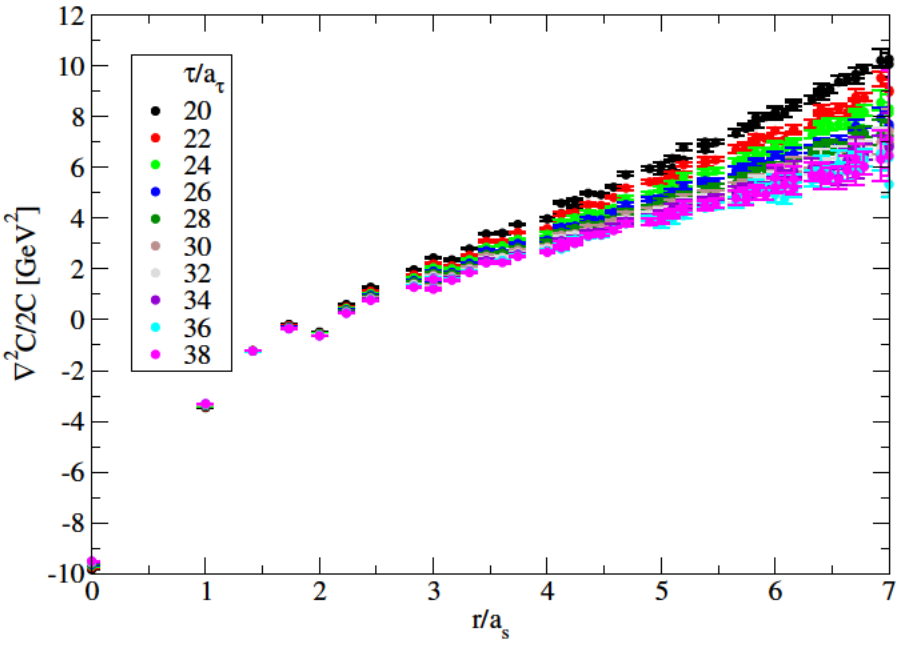

Figure 6.17: The dependence of the reduced spatial derivative term in the potential on distance, r. Clear discretisation errors are visible at short distance where this data deviate from a smooth function. The data shown is for the $T = 141$ MeV vector channel correlator.

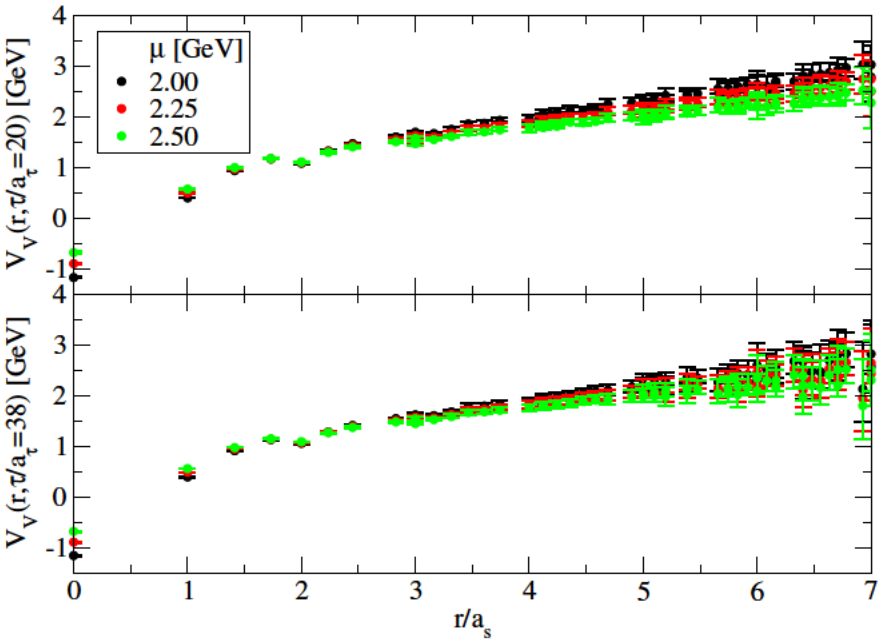

Figure 6.18: Illustrations of the vector potential for different reduced quark masses, μ. Created by the addition of Figures 6.16 and 6.17 in accordance with equation (5.8); this is not using the method developed in Section 6.5. Clearly, at early times, mistakenly estimating μ can mimic the flattening of the potential at large r. At all times there is a large difference at $r = 0$ with changing μ.

the potential that comes with a metric of how well the Schrödinger equation, and potential picture in general, is respected (important for non-zero temperature studies); it also comes with its own estimate of the reduced quark mass.

The approach of the previous chapter was to average values of the reduced temporal and spatial derivative terms over a time window and then combine them in equation (5.8). For this alteration we will expand and rearrange this equation slightly, giving

$$\frac{\partial C_\lambda(\mathbf{r},\tau)/\partial\tau}{C_\lambda(\mathbf{r},\tau)} = \frac{1}{2\mu}\frac{\nabla_r^2 C_\lambda(\mathbf{r},\tau)}{C_\lambda(\mathbf{r},\tau)} - V_\lambda(\mathbf{r}). \tag{6.22}$$

In this form it can be compared to the equation for a straight line: for fixed $\mathbf{r}$, a line in the plane of $(1/C_\lambda(\mathbf{r},\tau))\partial C_\lambda(\mathbf{r},\tau)/\partial\tau$ against $(1/C_\lambda(\mathbf{r},\tau))\nabla_r^2 C_\lambda(\mathbf{r},\tau)$ (with τ changing) would have gradient $1/(2\mu)$ and y-intercept of $-V_\lambda(\mathbf{r})$. Not only does this give us a prescription of the potential, but also the reduced quark mass. Furthermore, if the HAL QCD method is to hold, then the linear relationship explicit in equation (6.22) must also hold. So the extent to which these data fit to a straight line offers a validation of the whole HAL QCD method and potential picture, at least numerically.

Whilst this is written in a linear form, the two terms that depend on the correlator are functions of τ and $\mathbf{r}$, the potential is a function of $\mathbf{r}$, and the gradient has no explicit dependencies. Naively splitting equation (6.22) into a set of independent linear equations for each separation r_i in the set of all separations $\{\mathbf{r}\}$ would allow for the value of $V_\lambda(r_i)$ to be completely determined by linear regression (leading to $N_\mathbf{r}$ different two-parameter fits), however, it would also have the consequence of allowing μ to vary with distance. Conversely, trying to fit all τ and $\mathbf{r}$ at once would require fitting $N_\mathbf{r}+1$ parameters concurrently, a much more demanding minimisation. To keep μ fixed with $\mathbf{r}$ but without needing such a high dimensional minimisation, I perform the following steps:

1. Select a trial $\tilde{\mu}$. Using $\tilde{\mu} = m_\Upsilon/4$ is a reasonable value to start with.

2. For each r_i in $\{\mathbf{r}\}$, and $\tau \in [\tau_1, \tau_2]$, fit the y-intercept of a line, whose gradient fixed to be $1/(2\tilde{\mu})$, to equation (6.22). The choice of τ_1 and τ_2 will be explored below.

3. Combine the goodness-of-fit values from each fit of $V_\lambda(r_i)$. The fit metric chosen is the orthogonal residual distance which accounts for errors in both observables, see [122] for more details.

4. Steps $1-3$ constitute a goodness-of-fit algorithm that assesses the use of a single $\tilde{\mu}$ to recover $V_\lambda(\mathbf{r})$ whilst only ever performing one-dimensional fits, giving a $\chi^2(\tilde{\mu})$. One need only perform one more single-dimension optimisation to minimise $\chi^2(\tilde{\mu})$ and recover the optimal $\tilde{\mu}$. This also gives the

accompanying estimate of $V_\lambda(\mathbf{r})$. Note that without access to the gradient of $\chi^2(\tilde{\mu})$ we opted for the golden section search from [89].

Figure 6.19 shows the quality of the linear fits for five example values of $r = |\mathbf{r}|$ using the $T = 235$ MeV ensemble. These values of r were chosen to represent the set of all distances without reducing the clarity of the figure, many more analogous figures are shown in Appendix B to exhibit the quality of the fits at a range of temperatures. Plotted in the same colour is the reduced time derivative against the reduced spatial derivative (with 2μ not included in the reduced spatial derivative) at all different τ in the range dictated by Table 6.1. The different colours are data at different values of r. The horizontal and vertical error bars come from the statistical errors in the reduced time derivative and reduced spatial derivative terms respectively, which in turn come from bootstrap resampling the ensembles. The value of μ is fixed across r which is evidenced by the gradient being fixed between colours in Figure 6.19.

From Figure 6.19, alongside Appendix B, we can see that the linear relationship is very strongly respected with an orthogonal residual distance per degree of freedom of ~ 1. This value of orthogonal residual distance means that there is, on average, one average errorbar's length between each datum and the line of best fit. Therefore, by using the method introduced in this section, we have shown that the data respect the Schrödinger equation at non-zero temperature, even above T_{pc}. This is a development on the traditional HAL QCD method where this behaviour is assumed.

From Chapter 5 we could see that at the very earliest times there was still time-dependence in the potential. In the setting of these linear fits that corresponds to ranges of τ where the linear relationship is not upheld and we do not want to include these times in our analysis. These time ranges are easily distinguished in this regime as there is a goodness-of-fit parameter, the orthogonal residual distance.

However, like as Chapters 4 and 5, to make comparisons across temperatures we must be careful with time window systematics: certain effects are a result of only the time window changing and we want to remove these effects to make observations of physical effects. Table 6.1 shows the range of τ and r that can be analysed whilst maintaining orthogonal residual distance ~ 1, corresponding to times where the method is valid. Exactly as in Section 5.5 there will be multiple reports of the potential from a single temperature done in such a way that a comparison with an equal time window can be made.

By comparison with Table 5.1 one can see that a longer range of r and τ has been prescribed for the data in this chapter. We suggest that this is caused by a combination of factors: the estimation of the time windows is now done using a goodness-of-fit parameter rather than human assessment and therefore

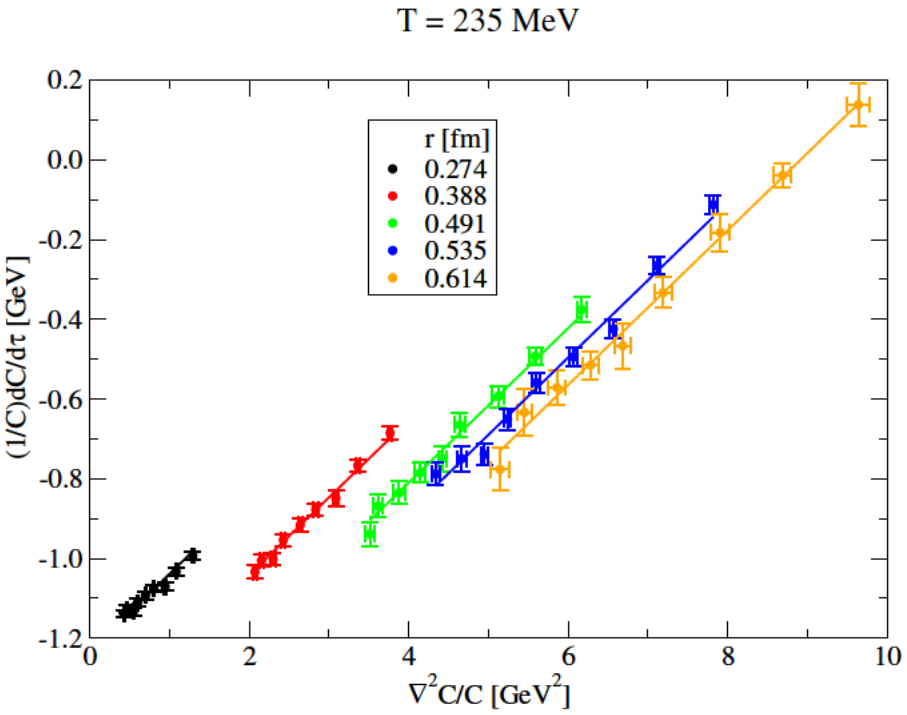

Figure 6.19: The linear fits that constitute the upholding of the Schrödinger equation given by equation (6.22). The markers are the data at a few representative distances in the vector channel, $T = 235$ MeV over the time range $\tau/a_\tau \in [13, 21]$. The gradient was fixed to $\mu = 2.58$ GeV for each linear fit, see Section 6.6.1 for more details on the treatment of μ across different temperatures. The full range of temperatures are shown in Appendix B.

Time window $[a_\tau]$	r max $[a_s]$	r max [fm]	Temperatures [MeV]
10 – 13	5.20	0.64	352 – 141
12 – 17	7.07	0.87	281 – 141
13 – 21	7.07	0.87	235 – 141
15 – 25	7.07	0.87	201 – 141
16 – 29	7.07	0.87	176 – 141
16 – 33	7.55	0.92	156 – 141
16 – 37	7.55	0.92	141

Table 6.1: The range of τ and r that minimised the orthogonal residual distance of a linear fit to equation (6.22) using the fitting procedure elucidated in Section 6.5. Unlike in Chapter 5, the $r = 0$ data are available due to incorporating periodic boundary conditions, therefore the minimum r is always 0.

is not prone to over/underestimation, the coarseness of the data from Table 5.1 meant that the exact cut off between valid and invalid data was not as clear and so there are larger rounding-like errors, and the off-axis data have smaller statistical fluctuations than the on-axis data because there are more degenerate combinations (under the cubic symmetry of the lattice) that can be made from points like (x, y, z) than from $(x, 0, 0)$. This final point needs the extra clarification that this goodness-of-fit parameter is measured over a range of r, rather than each value in turn, and thus any values of r that would be deemed invalid can be accounted for by neighbouring, valid, values of r such as off-axis points with smaller statistical variation. One further difference is that for these data it was found, empirically, that not including the final available point in time led to a better linear regression fit, this is why the time window ends at $\tau/a_\tau = N_\tau - 3$ (the lattice ends at $N_\tau - 1$, but the time derivative is only defined up to $N_\tau - 2$, so the penultimate point where the data are defined is $N_\tau - 3$).

6.6 Results

6.6.1 Temperature dependence of μ

We established that the potential is sensitive to the value of μ used for the analysis (Section 6.4). We have just now proposed a method that would determine μ from that data, which is good for self-consistency but does mean the value of μ may fluctuate with temperature. The quark mass itself is not a constant and runs with the energy scale considered and thus it is not unreasonable to assume that μ may change with temperature. It therefore remains to be seen if we can use a single value of μ for our analysis or if we must allow it to change with temperature.

Table 6.1 established the optimal time windows for drawing comparisons between the data, and thus there are two kinds of analysis that can be performed: once per temperature using the most appropriate time window for each temperature, or many times per temperature at many time windows. The goal of this subsection is to establish if μ changes significantly enough with temperature for us to need to include this effect in our analysis. It should be noted, however, that using a temperature dependent μ causes significant short range discrepancies between potentials at different temperatures, this was clear in Figure 6.18. Figure 6.20 shows the value of μ prescribed by the linear fits when the optimal time range for each individual temperature is used, therefore each data on this figure is fit to a different time range; overlaid is the line of best fit, complete with error estimate in grey, to estimate the behaviour of μ with temperature. The data from this figure is consistent with μ being constant with temperature when we consider the optimal time window for each temperature. This is evidenced by the

linear fit being indistinguishable from a constant within errors. A similar, albeit less concise, trend comes from the analysis across temperature multiple times for each time window. The gradient of a linear fit of $\mu(T)$ fluctuates between zero and slightly above zero (although still below a 2σ deviation from zero), and there seems no pattern between the time window and whether or not the gradient is zero. Therefore, there is not enough evidence to say that there is certainly temperature dependence of μ. For the rest of the analysis μ is kept fixed and is recovered from a constant fit of $\mu(T) = \mu$. For the vector channel, this is shown by the cyan line in Figure 6.20.

A success of this approach is that when the linear fits were applied to V_{PS} and V_V independently, the fitted values of μ from each channel agree remarkably, $\mu = 2.584(26)$ GeV and $\mu = 2.573(27)$ GeV respectively; for the remainder of the work the same value, $\mu = 2.58$ GeV, will be used for both channels. These correspond to a bottom quark mass, $m_b = 2\mu$, that is consistent with the zero temperature result from a similar study of NBS amplitudes using NRQCD quarks, $m_b = 5.52 \pm 0.33$ GeV [102] and the value of $m_b = 5.17$ GeV used for the original Cornell model work [31].

Another interesting result of Figure 6.20 is that the prescription that $\mu = m_\Upsilon/4 \sim 2.37$ GeV, extending the methodology of [96, 101] to bottomonium, does not seem to be supported by the data. This becomes more important in combination with Section 6.4 when it was shown that an incorrect value of μ could be incorrectly attributed to physical mechanisms, such as the flattening of the potential at large distance.

Equipped with the value of μ, we can alter the linear regression procedure presented in Section 6.5 such that the value of μ is fixed and yet we still fit a value of $V_\lambda(r_i)$ for a range of τ at each distance r_i. Potentials will be calculated for each row in Table 6.1 such that any comparison across temperatures can be made without systematic changes caused by different time windows for different temperatures.

6.6.2 Spin-dependent potential

Figure 6.21 shows the spin-dependent potential, defined in equation (6.18), against quark separation for a range of temperatures. The spin-dependent potential shows no significant change with the time window, Figure 6.21 therefore acts as a representation of all time windows.

As explained in Section 6.3.1, there are many cubic symmetry operations on the lattice and thus the data was averaged over these, what remains are the unique coordinates that cannot be transformed into any other coordinates by any of these symmetry operations. When these unique coordinates are converted into polar distance, ignoring any dependence on the angular polar coordinates,

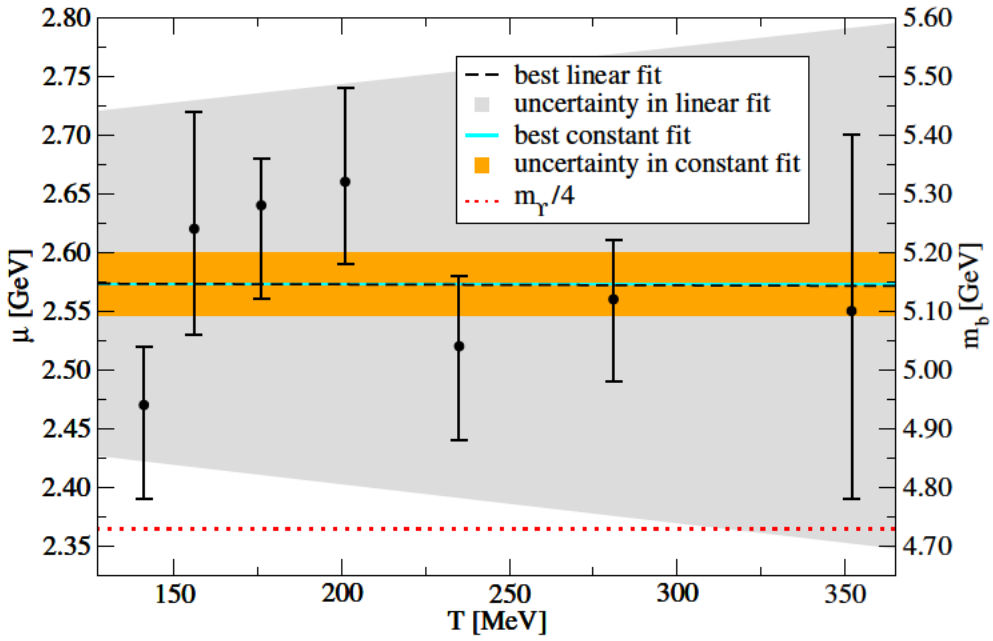

Figure 6.20: Estimated linear dependence of the reduced quark mass, μ, with temperature from the vector channel. The best estimate of a straight line fit is shown as the dashed black line with the uncertainty spanning the grey region. Clearly, the gradient of the linear fit is indistinguishable from zero within these errors. Fits to a constant value are shown in cyan with the uncertainty in orange. The errors on the points and linear fits were attained using bootstrap resampling. The heuristically motivated value of $m_\Upsilon/4$, analogous to that used by [96, 101], is shown by the red line. Note that for a system of two bottom quarks, $\mu = m_b/2$.

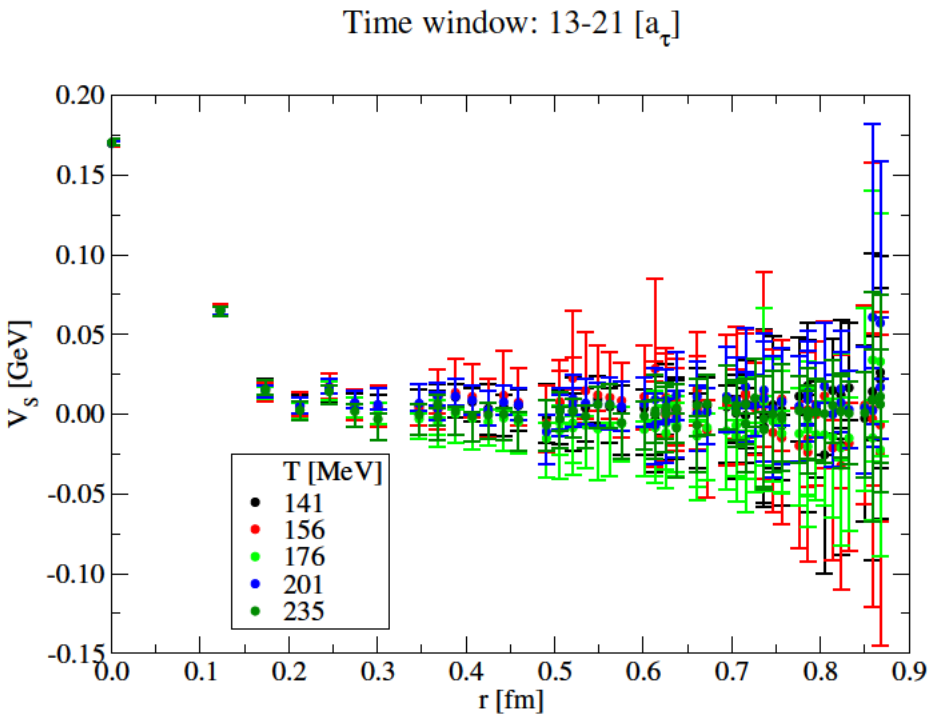

Figure 6.21: The spin-dependent potential, defined as $V_{\mathrm{S}} = V_{\mathrm{V}} - V_{\mathrm{PS}}$, for a range of temperatures at the fixed time window of $\tau/a_\tau \in [13, 21]$. Clearly, there is no discernable temperature dependence, and further analysis showed that there is no time window dependence either.

there are degeneracies, for example $(3,0,0)a_s$ and $(2,2,1)a_s$. These are the cause of the multivalued nature in the plots for the remainder of this section.

From Figure 6.21 it can be seen that the spin-dependent potential has a repulsive core and then plateaus to zero beyond ~ 0.2fm. There is also exceptional consistency across temperatures at short distances. The size of the errors at large r are an indication of why the behaviour of the spin-dependent potential could not be used to determine the reduced quark mass (discussed in Section 6.4).

In [98,100] the long distance behaviour of the spin-dependent potential is zero by construction: the value of μ was set according to this condition. In [97], a charmonium calculation, the assignment of $\mu = m_{J/\psi}/4$ was consistent with a zero spin-dependent potential beyond 0.5fm, however, in [101], another charmonium calculation with the same definition of μ, the spin-dependent potential plateaued at a negative value from 0.2fm onwards. This final result was calculated on the same gauge configurations as the work in this chapter and it would be interesting to rerun that analysis with the improvements introduced in this chapter.

The spin-dependent potential reported in this work is therefore consistent with the results of the HAL QCD collaboration.

6.6.3 Central potential

Figures 6.22 and 6.23 show the central potential for the first four time windows of Table 6.1. From Figures 6.22 and 6.23 it is clear that there is a systematic flattening of the potential with increased temperature, and that the effect is monotonic with differences often larger than statistical errors. Given that the same data are used multiple times, not every difference between temperatures is independent, but in each individual pane of the two figures all the data are independent.

Also present in these figures are significant discretisation errors, particularly at short distance. This is addressed below, using the results from Section 6.3.3.

Discretisation corrections

Whilst we don't know the exact form of the potential at increasing temperature, the zero temperature form is known to be well captured by the Cornell potential in the continuum and from lattice studies. With this in mind, we can say, with some confidence, that the potentials at short distance in Figures 6.22 and 6.23 are showing discretisation errors and a corrected version would increase smoothly. We stop short of defining this smoothness but we will observe the effects of discretisation corrections with this heuristic in mind. We can identify the 4^{th} and 5^{th} left-most points of Figures 6.22 and 6.23 as being from lattice sites $(1,1,1)a_s$ and $(2,0,0)a_s$ respectively: this pair of points differ greatly in discrete space but

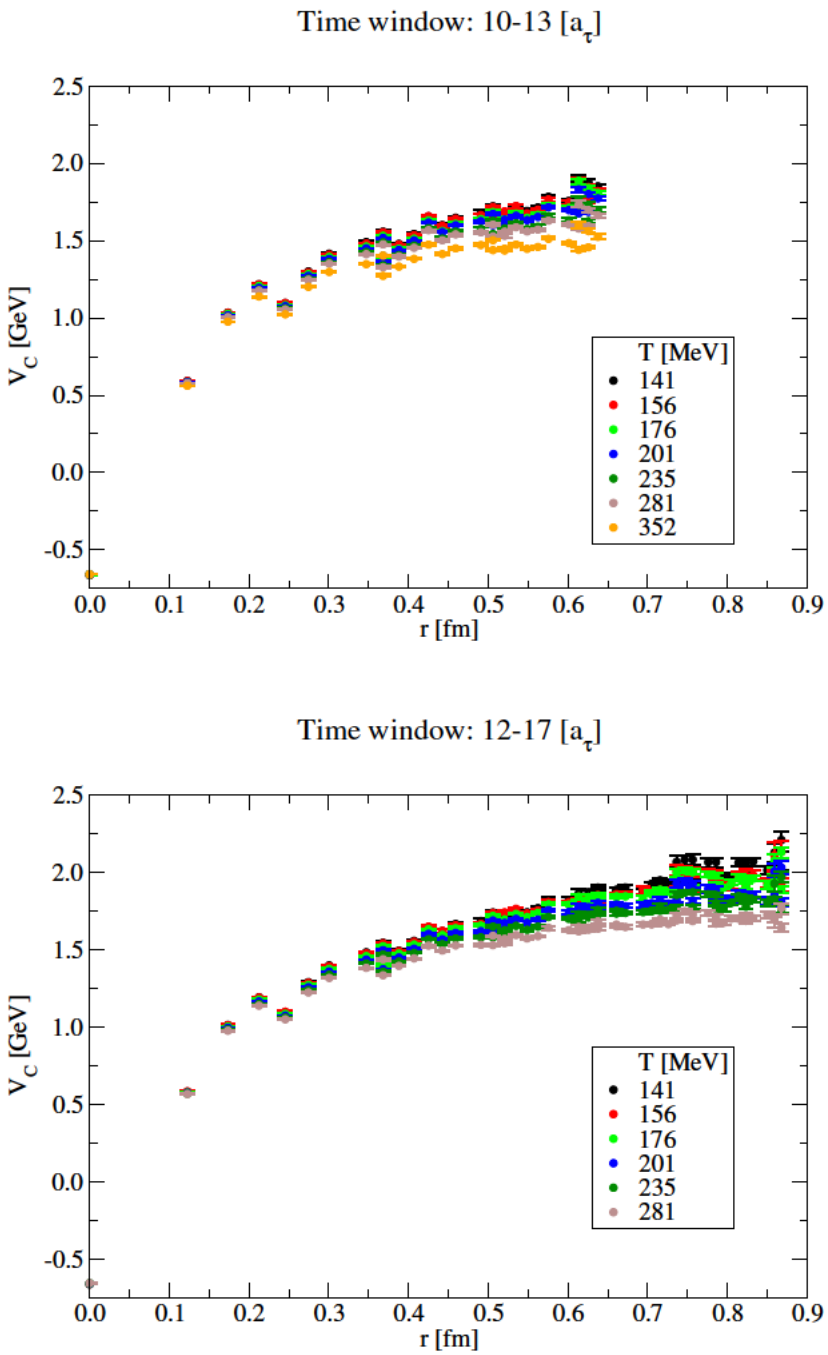

Figure 6.22: The central potential recovered from the linear regression fits given by equation (6.22) for the time windows given by the 1st (top) and 2nd (bottom) rows of Table 6.1. The data are plotted at the unique coordinates explained in Section 6.3.1 which are defined in Cartesian coordinates, when plotted against radial distance (ignoring the angular polar coordinates) there are some degenerate values. This explains the multivalued nature at, for example, $r \sim 0.38$fm.

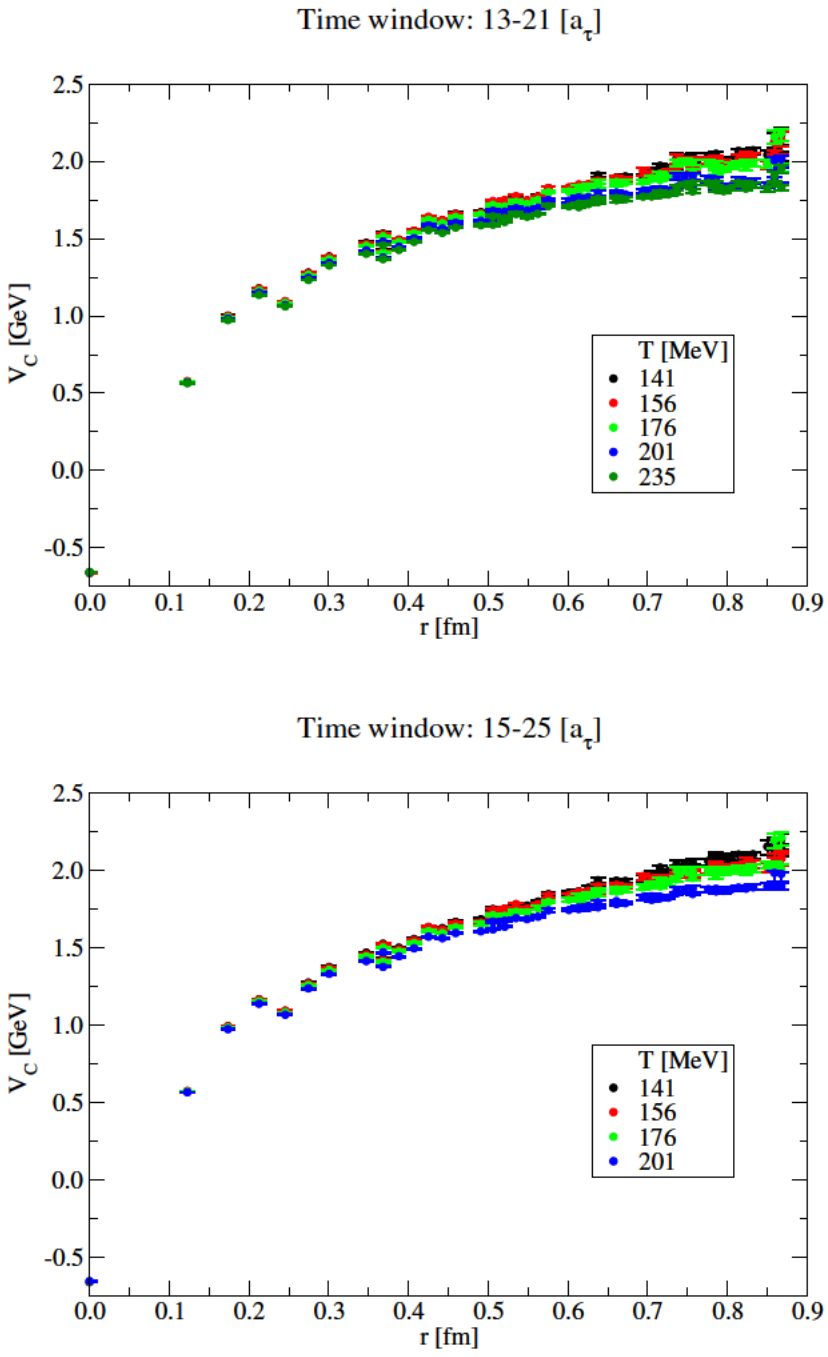

Figure 6.23: As in Figure 6.22 but for the 3rd (top) and 4th (bottom) rows of Table 6.1.

only slightly in continuous space, therefore, they act as a good guide for these discretisation corrections.

We have already outlined two approaches to correcting the discretisation errors present in the potential. In Section 6.3.3 we introduced improvement scheme **I** that gave an extra correction term to the Cornell potential ansatz, as well as improvement scheme **II** that leaves the values of the potential unchanged but changes the values of r over which they're defined. We will explore each method in that order.

Improvement scheme **I** requires us to fit the data to the Cornell potential. I will postpone reporting the values of the parameters until the next subsection and instead present only the impact of the tree-level improvement. To show the effects of this ansatz, the potential data is fit to the form of equation (6.16) and then the term responsible for the correction, $\alpha f \delta G(r)$, is removed from the data. The resulting potential is shown in Figure 6.24 for a single temperature, $T = 141$ MeV. The Coulomb-like increase at short distance is certainly less jagged, especially for the third and fourth left-most points, and the correction makes negligible change at larger distance. A fit of the $T = 141$ MeV data (over the time window $\tau \in [16 - 37]a_\tau$) to the corrected Cornell potential yields a χ^2_ν of 15, this is markedly lower than the value of 73 from the fit to the uncorrected version. Visually, too, it would seem like this is partially correcting for the discretisation, although it does not seem to correct discretisation errors completely. The latter point is clear as the correction does not offer enough change to overcome the continuous rotational symmetry breaking effects that are seen around $r = 0.38$fm in the figure, these are the two points at $(3, 0, 0)a_s$ and $(2, 2, 1)a_s$.

The second approach to discretisation corrections, improvement scheme **II**, was shown in equation (6.17). It gives a mapping from the Cartesian coordinate $\mathbf{r}$ to an improved distance r_I. This conversion contains no free parameter to adjust the strength of the correction and thus is less flexible than improvement scheme **I**, however, in Section 6.3.2 we noted that the naive conversion from Cartesian to polar coordinates was inappropriate on the lattice and thus this is well motivated. Figure 6.25 shows the effects of this method on the same data as Figure 6.24, but immediately apparent is the fact the improved distances do not change enough from the original distances to smoothen out the short distance jaggedness. Fitting the Cornell potential at the improved distances leads to $\chi^2_\nu = 37$, which is better than when fit to the polar distances where $\chi^2_\nu = 73$ but worse than the previous correction method. This is evidence that the method does offer partial corrections, however, given the lack of a free parameter there is no way to increase this correction beyond this level and thus we conclude that this method is not appropriate for our data.

Table 6.2 summarises the quality of fits from this section. We conclude by saying that improvement scheme **I** is more appropriate for these data and thus

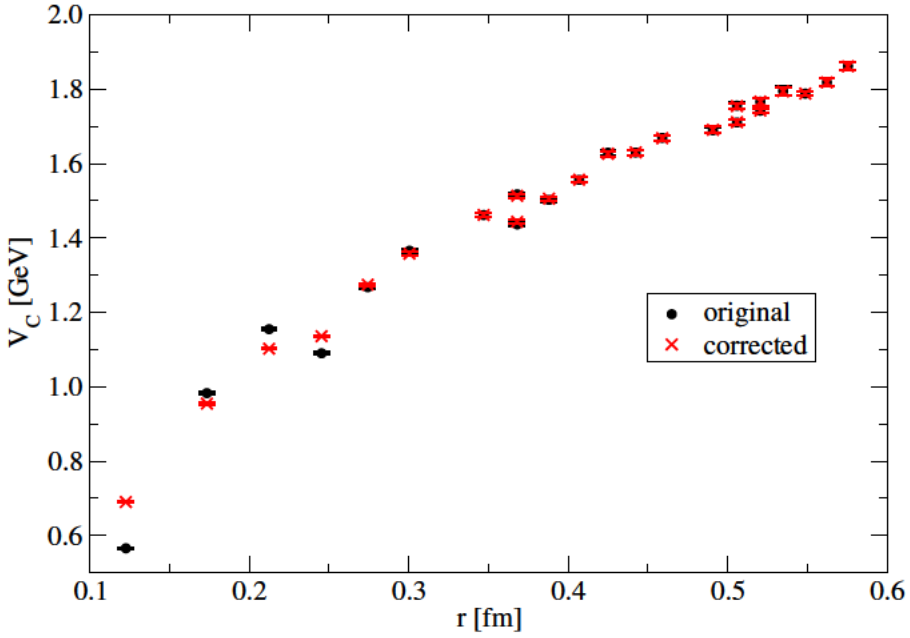

Figure 6.24: The central potential at $T = 141$ MeV for the time range $(16-37)a_\tau$ with (red) and without (black) tree-level improvements from improvement scheme **I** using, equation (6.16). Clearly the corrected version increases in a smoother fashion than the original but the corrections are not enough to overcome the continuous rotational symmetry breaking effects most present in the pair of points around $r = 0.38$fm.

Improvement scheme	χ^2_ν
Unimproved	73
Scheme **I**	15
Scheme **II**	37

Table 6.2: The quality of fits measured by the χ^2 per degree of freedom, χ^2_ν. See Section 6.3.3 for details of the improvement schemes.

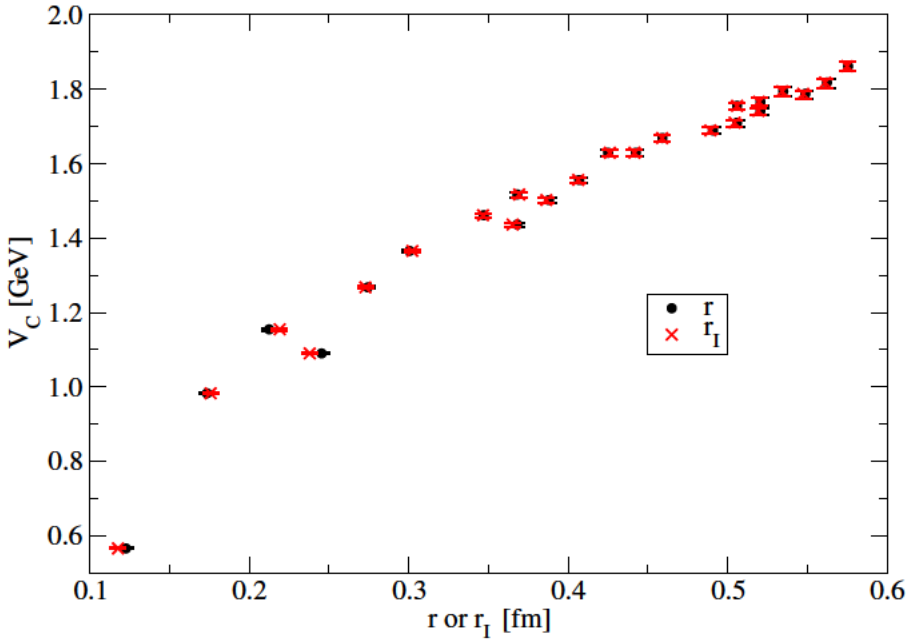

Figure 6.25: The central potential at $T = 141$ MeV for the time range $(16 - 37)a_\tau$ with (red) and without (black) tree-level improvements from improvement scheme **II**: these corrections shift the value of r at which the data are defined to an improved distance, r_I, through equation (6.17). The changes due to this correction are only small and as the mapping to r_I is unique there is no way to increase the effect.

this is the treatment that will be applied to the final analysis.

Fits to the Cornell potential

In order to quantify the changes to the potential with increased temperature, we compare the data to the Cornell potential to extract the coupling, α, and string tension, $\sqrt{\sigma}$. The behaviour of these two quantities with increasing temperature can offer insight into how the potential binding bottomonium states changes in the transition from hadrons to QGP.

There are four free parameters in the form of the Cornell potential that accounts for discretisation errors, equation (6.16). Two of these, the added vertical shift, C, and the magnitude of the corrections, f, are fixed using the lowest temperature data at the longest time window ($T = 141$ MeV over range $[16 - 37]a_\tau$) and thus only the coupling and string tension are measured for all other fits. The values are: $C = 1.26(2)$ GeV and $f = 4.08(48)$. Whilst C has changed from the value reported in the previous chapter, it is just an additive normalisation that is not of importance to this work. Figures 6.26 and 6.27 show the temperature dependence of the other two fit parameters, α and $\sqrt{\sigma}$ respectively.

By considering Figure 6.26 one can see that the dependence of the coupling, α, on temperature is not statistically significant. The reported values at different time windows almost always agree within errors and considering the time range that spans all temperatures ($[10 - 13]a_\tau$) there is no temperature change beyond the level of statistical errors. Comparing to the results of Chapter 5, specifically Figure 5.8 (top), we can see that the statistical errors and variation in α actually increase with the addition of the off-axis data. This is likely due to the short distance discretisation errors discussed in Section 6.6.3, as this is the region most sensitive to the value of α. This increase in uncertainty could be more representative as the fluctuations depicted in Figure 5.8 (top) could not be explained. The level of agreement between the two chapters is a testament to the tree-level corrections: the inclusion of off-axis data introduces discretisation errors not present in the on-axis data, however, the agreement suggests that these effects are, at least in part, accounted for. Further supporting this is that a fit of the potential at $T = 141$MeV to the Cornell potential that does not account for the discretisation errors gives $\alpha = 0.51(7)$. This value does agree with the results from Chapter 5, albeit with a significantly larger statistical error than when the corrections are used.

The string tension shows a significant and monotonic decrease with increasing temperature in Figure 6.27. There is reasonable agreement between different time ranges for the same temperature, with $T = 281$ MeV being the largest exception. That datum notwithstanding, there is certainly a pattern of decreasing string tension beyond the level of errors with increasing temperature when considering

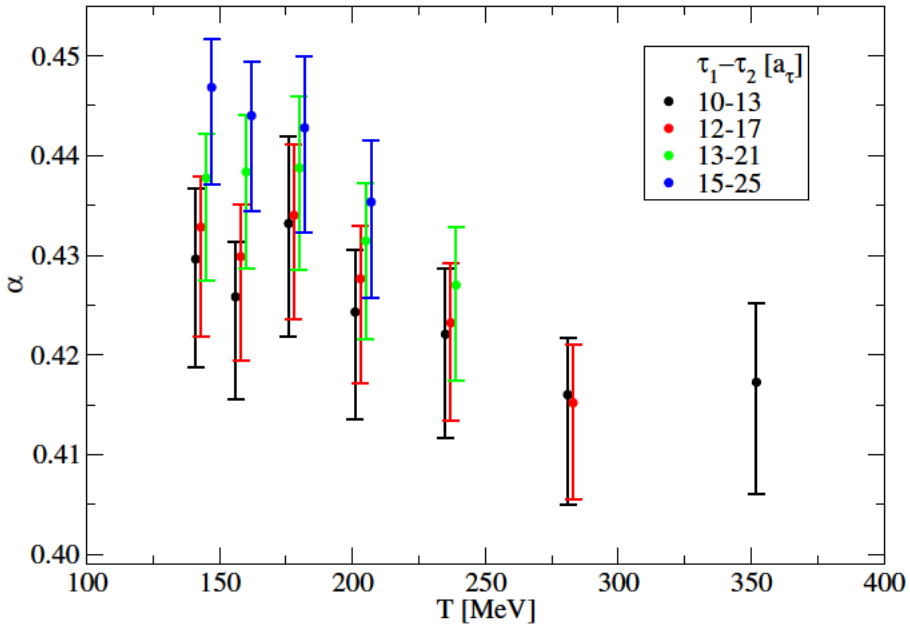

Figure 6.26: The fitted values of the coupling, α, from the tree-level correction inspired Cornell ansatz given in equation (6.16). Data of the same colour were fit to the same time range over various temperatures. The errorbars are from estimates on bootstrap resampled ensembles. The data have been shifted horizontally for clarity.

a fixed time window. This stands in qualitative agreement with the previous chapter, namely Figure 5.8 (bottom), albeit with a clearer behaviour with temperature. However, the values of the string tension are markedly lower and in line with $\sqrt{\sigma} = 445$ MeV from [28]. This reduction can be attributed either to the increased accuracy in the finite difference Laplacian explored in Section 6.2.1 or the more appropriate prescription of the quark mass. Whilst both chapters reported a decrease of string tension with increasing temperature, the results of this section are subject to a more thorough treatment and thus carry more weight.

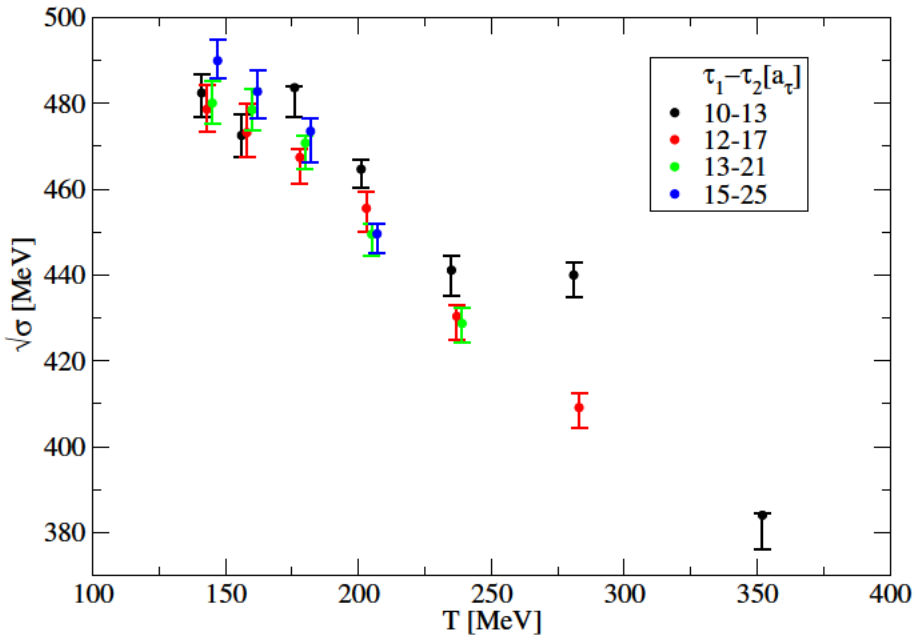

Figure 6.27: As in Figure 6.26 but for the string tension, $\sqrt{\sigma}$.

6.7 Conclusion of interquark potentials

The results of this chapter are more than the non-zero temperature analysis of Section 6.6. There are checks and developments to the HAL QCD method that also apply to zero temperature studies. In Section 6.2 we showed that increasing the accuracy of the finite difference derivative that approximates the Laplacian has a significant effect on the potential; when the resulting potential was fit to the Cornell ansatz in Section 6.6.3 this effect manifested in the reduction of the string tension towards physical values (when compared to the results of Chapter 5). We introduced a new formulation of the HAL QCD method in Section 6.5 that provided two new elements: a method of assessing how well the data respect the Schrödinger equation at non-zero temperature, and a self-consistent determination of the reduced quark mass. The first of these was present in Figure 6.19 where we saw how the non-relativistic Schrödinger equation is respected above T_{pc}, reflected in the quality of the linear relationship introduced by this new method. The second of these new elements brought into question the treatment of the reduced quark mass at non-zero temperature, whether it should remain fixed at different temperatures or be allowed to vary. In Section 6.6.1 we concluded that the data do not show significant indications in favour of varying across temperature and it was chosen to keep the mass fixed. Furthermore, the analysis of both the vector and pseudoscalar channels gave estimates of the quark mass that are consistent with each other within errors, moreover, the resulting quark mass agrees with [31, 102]. Establishing the reduced quark mass did not require the assertion that the spin-dependent potential vanishes at large distance, the fact that this result was shown to still be the case strongly supports the HAL QCD method. Finally, through fits of the Cornell potential to the central potential it was shown that the coupling exhibits no significant temperature dependence yet the string tension systematically, and significantly, decreases with increasing temperature. This is a reflection of the central potential flattening with increased temperature, which is in agreement with results from static quark calculations [103–108] (recent result from [109] notwithstanding) and charmonium interquark potentials from [101].

Chapter 7

Conclusion

In Chapter 4 we performed spectral reconstruction to extract the ground state mass and width of the Υ and χ_{b1} states. Care was taken to reduce, and then extrapolate out, the systematic dependencies on the time window over which the analysis was performed. The resulting narrative was that the mass does not change with temperature for either state and that the width increases for both. The increase was larger for the χ_{b1} suggesting that this would dissociate earlier than the Υ. The excited state values were not reported as they varied greatly due to statistical uncertainties. Further work could be done to develop a more robust spectrum ansatze, reducing the dependence on the time window, increasing the quality of the fits, and providing access to excited state information.

In Chapters 5 and 6 the central and spin-dependent potentials were calculated for the S-wave bottomonium states. Improvements made to the HAL QCD method confirmed that the non-relativistic Schrödinger equation is still respected above the pseudocritical temperature and that the quark mass used for this analysis does not change with temperature. The central potential flattens with increasing temperature and exhibits clear Cornell-like behaviour. The spin-dependent potential shows a repulsive core and then returns to zero beyond 0.2fm with temperature having no impact on the spin-dependent potential. Discretisation errors were reduced using tree-level improvement, however not eliminated. Performing the same analysis on lattices with smaller lattice spacing would reduce these errors and give a better estimation of the short distance behaviour of the potential.

Further work could explore agreement between the Υ mass recovered from spectral reconstruction and the spectrum of S-wave states calculated via the Schrödinger equation using the potential obtained from the HAL QCD method. This is beneficial as spectral reconstruction complements the HAL QCD method. The former offers a measurement of the width of states, whereas the latter does not contain this information; the HAL QCD method does not grant access to the imaginary part of the potential from which the width could be estimated.

Appendices

Appendix A

Simplifying the Gaussian integral

In Section 4.3.1 we used maximum likelihood estimation to fit three physically justified ansatze to the correlation functions calculated on the lattice. As part of this analysis, we motivated three functional forms of the spectral function that were given in equations (4.17), (4.18) and (4.19). To convert a spectral function into a correlation function, within the framework of NRQCD, one takes the Laplace transform of the spectral function, given by equation (4.6). However, a simplification was made when calculating the Laplace transformation of the two spectral functions that contained a Gaussian peak (equations (4.18) and (4.19)). This appendix will explore the simplification used and quantify the difference between the simplified and full treatments of the Gaussian integral.

The ansatze stated in Section 4.3.1, equations (4.21) and (4.22), are the result of this simplification.

A.1 Correlator ansatz

The correlation function in NRQCD is the Laplace transform of the spectral function. This integral is over the range of non-negative, real energies, $\omega \in [0, \infty]$. However, the Laplace transform results in a 'simpler form' of correlation function if one instead evaluates the integral over the range $\omega \in [-\infty, \infty]$. I will soon clarify what is meant by simpler form.

First, we consider the spectral function

$$\rho(\omega) = \frac{A\sqrt{2\pi}}{\Gamma} e^{-\tau\left(\frac{(\omega-M)^2}{2\Gamma^2}\right)}. \tag{A.1}$$

Then we consider the Laplace transform of this, but importantly with the range of integration extended to the range $\omega \in [-\infty, \infty]$, *i.e.*

$$C(\tau)_{\text{simplified}} = \int_{-\infty}^{\infty} \frac{A}{\Gamma\sqrt{2\pi}} e^{-\tau\left(\frac{(\omega-M)^2}{2\Gamma^2}\right)} d\omega. \tag{A.2}$$

We can evaluate this by completing the square to leave the form of the correlation function that we gave in equation (4.21),

$$C(\tau)_{\text{simplified}} = Ae^{-\tau\left(M - \frac{\Gamma^2\tau}{2}\right)}. \tag{A.3}$$

This form is considered simple as the logarithm of this correlator is a polynomial in τ and as such it is easy to fit curves that estimate M and Γ.

By splitting the integral over all real ω into two integrals, one over positive ω and the other over negative ω, we can relate the true Laplace transform to the simpler version that we have just calculated. And so,

$$\begin{aligned}\int_0^\infty \frac{A}{\Gamma\sqrt{2\pi}} e^{-\tau\left(\frac{(\omega-M)^2}{2\Gamma^2}\right)} d\omega &= \int_{-\infty}^\infty \frac{A}{\Gamma\sqrt{2\pi}} e^{-\tau\left(\frac{(\omega-M)^2}{2\Gamma^2}\right)} d\omega - \int_{-\infty}^0 \frac{A}{\Gamma\sqrt{2\pi}} e^{-\tau\left(\frac{(\omega-M)^2}{2\Gamma^2}\right)} d\omega, \\ &= Ae^{-\tau\left(M-\frac{\Gamma^2\tau}{2}\right)} - \frac{Ae^{-\tau\left(M-\frac{\Gamma^2\tau}{2}\right)}}{2}\left(1+\mathrm{Erf}\left(\frac{\Gamma\left(\tau-\frac{M}{\Gamma^2}\right)}{\sqrt{2}}\right)\right).\end{aligned} \tag{A.4}$$

The error function, $\mathrm{Erf}(z)$ is defined as

$$\mathrm{Erf}(z) = \frac{2}{\sqrt{\pi}} \int_0^z e^{-t^2} dt. \tag{A.5}$$

If we further define the complementary error function, $\mathrm{Erfc}(z) = 1 - \mathrm{Erf}(z)$, then we can write the true Laplace transform in terms of the simpler form times a correction factor,

$$\int_0^\infty \frac{A}{\Gamma\sqrt{2\pi}} e^{-\tau\left(\frac{(\omega-M)^2}{2\Gamma^2}\right)} d\omega := C(\tau)_{\text{true}} = C(\tau)_{\text{simplified}} \times \frac{1}{2}\mathrm{Erfc}\left(\frac{\Gamma\left(\tau-\frac{M}{\Gamma^2}\right)}{\sqrt{2}}\right). \tag{A.6}$$

In the rest of this this Appendix, we assess the viability of using just $C(\tau)_{\text{simplified}}$ as the ansatz and neglecting the correction factor.

From the general properties of $\mathrm{Erfc}(x)$, namely that

$$\mathrm{Erfc}(x) = \begin{cases} \sim 0 & \text{if } x > 0 \\ 1 & \text{x=0} \\ \sim 2 & \text{x} < 0 \end{cases} \tag{A.7}$$

we can say that if the argument is suitably smaller than 0 then the correction from $\frac{1}{2}\mathrm{Erfc}\left(\frac{\Gamma\left(\tau-\frac{M}{\Gamma^2}\right)}{\sqrt{2}}\right)$ is approximately 1. Therefore, as this is a multiplicative correction, if $M/\Gamma^2 > \tau$ then the correction is negligible. To see the impact this correction term has, Figure A.1 shows how much it deviates from 1 in the case where the values chosen for M and Γ were 10 GeV and 0.4 GeV respectively. These values lie roughly in line with the fits to the χ_{b1} (with the mass also being apparent from the effective mass in Figure 4.5), as well as similar to those reported by [83]. From this one can see that providing we don't consider the

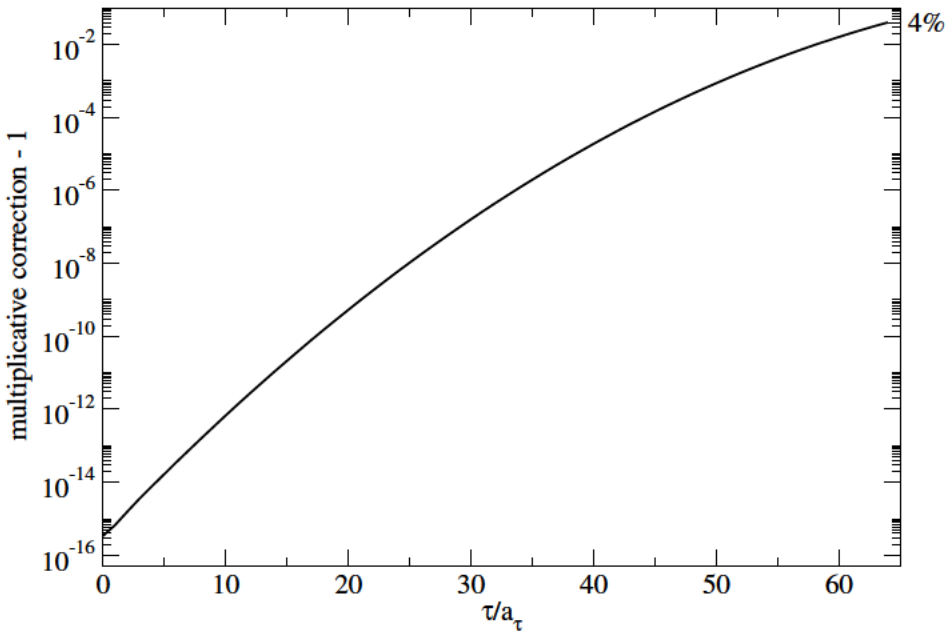

Figure A.1: There is a multiplicative correction that should be applied to the ansatze in equations (4.21) and (4.22) due to a simplification made when calculating the Laplace transform. Shown is the amount this multiplicative factor, given in equation (A.6), differs from 1 as τ increases. Rough estimates of the mass and width of the state were taken as examples, the values used were 10 GeV and 0.4 GeV respectively.

ansatz at times beyond $\tau/a_\tau = 64$ then the correction is only a maximum of 4%. The nature of the correction is negative spectral weight appearing in the integral now the lower limit of ω is $-\infty$ rather than 0. It allows for negative masses, or positive masses with such large widths that there is non-negligible negative spectral weight.

This inclusion of negative spectral weight is also why the effective mass appears not to be bound from below for a state with non-zero width. Taking the ansatz in the form $C(\tau) = Ae^{-\tau\left(M-\frac{\Gamma^2\tau}{2}\right)}$ and substituting this into the effective mass formula, $M_{\text{eff}}(\tau) = \log\left(\frac{C(\tau)}{C(\tau+1)}\right)$, gives $M_{\text{eff}}(\tau) = m - \Gamma^2(\tau + \frac{1}{2})$. No such simple expression exists for the effective mass when the correlator ansatz takes the corrected form of equation (A.6), but numerically it can be evaluated. Figure

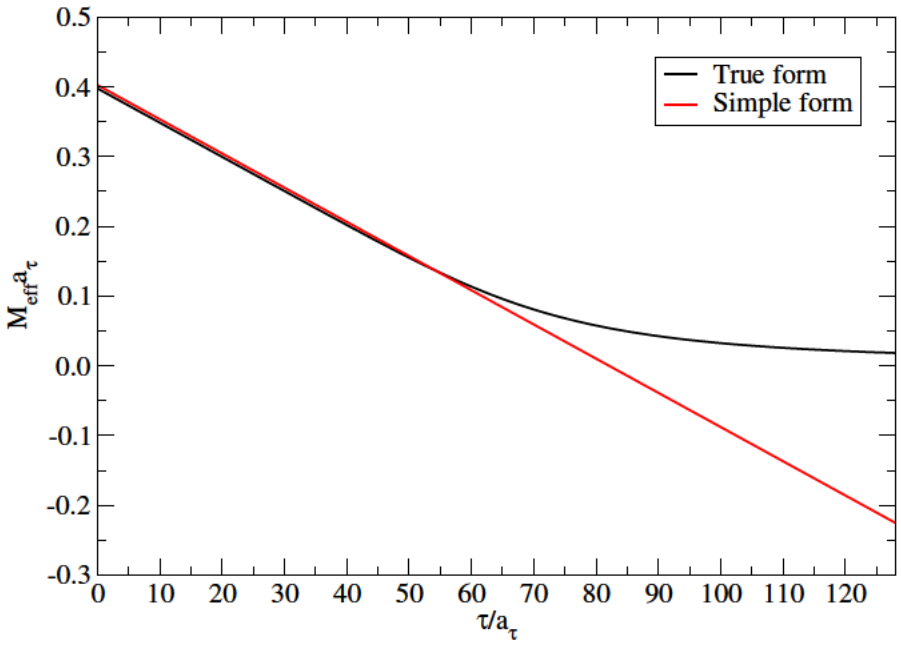

Figure A.2: The effective mass against time in the case where the spectral function is completely described by a single Gaussian, like in equation (4.18). The simple form (red) extends the range of integration for the Laplace transform to make for a simpler correlation function ansatz, whereas the true form (black) uses the correct bounds of integration, picking up a multiplicative correction to the simpler form that is shown in equation (A.6).

A.2 compares the two forms of the effective mass, the simpler form that extends the range of integration to $\omega = -\infty$, and the true form that contains the error function correction. Similar to Figure A.1, these used $M = 10$ GeV and $\Gamma = 0.4$ GeV as approximately physical parameters. From this, we conclude that a non-zero width does lead to a decrease of the effective mass below the ground state mass and that when the full expression is used this quantity is bounded from below at 0.

Appendix B

Linear fit approach to the HAL QCD method

B.1 Fits at all temperatures

In Section 6.5 we introduced a new approach to the HAL QCD method that treated the Schrödinger equation as a linear relationship captured in equation (6.22), repeated here for convenience

$$\frac{\partial C_\Lambda(\mathbf{r},\tau)/\partial\tau}{C_\Lambda(\mathbf{r},\tau)} = \frac{1}{2\mu}\frac{\nabla_r^2 C_\Lambda(\mathbf{r},\tau)}{C_\Lambda(\mathbf{r},\tau)} - V_\Lambda(\mathbf{r}). \tag{B.1}$$

In Figure 6.19 we showed how this linear relationship is upheld for a range of r at a single temperature, T=235 MeV. In this appendix, the analogous plots are shown for all temperatures of generation-2 ensembles, with the data from Figure 6.19 shown again here. The time ranges for each plot are given in Table 6.1. Multiple time ranges are shown for certain temperatures in this table, the data in the following plots are performed over the longest time window available for each temperature. For example, for T=176 MeV the time range is $(16-29)a_\tau$.

Figures B.1, B.2, B.3, and B.4 show the quality of the linear fits at decreasing temperature. As per Section 6.6.1 the gradient was fixed to correspond to $\mu = 2.58$ GeV for each fit at all temperatures, despite this restriction the data closely follow the linear relationship. This shows that the HAL QCD method, when treated in this method introduced in this work, can be applied at non-zero temperature, even above $T_{\rm pc}$.

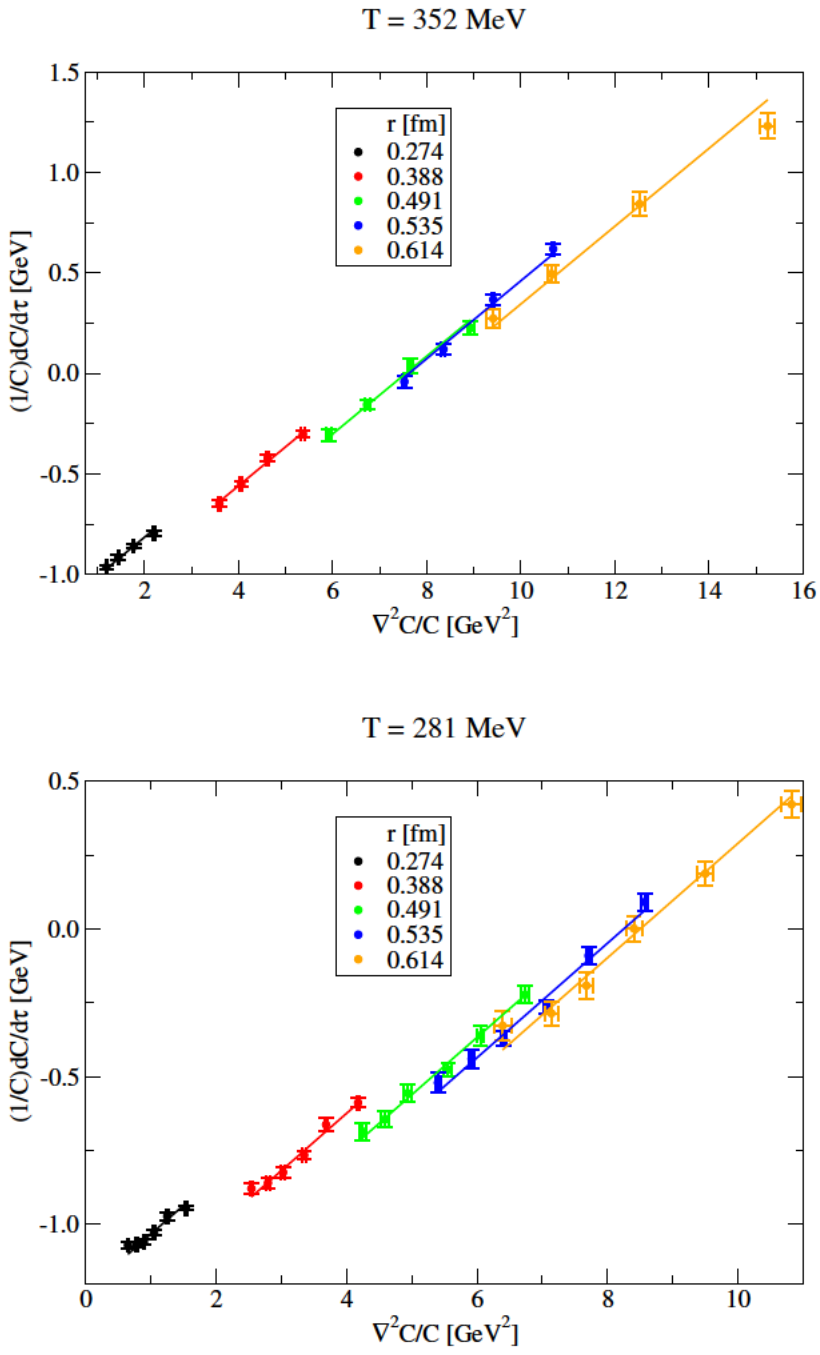

Figure B.1: The linear fits that constitute the upholding of the Schrödinger equation given by equation (6.22). The symbols are the data at a few representative distances in the vector channel for T= 352 MeV (top) and T= 281 MeV (bottom). The ranges of τ are reported in Table 6.1 (the longest time range for each temperature is used). The gradient was fixed to $\mu = 2.58$ GeV for each linear fit, see Section 6.6.1 for more details on the treatment of μ across different temperatures.

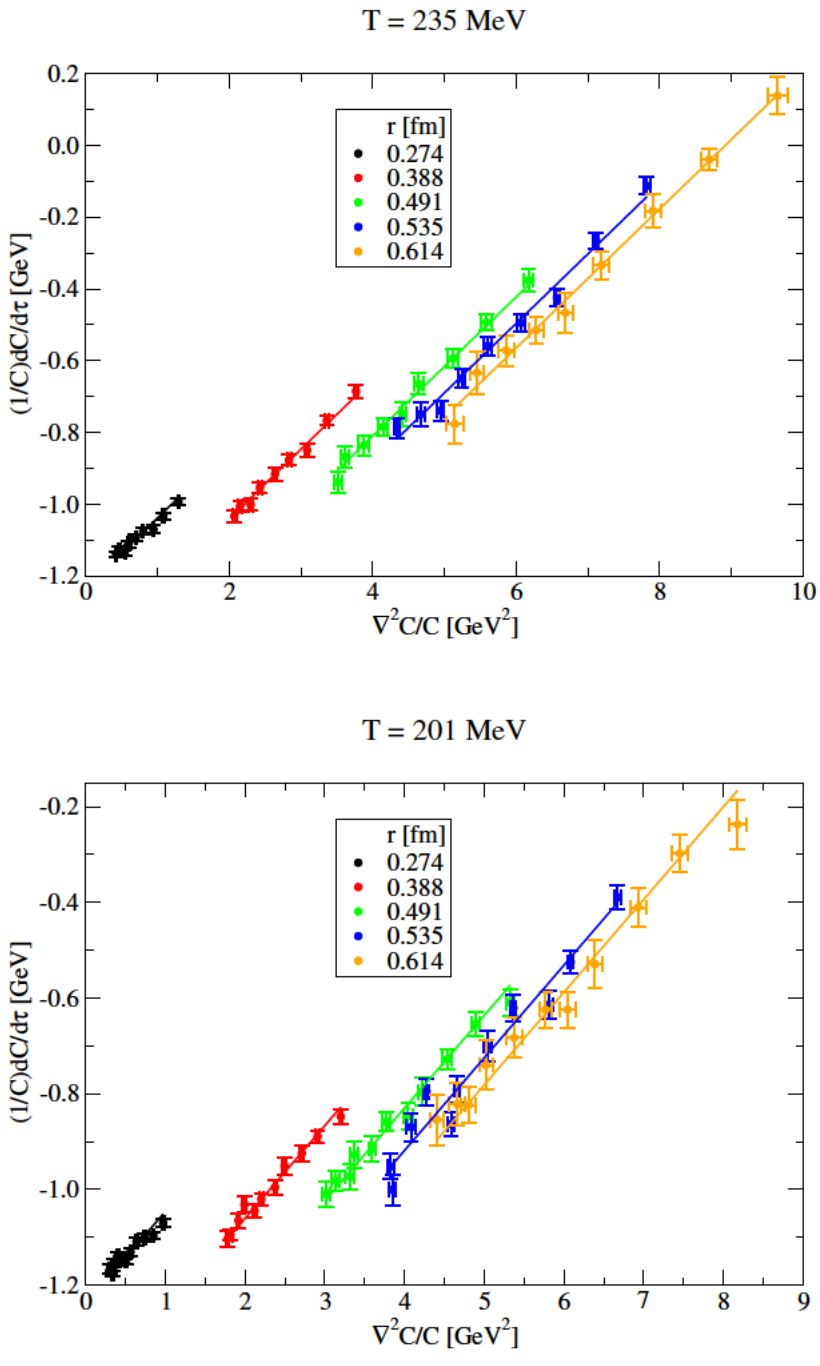

Figure B.2: As in Figure B.1 but for T=235 MeV (top) and T=201MeV (bottom).

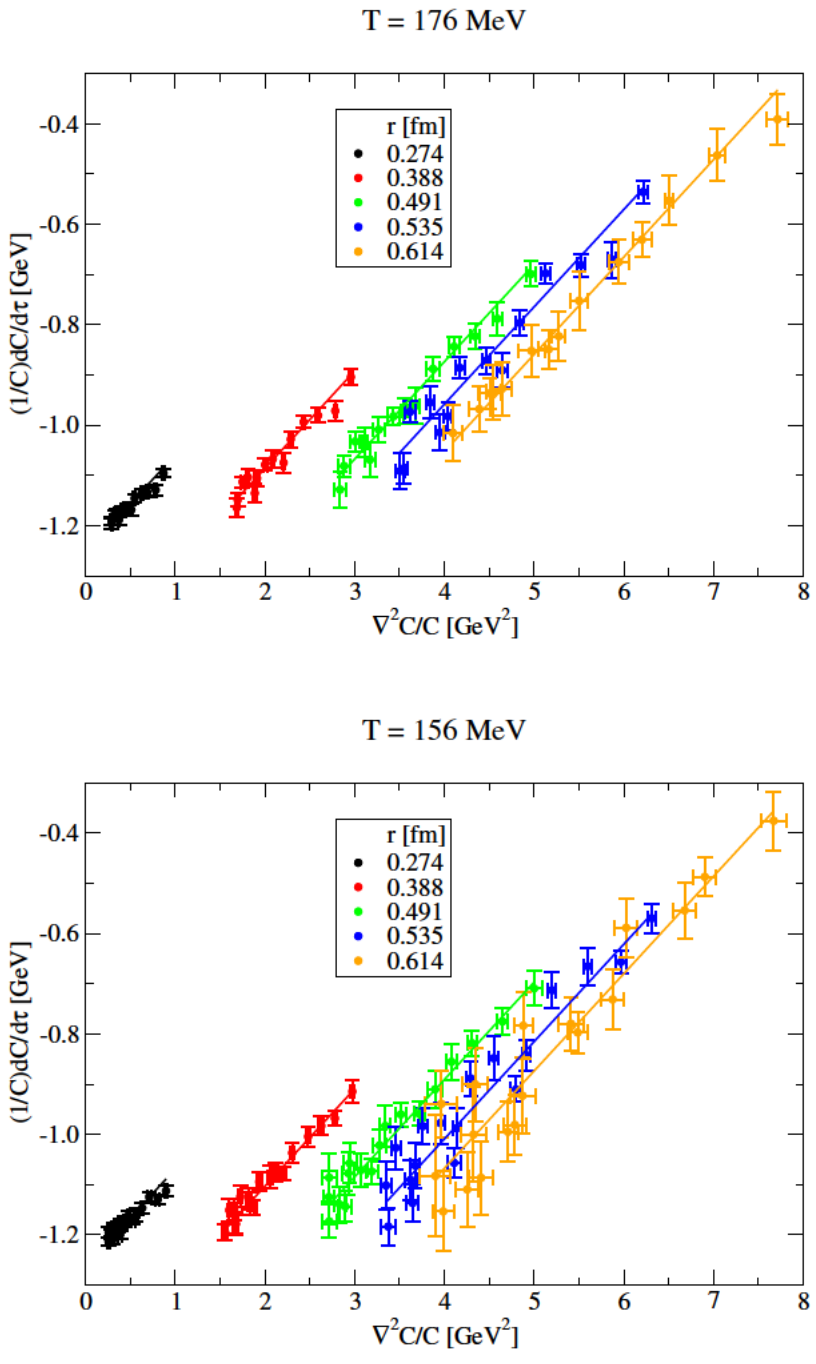

Figure B.3: As in Figure B.1 but for T=176 MeV (top) and T=156MeV (bottom).

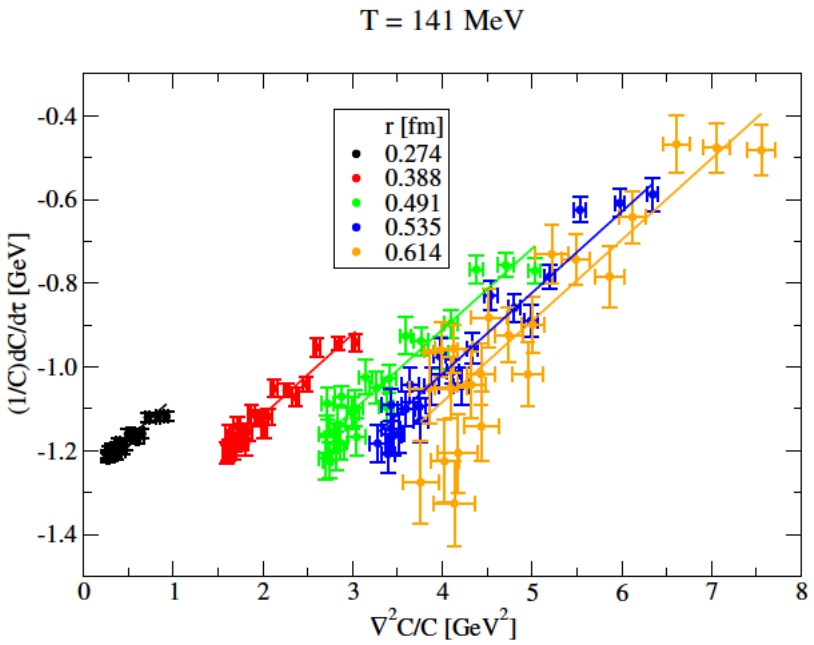

Figure B.4: As in Figure B.1 but for T=141 MeV.

Bibliography

[1] T. Spriggs et al., *Bottomonium spectral widths at nonzero temperature using maximum likelihood*, *PoS* **LATTICE2021** (2022) 077 [2112.01599].

[2] T. Spriggs et al., *A comparison of spectral reconstruction methods applied to non-zero temperature NRQCD meson correlation functions*, *EPJ Web Conf.* **258** (2022) 05011 [2112.04201].

[3] T. Spriggs, C. Allton, T. Burns and S. Kim, *Thermal interquark potentials for bottomonium using NRQCD from the HAL QCD method*, *PoS* **LATTICE2021** (2022) 569 [2112.09092].

[4] T. Spriggs, C. Allton, T. Burns and S. Kim, *New results for thermal interquark bottomonium potentials using NRQCD from the HAL QCD method*, *PoS* **LATTICE2022** (2023) 192 [2301.03320].

[5] C.-N. Yang and R. L. Mills, *Conservation of Isotopic Spin and Isotopic Gauge Invariance*, *Phys. Rev.* **96** (1954) 191.

[6] M. Gell-Mann, *The eightfold way: A theory of strong interaction symmetry*, .

[7] Y. Ne'eman, *Derivation of strong interactions from a gauge invariance*, *Nucl. Phys.* **26** (1961) 222.

[8] M. Y. Han and Y. Nambu, *Three Triplet Model with Double SU(3) Symmetry*, *Phys. Rev.* **139** (1965) B1006.

[9] S. D. Drell, D. J. Levy and T.-M. Yan, *A Theory of Deep Inelastic Lepton-Nucleon Scattering and Lepton Pair Annihilation Processes. 1.*, *Phys. Rev.* **187** (1969) 2159.

[10] D. J. Gross and F. Wilczek, *Ultraviolet Behavior of Nonabelian Gauge Theories*, *Phys. Rev. Lett.* **30** (1973) 1343.

[11] H. D. Politzer, *Reliable Perturbative Results for Strong Interactions?*, *Phys. Rev. Lett.* **30** (1973) 1346.

[12] G. 't Hooft, *When was asymptotic freedom discovered? or the rehabilitation of quantum field theory*, *Nucl. Phys. B Proc. Suppl.* **74** (1999) 413 [hep-th/9808154].

[13] D. J. Gross, *The discovery of asymptotic freedom and the emergence of qcd*, *Proc. Nat. Acad. Sci.* **102** (2005) 9099.

[14] R. K. Ellis and W. J. Stirling, *Qcd and collider physics*, in *1989 CERN-JINR School of Physics*, 8, 1990.

[15] M. E. Peskin and D. V. Schroeder, *An Introduction to quantum field theory*. Addison-Wesley, Reading, USA, 1995.

[16] C. Gattringer and C. B. Lang, *Quantum chromodynamics on the lattice*, vol. 788. Springer, Berlin, 2010, 10.1007/978-3-642-01850-3.

[17] W. Florkowski, *The realistic qcd equation of state in relativistic heavy-ion collisions and the early universe*, *Nucl. Phys. A* **853** (2011) 173 [1008.5225].

[18] T. Boeckel and J. Schaffner-Bielich, *A little inflation in the early universe at the qcd phase transition*, *Phys. Rev. Lett.* **105** (2010) 041301 [0906.4520], [Erratum: Phys.Rev.Lett. 106, 069901 (2011)].

[19] C. Schmid, D. J. Schwarz and P. Widerin, *Amplification of cosmological inhomogeneities from the qcd transition*, *Phys. Rev. D* **59** (1999) 043517 [astro-ph/9807257].

[20] D. J. Schwarz, *The first second of the universe*, *Annalen Phys.* **12** (2003) 220 [astro-ph/0303574].

[21] M. Arslandok et al., *Hot qcd white paper*, 2303.17254.

[22] P. Achenbach et al., *The present and future of qcd*, 2303.02579.

[23] K. Fukushima and T. Hatsuda, *The phase diagram of dense qcd*, *Rept. Prog. Phys.* **74** (2011) 014001 [1005.4814].

[24] M. Durante et al., *All the fun of the FAIR: fundamental physics at the facility for antiproton and ion research*, *Phys. Scripta* **94** (2019) 033001 [1903.05693].

[25] M. Creutz, *Anomalies and chiral symmetry in qcd*, *Annals Phys.* **324** (2009) 1573 [0901.0150].

[26] H. Sazdjian, *Introduction to chiral symmetry in qcd*, *EPJ Web Conf.* **137** (2017) 02001 [1612.04078].

[27] G. Aarts et al., *Properties of the qcd thermal transition with nf=2+1 flavors of wilson quark*, *Phys. Rev. D* **105** (2022) 034504 [2007.04188].

[28] H. Satz, *Colour deconfinement and quarkonium binding*, *J. Phys. G* **32** (2006) R25 [hep-ph/0512217].

[29] E. Eichten, K. Gottfried, T. Kinoshita, J. B. Kogut, K. D. Lane and T.-M. Yan, *The Spectrum of Charmonium*, *Phys. Rev. Lett.* **34** (1975) 369 [Erratum: Phys.Rev.Lett. 36, 1276 (1976)].

[30] E. Eichten, K. Gottfried, T. Kinoshita, K. D. Lane and T.-M. Yan, *Charmonium: The model*, *Phys. Rev. D* **17** (1978) 3090 [Erratum: Phys.Rev.D 21, 313 (1980)].

[31] E. Eichten, K. Gottfried, T. Kinoshita, K. D. Lane and T.-M. Yan, *Charmonium: Comparison with Experiment*, *Phys. Rev. D* **21** (1980) 203.

[32] T. Matsui and H. Satz, *j/ψ suppression by quark-gluon plasma formation*, *Phys. Lett. B* **178** (1986) 416.

[33] F. Knechtli, M. Günther and M. Peardon, *Lattice quantum chromodynamics: practical essentials*. Springer, 2017.

[34] H. J. Rothe, *Lattice Gauge Theories : An Introduction (Fourth Edition)*, vol. 43. World Scientific Publishing Company, 2012, 10.1142/8229.

[35] M. Creutz, *Quarks, Gluons and Lattices*. Oxford University Press, 1983, 10.1017/9781009290395.

[36] S. Borsanyi, S. Durr, Z. Fodor, C. Hoelbling, S. D. Katz, S. Krieg, D. Nogradi, K. K. Szabo, B. C. Toth and N. Trombitas, *Qcd thermodynamics with continuum extrapolated wilson fermions i*, *JHEP* **08** (2012) 126 [1205.0440].

[37] S. Borsanyi, S. Durr, Z. Fodor, C. Holbling, S. D. Katz, S. Krieg, D. Nogradi, K. K. Szabo, B. C. Toth and N. Trombitas, *Qcd thermodynamics with continuum extrapolated wilson fermions ii*, *Phys. Rev. D* **92** (2015) 014505 [1504.03676].

[38] WHOT-QCD collaboration, T. Umeda, S. Aoki, S. Ejiri, T. Hatsuda, K. Kanaya, Y. Maezawa and H. Ohno, *Equation of state in 2+1 flavor qcd with improved wilson quarks by the fixed scale approach*, *Phys. Rev. D* **85** (2012) 094508 [1202.4719].

[39] WHOT-QCD collaboration, Y. Taniguchi, S. Ejiri, K. Kanaya, M. Kitazawa, H. Suzuki and T. Umeda, *n_f = 2+1 qcd thermodynamics with gradient flow using two-loop matching coefficients*, *Phys. Rev. D* **102** (2020) 014510 [2005.00251], [Erratum: Phys.Rev.D 102, 059903 (2020)].

[40] F. Burger, E.-M. Ilgenfritz, M. P. Lombardo and A. Trunin, *Chiral observables and topology in hot qcd with two families of quarks*, *Phys. Rev. D* **98** (2018) 094501 [1805.06001].

[41] A. Y. Kotov, M. P. Lombardo and A. M. Trunin, *Finite temperature qcd with $n_f = 2 + 1 + 1$ wilson twisted mass fermions at physical pion, strange and charm masses*, *Eur. Phys. J. A* **56** (2020) 203 [2004.07122].

[42] B. A. Thacker and G. P. Lepage, *Heavy quark bound states in lattice qcd*, *Phys. Rev. D* **43** (1991) 196.

[43] L. L. Foldy and S. A. Wouthuysen, *On the dirac theory of spin 1/2 particles and its non-relativistic limit*, *Phys. Rev.* **78** (1950) 29.

[44] G. P. Lepage, L. Magnea, C. Nakhleh, U. Magnea and K. Hornbostel, *Improved nonrelativistic qcd for heavy quark physics*, *Phys. Rev. D* **46** (1992) 4052 [hep-lat/9205007].

[45] G. Aarts, C. Allton, S. Kim, M. P. Lombardo, M. B. Oktay, S. M. Ryan, D. K. Sinclair and J. I. Skullerud, *What happens to the υ and η_b in the quark-gluon plasma? bottomonium spectral functions from lattice qcd*, *JHEP* **11** (2011) 103 [1109.4496].

[46] Particle Data Group collaboration, P. A. Zyla et al., *Review of Particle Physics*, *PTEP* **2020** (2020) 083C01.

[47] Particle Data Group collaboration, R. L. Workman and Others, *Review of Particle Physics*, *PTEP* **2022** (2022) 083C01.

[48] R. G. Edwards, B. Joo and H.-W. Lin, *Tuning for Three-flavors of Anisotropic Clover Fermions with Stout-link Smearing*, *Phys. Rev. D* **78** (2008) 054501 [0803.3960].

[49] Hadron Spectrum collaboration, H.-W. Lin et al., *First results from 2+1 dynamical quark flavors on an anisotropic lattice: Light-hadron spectroscopy and setting the strange-quark mass*, *Phys. Rev. D* **79** (2009) 034502 [0810.3588].

[50] Hadron Spectrum collaboration, G. K. C. Cheung, C. O'Hara, G. Moir, M. Peardon, S. M. Ryan, C. E. Thomas and D. Tims, *Excited and exotic charmonium, D_s and D meson spectra for two light quark masses from lattice QCD*, *JHEP* **12** (2016) 089 [1610.01073].

[51] D. J. Wilson, R. A. Briceno, J. J. Dudek, R. G. Edwards and C. E. Thomas, *The quark-mass dependence of elastic πk scattering from qcd*, *Phys. Rev. Lett.* **123** (2019) 042002 [1904.03188].

[52] G. Aarts, C. Allton, A. Amato, P. Giudice, S. Hands and J.-I. Skullerud, *Electrical conductivity and charge diffusion in thermal qcd from the lattice*, *JHEP* **02** (2015) 186 [1412.6411].

[53] G. Aarts, C. Allton, R. Bignell, T. J. Burns, S. C. García-Mascaraque, S. Hands, B. Jäger, S. Kim, S. M. Ryan and J.-I. Skullerud, *Open charm mesons at nonzero temperature: results in the hadronic phase from lattice qcd*, 2209.14681.

[54] A. Mocsy, *Potential models for quarkonia*, *Eur. Phys. J. C* **61** (2009) 705 [0811.0337].

[55] Y. Burnier, M. Laine and M. Vepsalainen, *Heavy quarkonium in any channel in resummed hot QCD*, *JHEP* **01** (2008) 043 [0711.1743].

[56] G. Arfken and J. Romain, *Mathematical methods for physicists*, *Physics Today* **20** (1967) 79.

[57] J. Hadamard, *Sur les problèmes aux dérivés partielles et leur signification physique*, *Princeton University Bulletin* **13** (1902) 49.

[58] S. Shi, L. Wang and K. Zhou, *Rethinking the ill-posedness of the spectral function reconstruction — why is it fundamentally hard and how artificial neural networks can help*, *Comput. Phys. Commun.* **282** (2023) 108547 [2201.02564].

[59] M. Asakawa and T. Hatsuda, *J / psi and eta(c) in the deconfined plasma from lattice QCD*, *Phys. Rev. Lett.* **92** (2004) 012001 [hep-lat/0308034].

[60] S. Datta, F. Karsch, P. Petreczky and I. Wetzorke, *Behavior of charmonium systems after deconfinement*, *Phys. Rev. D* **69** (2004) 094507 [hep-lat/0312037].

[61] A. Jakovac, P. Petreczky, K. Petrov and A. Velytsky, *Quarkonium correlators and spectral functions at zero and finite temperature*, *Phys. Rev. D* **75** (2007) 014506 [hep-lat/0611017].

[62] G. Aarts, C. Allton, M. B. Oktay, M. Peardon and J.-I. Skullerud, *Charmonium at high temperature in two-flavor QCD*, *Phys. Rev. D* **76** (2007) 094513 [0705.2198].

[63] S. Borsanyi et al., *Charmonium spectral functions from 2+1 flavour lattice QCD*, *JHEP* **04** (2014) 132 [1401.5940].

[64] H. T. Ding, A. Francis, O. Kaczmarek, F. Karsch, H. Satz and W. Soeldner, *Charmonium properties in hot quenched lattice QCD*, *Phys. Rev. D* **86** (2012) 014509 [1204.4945].

[65] C01-08-19, CP-PACS collaboration, S. Aoki et al., *Maximum entropy analysis of hadron spectral functions and excited states in quenched lattice QCD*, *Nucl. Phys. B Proc. Suppl.* **106** (2002) 233 [hep-lat/0110127].

[66] Y. Nakahara, M. Asakawa and T. Hatsuda, *Hadronic spectral functions in lattice QCD*, *Phys. Rev. D* **60** (1999) 091503 [hep-lat/9905034].

[67] M. Asakawa, T. Hatsuda and Y. Nakahara, *Hadronic spectral functions above the QCD phase transition*, *Nucl. Phys. A* **715** (2003) 863 [hep-lat/0208059].

[68] F. Karsch, S. Datta, E. Laermann, P. Petreczky, S. Stickan and I. Wetzorke, *Hadron correlators, spectral functions and thermal dilepton rates from lattice QCD*, *Nucl. Phys. A* **715** (2003) 701 [hep-ph/0209028].

[69] G. Aarts, S. Kim, M. P. Lombardo, M. B. Oktay, S. M. Ryan, D. K. Sinclair and J. I. Skullerud, *Bottomonium above deconfinement in lattice nonrelativistic QCD*, *Phys. Rev. Lett.* **106** (2011) 061602 [1010.3725].

[70] G. Aarts, C. Allton, A. Kelly, J. I. Skullerud, S. Kim, T. Harris, S. M. Ryan and M. P. Lombardo, *Quark-Gluon Plasma: from lattice simulations to experimental results*, *J. Phys. Conf. Ser.* **527** (2014) 012013 [1403.5183].

[71] G. Aarts, C. Allton, S. Kim, M. P. Lombardo, M. B. Oktay, S. M. Ryan, D. K. Sinclair and J.-I. Skullerud, *S wave bottomonium states moving in a quark-gluon plasma from lattice NRQCD*, *JHEP* **03** (2013) 084 [1210.2903].

[72] G. Aarts, C. Allton, T. Harris, S. Kim, M. P. Lombardo, S. M. Ryan and J.-I. Skullerud, *The bottomonium spectrum at finite temperature from N_f = 2 + 1 lattice QCD*, *JHEP* **07** (2014) 097 [1402.6210].

[73] S. Kim, P. Petreczky and A. Rothkopf, *Lattice NRQCD study on in-medium bottomonium spectra using a novel Bayesian reconstruction approach*, *AIP Conf. Proc.* **1701** (2016) 060017 [1411.3137].

[74] S. Kim, P. Petreczky and A. Rothkopf, *Quarkonium in-medium properties from realistic lattice NRQCD*, *JHEP* **11** (2018) 088 [1808.08781].

[75] M. Hansen, A. Lupo and N. Tantalo, *Extraction of spectral densities from lattice correlators*, *Phys. Rev. D* **99** (2019) 094508 [1903.06476].

[76] N. Y. Astrakhantsev, V. V. Braguta and A. Y. Kotov, *Temperature dependence of the bulk viscosity within lattice simulation of $SU(3)$ gluodynamics*, *Phys. Rev. D* **98** (2018) 054515 [1804.02382].

[77] B. B. Brandt, A. Francis, B. Jäger and H. B. Meyer, *Charge transport and vector meson dissociation across the thermal phase transition in lattice QCD with two light quark flavors*, *Phys. Rev. D* **93** (2016) 054510 [1512.07249].

[78] B. Page, G. Aarts, C. Allton, B. Jäger, S. Kim, M. P. Lombardo, S. Offler, S. M. Ryan, J.-I. Skullerud and T. Spriggs, *Spectral Reconstruction in NRQCD via the Backus-Gilbert Method*, *PoS* **LATTICE2021** (2022) 134 [2112.02075].

[79] T. Lechien and D. Dudal, *Neural network approach to reconstructing spectral functions and complex poles of confined particles*, *SciPost Phys.* **13** (2022) 097 [2203.03293].

[80] H. Yoon, J.-H. Sim and M. J. Han, *Analytic continuation via domain knowledge free machine learning*, *Physical Review B* **98** (2018) 245101.

[81] S. Offler, G. Aarts, C. Allton, B. Jäger, S. Kim, M.-P. Lombardo, B. Page, S. M. Ryan, J.-I. Skullerud and T. Spriggs, *Reconstruction of bottomonium spectral functions in thermal QCD using Kernel Ridge Regression*, *PoS* **LATTICE2021** (2022) 509 [2112.02116].

[82] Y. Burnier, H. T. Ding, O. Kaczmarek, A. L. Kruse, M. Laine, H. Ohno and H. Sandmeyer, *Thermal quarkonium physics in the pseudoscalar channel*, *JHEP* **11** (2017) 206 [1709.07612].

[83] R. Larsen, S. Meinel, S. Mukherjee and P. Petreczky, *Thermal broadening of bottomonia: Lattice nonrelativistic QCD with extended operators*, *Phys. Rev. D* **100** (2019) 074506 [1908.08437].

[84] R. Larsen, S. Meinel, S. Mukherjee and P. Petreczky, *Excited bottomonia in quark-gluon plasma from lattice QCD*, *Phys. Lett. B* **800** (2020) 135119 [1910.07374].

[85] H.-n. Li and H. Umeeda, *QCD sum rules with spectral densities solved in inverse problems*, *Phys. Rev. D* **102** (2020) 114014 [2006.16593].

[86] S. Gusken, *A study of smearing techniques for hadron correlation functions*, *Nucl. Phys. B Proc. Suppl.* **17** (1990) 361.

[87] J. Berkson, *Minimum chi-square, not maximum likelihood!*, *The Annals of Statistics* **8** (1980) 457.

[88] B. Yoon, Y.-C. Jang, C. Jung and W. Lee, *Covariance fitting of highly correlated data in lattice QCD*, *J. Korean Phys. Soc.* **63** (2013) 145 [1101.2248].

[89] W. H. Press, *Numerical recipes 3rd edition: The art of scientific computing*. Cambridge university press, 2007.

[90] J. A. Nelder and R. Mead, *A simplex method for function minimization*, *The computer journal* **7** (1965) 308.

[91] FASTSUM COLLABORATION collaboration, *in preparation*, .

[92] N. Ishii, S. Aoki and T. Hatsuda, *The nuclear force from lattice qcd*, *Phys. Rev. Lett.* **99** (2007) 022001 [nucl-th/0611096].

[93] S. Aoki, T. Hatsuda and N. Ishii, *Theoretical foundation of the nuclear force in qcd and its applications to central and tensor forces in quenched lattice qcd simulations*, *Prog. Theor. Phys.* **123** (2010) 89 [0909.5585].

[94] HAL QCD collaboration, S. Aoki, T. Doi, T. Hatsuda, Y. Ikeda, T. Inoue, N. Ishii, K. Murano, H. Nemura and K. Sasaki, *Lattice qcd approach to nuclear physics*, *PTEP* **2012** (2012) 01A105 [1206.5088].

[95] HAL QCD collaboration, T. Iritani, S. Aoki, T. Doi, S. Gongyo, T. Hatsuda, Y. Ikeda, T. Inoue, N. Ishii, H. Nemura and K. Sasaki, *Systematics of the hal qcd potential at low energies in lattice qcd*, *Phys. Rev. D* **99** (2019) 014514 [1805.02365].

[96] Y. Ikeda and H. Iida, *Quark-anti-quark potentials from nambu-bethe-salpeter amplitudes on lattice*, *Prog. Theor. Phys.* **128** (2012) 941 [1102.2097].

[97] T. Kawanai and S. Sasaki, *Charmonium potential from full lattice QCD*, *Phys. Rev. D* **85** (2012) 091503 [1110.0888].

[98] T. Kawanai and S. Sasaki, *Heavy quarkonium potential from bethe-salpeter wave function on the lattice*, *Phys. Rev. D* **89** (2014) 054507 [1311.1253].

[99] T. Kawanai and S. Sasaki, *Potential description of charmonium and charmed-strange mesons from lattice QCD*, *Phys. Rev. D* **92** (2015) 094503 [1508.02178].

[100] K. Nochi, T. Kawanai and S. Sasaki, *Bethe-salpeter wave functions of $\eta_c(2s)$ and $\psi(2s)$ states from full lattice qcd*, *Phys. Rev. D* **94** (2016) 114514 [1608.02340].

[101] C. Allton, W. Evans, P. Giudice and J.-I. Skullerud, *The charmonium potential at non-zero temperature*, 1505.06616.

[102] R. Larsen, S. Meinel, S. Mukherjee and P. Petreczky, *Bethe-salpeter amplitudes of upsilons*, *Phys. Rev. D* **102** (2020) 114508 [2008.00100].

[103] A. Rothkopf, T. Hatsuda and S. Sasaki, *Complex heavy-quark potential at finite temperature from lattice qcd*, *Phys. Rev. Lett.* **108** (2012) 162001 [1108.1579].

[104] Y. Burnier, O. Kaczmarek and A. Rothkopf, *Static quark-antiquark potential in the quark-gluon plasma from lattice qcd*, *Phys. Rev. Lett.* **114** (2015) 082001 [1410.2546].

[105] Y. Burnier and A. Rothkopf, *Complex heavy-quark potential and debye mass in a gluonic medium from lattice qcd*, *Phys. Rev. D* **95** (2017) 054511 [1607.04049].

[106] TUMQCD collaboration, P. Petreczky and J. Weber, *Lattice calculations of heavy quark potential at finite temperature*, *Nucl. Phys. A* **967** (2017) 592 [1704.08573].

[107] P. Petreczky, A. Rothkopf and J. Weber, *Realistic in-medium heavy-quark potential from high statistics lattice qcd simulations*, *Nucl. Phys. A* **982** (2019) 735 [1810.02230].

[108] D. Lafferty and A. Rothkopf, *Improved gauss law model and in-medium heavy quarkonium at finite density and velocity*, *Phys. Rev. D* **101** (2020) 056010 [1906.00035].

[109] HotQCD collaboration, D. Bala, O. Kaczmarek, R. Larsen, S. Mukherjee, G. Parkar, P. Petreczky, A. Rothkopf and J. H. Weber, *Static quark-antiquark interactions at nonzero temperature from lattice qcd*, *Phys. Rev. D* **105** (2022) 054513 [2110.11659].

[110] G. Parkar, D. Bala, O. Kaczmarek, R. Larsen, S. Mukherjee, P. Petreczky, A. Rothkopf and J. H. Weber, *Static quark anti-quark interactions at non-zero temperature from lattice QCD*, *EPJ Web Conf.* **274** (2022) 04006 [2211.12937].

[111] S. Godfrey and N. Isgur, *Mesons in a relativized quark model with chromodynamics*, *Phys. Rev. D* **32** (1985) 189.

[112] M. W. Hecht and T. A. DeGrand, *Wave functions of S wave hadrons in the quenched approximation to lattice QCD*, *Phys. Rev. D* **46** (1992) 2155.

[113] C. Drischler, W. Haxton, K. McElvain, E. Mereghetti, A. Nicholson, P. Vranas and A. Walker-Loud, *Towards grounding nuclear physics in QCD*, *Prog. Part. Nucl. Phys.* **121** (2021) 103888 [1910.07961].

[114] G. B. Arfken, H. J. Weber and F. E. Harris, *Mathematical methods for physicists: a comprehensive guide*. Academic press, 2011.

[115] R. Hamming, *Numerical methods for scientists and engineers*. Courier Corporation, 2012.

[116] B. Fornberg, *Generation of finite difference formulas on arbitrarily spaced grids*, *Mathematics of computation* **51** (1988) 699.

[117] C. Michael, *The Running coupling from lattice gauge theory*, *Phys. Lett. B* **283** (1992) 103 [hep-lat/9205010].

[118] A. Bazavov, N. Brambilla, X. G. Tormo, I, P. Petreczky, J. Soto and A. Vairo, *Determination of α_s from the QCD static energy: An update*, *Phys. Rev. D* **90** (2014) 074038 [1407.8437], [Erratum: Phys.Rev.D 101, 119902 (2020)].

[119] F. Karsch, E. Laermann, P. Petreczky and S. Stickan, *Infinite temperature limit of meson spectral functions calculated on the lattice*, *Phys. Rev. D* **68** (2003) 014504 [hep-lat/0303017].

[120] G. Aarts and J. M. Martinez Resco, *Continuum and lattice meson spectral functions at nonzero momentum and high temperature*, *Nucl. Phys. B* **726** (2005) 93 [hep-lat/0507004].

[121] G. S. Bali, K. Schilling and A. Wachter, *Ab initio calculation of relativistic corrections to the static interquark potential. 1: SU(2) gauge theory*, *Phys. Rev. D* **55** (1997) 5309 [hep-lat/9611025].

[122] P. T. Boggs, R. H. Byrd, J. E. Rogers and R. B. Schnabel, *User's reference guide for odrpack version 2.01: Software for weighted orthogonal distance regression*, .